Adventures in Gravitational Wave Detector Control: A Round-Trip Journey

Maggiore, Riccardo

2024

DOI (link to publisher)
10.5463/thesis.566

document version
Publisher's PDF, also known as Version of record

VRIJE UNIVERSITEIT

ADVENTURES IN GRAVITATIONAL WAVE DETECTOR CONTROL: A ROUND-TRIP JOURNEY

ACADEMISCH PROEFSCHRIFT

ter verkrijging van de graad Doctor of Philosophy aan
de Vrije Universiteit Amsterdam,
op gezag van de rector magnificus
prof.dr. J.J.G. Geurts,
in het openbaar te verdedigen
ten overstaan van de promotiecommissie
van de Faculteit der Bètawetenschappen
op donderdag 11 april 2024 om 13.45 uur
in een bijeenkomst van de universiteit,
De Boelelaan 1105

door

Riccardo Maggiore

geboren te Rome, Italië

promotor:	prof.dr. A. Freise
copromotor:	dr. C.M. Mow-Lowry
promotiecommissie:	prof.dr. H.L. Bethlem prof.dr.ir. E.J.G. Peterman dr. S.M. Nissanke prof.dr. A. Vecchio dr. A. Perreca prof.dr. S. Hild

Acknowledgements

When I have to think of a memory that helps me realise how much time has passed since the beginning of my PhD, the choice always falls on the Christmas break of 2019. It was my first Christmas at home after moving to the UK, my first real experience abroad. We were at Giacomo's house playing Christmas games when Nicolò takes from my wallet the University of Birmingham ID card on which the end date of my course is written: September 15, 2023. At that point, the reaction was the only truly possible one for a Roman: "e quando ca**o ci torni a Roma?"[1] – a phrase that undoubtedly accompanied me throughout my entire PhD.

So much time has gone by since that moment, so many moments have passed as well as many people who have accompanied them; it's impossible to thank them all. Here I want to thank those who had a significant role, those who have always been there and whom I hope will continue to be there in the years to come.

Thanks to my brother, Andrea, for being silly exactly the way I am. With you, I share a language of our own.

[1] For all those who are not familiar with Roman dialect, the translation is: "Goodness gracious, any plans for a return to Rome?"

Thanks to my father, Marco, for being the most important person in the hardest moment. In the end, you're the one I always end up talking about.

Thanks to my mother, Cristina, for being the person who understands me better than anyone else. You're the person who always knows exactly what's going on in my mind, sometimes even better then I do.

Thanks to my grandmothers, Anna and Mariuccia. Anna, you are one of the kindest and most empathetic individuals I've ever known. Thank you for spoiling me endlessly, and for your irreverent sense of humor that never fails to bring laughter. As for Mariuccia, I wish you were here with us more than anyone else. I didn't end up continuing to play the guitar as I promised you. I am aware a PhD is definitely not the same thing, but I hope you're still pleased.

Thanks to my uncle, Elvezio, the other person who was there more than anyone else in the hardest moment. You're the coolest of the cool uncles; the reason I started playing basketball as a kid and the reason I started studying law. I don't think I'll ever stop feeling guilty for changing course of study.

Thanks to Lorenzo, my oldest friend and the kindest person I know. You've listened to me in moments when I would have been bored listening to myself.

Thanks to Gianmarco, my partner in adventures and a brother to me. Our travels are the most beautiful memories of the last few years.

Thanks to the other most important friends, Nicolò, Giacomo, Federica, and Guillaume. Although I've never told you, I've learned a lot from you over the years. You've been fundamental to me.

Thanks to Edoardo and Beatrice, who will forever be remembered as the friends from London, although they actually lived in London for only three

months. That time together in the UK is what I remember most fondly in my entire PhD. Special thanks to Edoardo for designing the cover of this thesis.

Thanks to Elenia. I may be a bit late in expressing this, but your notes were the main reason I successfully completed both my Bachelor's and Master's.

Thanks to my supervisor, Andreas, for being first and foremost a friend; for never treating me solely as a PhD student but adjusting the bar based on what I was ready for, and then raising it just a little bit higher to keep pushing me.

Thanks to Paolo, one of the people who taught me the most, and without whom this work would not have been possible.

Thanks to Antonio, who spent hours on the phone with me when it came to choosing my PhD. In a way, all of this started with you.

Thanks to my colleagues at Nikhef in Amsterdam as well as those at the University of Birmingham. Special mention goes to Conor, my second supervisor. I'm sorry for all the times I ditched on you to go climbing. Thanks to the friends in the particle physics group at Nikhef. I have to be honest, I never thought particle physicists could be social animals.

Thanks to all the friends here in the Netherlands, especially Fabrizio, Stefano, Alseesandro and Carlo. A special mention goes to Andrea, who, besides being a great gym-bro, picked up and delivered copies of my thesis to the Beadle's Office.

Thanks to Nikhef and the VU for hosting the last two years of my PhD, and thanks to the University of Birmingham for hosting the first two. Although the time spent in the UK was not very long, I will always remember the university with great affection. Thanks to the European Gravitational Observatory for hosting me for almost a year, undoubtedly an important

period for my PhD.

I conclude by recognising that I would have regretted not including acknowledgments in this thesis. My supervisors from the Master's project still remind me that I didn't include them in that thesis. To make amends, thank you to you as well; better late than never!

Contents

1 Introduction

1.1 Gravitational waves

In 1916, Albert Einstein predicted the existence of gravitational waves, but it took a century for these elusive waves to be observed. The groundbreaking discovery was made by the Laser Interferometer Gravitational Wave Observatory (LIGO) on September 14, 2015 [1, 2]. This observation, known as GW150914, emerged from the collision of two black holes with masses about 36 and 29 times those of the Sun, located approximately 410^{+160}_{-180}Mpc from Earth.

This detection was recognised as an unparalleled achievement worldwide. The waves, emerging from the GW150914 merger, reached Earth as subtle spacetime ripples, altering the length of the 4 km LIGO arms by one thousandth of a proton width. This observation offered a crucial test for General Relativity in the strong gravitational field regime [3], where no deviations were found. It signified the dawn of Gravitational Wave (GW) astronomy, enabling unprecedented observation of astrophysical phenomena and potentially offering direct insight into the universe's earliest epochs.

Before this significant discovery, the exploration of the Universe primarily

relied on electromagnetic (EM) radiation—including visible light, X-rays, and radio waves—with some exploration via neutrinos. These "messengers" provided varied but complementary universal perspectives. Gravitational waves have revolutionised this field, enabling the observation of previously invisible cosmic events, such as black hole collisions. Unlike EM radiation, gravitational waves traverse space virtually unimpeded, delivering clear, direct insights into their origins and opening a new, unobscured window onto the universe, thereby enriching our cosmic understanding.

1.2 A glimpse of the Einstein Telescope

The enhancement in sensitivity following the upgrade of the gravitational wave detectors LIGO [4] and Virgo [5] to the second generation [2, 6] facilitated not only the first direct detection of gravitational waves, but also the subsequent identification of numerous coalescing binaries in the observing runs O1, O2 and O3. This technological advancement enabled the increase in the detection rate and yielded insight into astrophysical processes. Despite this progress, the Signal-to-Noise Ratio (SNR) of the past and the majority of anticipated detections have not fully harnessed the comprehensive potential of GW astronomy. Observation rates and SNR for many crucial sources, such as neutron star mergers or supernovae, remain insufficient within the current detection range. With substantially improved sensitivity, the third-generation detectors will usher in the age of precision GW astronomy. The Einstein Telescope (ET) project [7] in Europe is at the forefront of this scientific revolution. Although the detection of gravitational waves was the objective of "advanced detectors", the emphasis now is on astrophysical observations.

Realising a third-generation GW observatory requires surpassing technological constraints found in current interferometers. The Einstein Telescope plans to employ innovative technologies to attain a sensitivity that is tenfold superior over a broad frequency range compared to the design sensitivities of

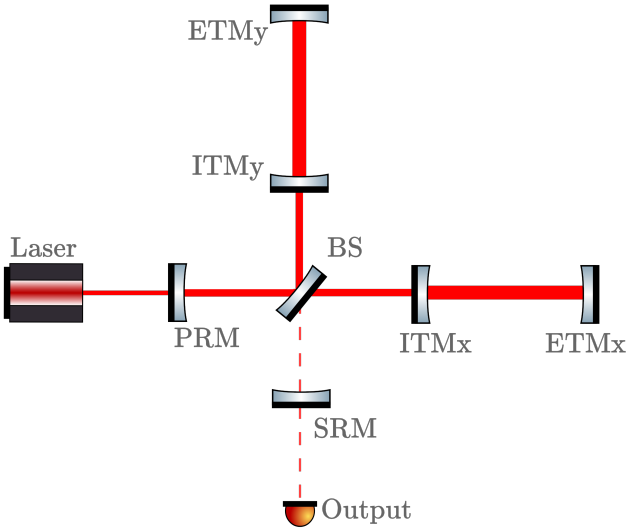

Figure 1.1: Schematic representation of an interferometric gravitational wave detector. The main optics consists of Input Test Masses (ITMx, ITMy), End Test Masses (ETMx, ETMy), the Power Recycling Mirror (PRM), the Beam Splitter (BS), and the Signal Recycling Mirror (SRM). The diagram also indicates the positions of the Output Sensor, where the gravitational wave signal is read.

existing detectors. From a technological point of view, while it is undoubtedly challenging, it is feasible that the technology will be ready by the time the detector is set to become operational (2035+).

1.3 Detection method

Gravitational wave detectors employ laser interferometry for precise measurement of length variations between their two arms. Forthcoming detectors, such as ET, are expected to adopt the same operational principle. The optical configuration of these detectors is based on a dual-recycled Michelson Fabry-Perot arm cavity interferometer, as illustrated in Fig. 1.1. Given the

quadrupolar nature of the radiation, a traversing gravitational wave sequentially expands and contracts one arm of the interferometer while inversely affecting the other [8]. The magnitude of this effect is extremely small, with a relative length change, $\delta L/L$, of less than 10^{-22}. Additional components (such as the PRM and SRM) further enhance the sensitivity and refine the detector response. In particular, the transmission and microscopic positioning of the SRM can be manipulated to restrict the detector bandwidth and amplify its peak sensitivity (Signal Recycling mode) or broaden it, reducing the peak sensitivity (Resonant Sideband Extraction (RSE) mode) [9, 10]. In addition to primary optics, numerous auxiliary optics are employed to condition, align, and match the laser beam into the interferometer and direct the signal field out of the interferometer into the photodetection system.

However, our biggest challenges lie not in individual components, but in the overall behaviour of the instrument, which extends beyond the sum of its parts. This has led to the emergence of a new field that is focused on the science and technology of gravitational wave instruments. It ties to other laser-based metrology, but with unique issues, mainly related to controls.

1.4 Thesis overview

For ET to operate, we must transcend the current state of the art. For controls, the only way to do this involves examining existing systems to identify and understand the limiting constraints. This information will lay the foundation for refined strategies for future detectors.

My work focused on the controls of Virgo with the aim of transferring the acquired knowledge for the ET design. This endeavour not only supports the planning for ET but also supports and enhances Virgo, ultimately leading to a better understanding of the detector.

To surpass the performance of current detectors, we may need to consider

strategies that differ from the current methods in use. From an optical perspective, this indicates the necessity to explore a wider variety of optical configurations beyond the ones presently employed. This is the purpose of Chapter 2. Here, we present a novel technique to control coupled cavities. Although this may seem like a well-explored topic, it is certainly not the case when it comes to strongly coupled cavities. Compared to what we are used to seeing in GW detectors, the optical system behaves in a substantially different manner, requiring the development of specialised techniques, which is the main outcome of the chapter. This marks the first successful design of a sensing scheme for this type of cavity. It is noteworthy for its potential use as a single filter cavity for the low-frequency sensitive component of ET, known as ET-Low Frequency (ET-LF) [11]. This method has been described in a paper [12].

Sensing strategies, such as the one shown in Chapter 2, rely on light modulation-demodulation techniques to generate error signals. These signals are normally used as part of a feedback control system to keep the optical system operational. The control system acts by zeroing the error signals. If the error signals present an offset, the operating point, which is the point where the error signals are zero, no longer coincides with the desired working point. Not being precisely at the working point can lead to unwanted radiation-pressure effects.
In Chapter 3, we explain how optical imperfections can result in the creation of offsets in these types of error signals. Furthermore, we will show how, for marginally stable optical resonators, the creation of an offset is more pronounced.
This work was triggered by commissioning needs and began while I was at the Virgo site from February 2021 to October 2021 and continued even after I left the site. The primary goal was to identify the presence of offsets in the error signals used to control the detector. The outcome of this work has been incorporated in evidence calling for the upgrading of stable recycling cavities for Virgo [13]. This work has moved forward and continued with the help of the master's student, Paul Hapke, who I supervised. Without

him, this work would not have been of the same quality.

ET is expected to outperform current detectors, especially in the low-frequency range, with an anticipated sensitivity improvement of approximately one million times compared to existing detectors in that range. However, a key limitation observed in this frequency region, as seen in LIGO detectors, is the presence of angular control noise. It is reasonable to assume that such constraints could obstruct ET's objectives unless the design intelligently avoids these issues. Thus, evaluating the noise performance of the ET is crucial and, to do this effectively, developing an accurate model is essential. Chapter 4 focuses on a detailed model of Advanced Virgo, which, for the first time, closely matches the measured data. This enables us to make strong predictions about ET's performance. The results of this work have been documented in a paper [14].

Chapter 5, on the other hand, stands as an independent chapter where we present a selection of investigations initiated during my time in Virgo, in addition to those on the offsets in Chapter 3. Specifically, this chapter focusses primarily on a series of simulations for the lock acquisition of the central part of the Virgo interferometer. These simulations are also documented in the more comprehensive publication [15].

Finally, to complete the picture, we list two other publications to which I have contributed but which are not part of the main narrative of my thesis [16, 17].

1.5 A round-trip journey

My work is focused on control techniques for gravitational wave detectors, which involve many different components and various techniques. During my Ph.D., I explored many of these areas. For this reason, we set the narrative as a navigation within a control loop, moving from one component to

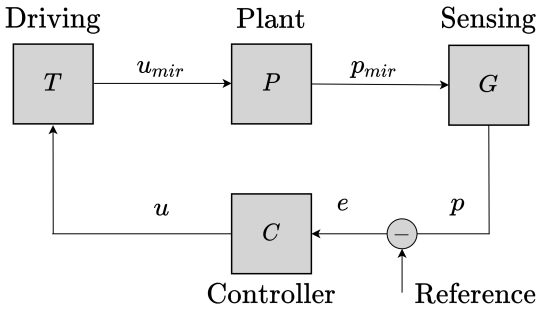

Figure 1.2: Map of our round-trip journey through a control loop.

another. This, in some ways, has been my Ph.D., and I imagine that of many other Ph.D. students: a series of seemingly disconnected blocks that, once the path is closed, have made sense.

Fig. 1.2 shows a block diagram, which is the map that will trace our journey. For those who are eager to embark on this adventure, the meaning of the map and the role of each element will become increasingly clear chapter after chapter. Therefore, these individuals can comfortably skip the rest of the text and head toward Chapter 2, where our journey begins. For the more passionate about cartography, however, a more detailed explanation of the map is given in the upcoming paragraph.

The map of our round-trip journey

In this section, we explain the block diagram in Fig. 1.2. The map is a fairly generic diagram, but it is inspired by the architecture of the two most important control systems of a gravitational wave detector: the one for controlling the relative longitudinal position between the optics and the one for controlling the relative alignment between the optics. For clarity, we will introduce and centre the discussion on the detector's longitudinal Degrees of Freedom (DoFs), even though the reasoning could easily have been referred

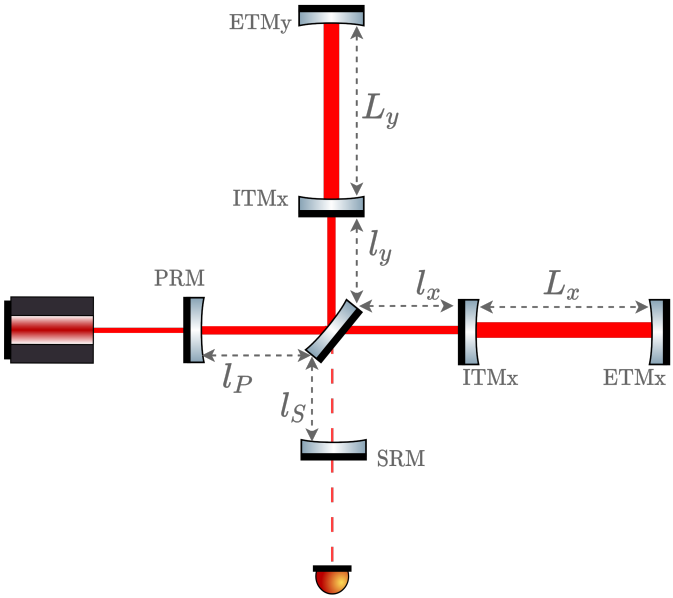

Figure 1.3: Schematic representation of an interferometric gravitational wave detector that highlights its DoFs.

to angular ones. With reference to Fig. 1.3, we define the following DoFs:

$$\begin{aligned}
\text{DARM} &= L_x - L_y \\
\text{CARM} &= \frac{L_x + L_y}{2} \\
\text{MICH} &= l_x - l_y \\
\text{PRCL} &= l_P + \frac{l_x + l_y}{2} \\
\text{SRCL} &= l_S + \frac{l_x + l_y}{2}
\end{aligned} \tag{1.1}$$

DARM stands for Differential ARM length, CARM stands for Common ARM length, MICH stands for MICHelson, PRCL stands for Power Recycling Cavity

Length and SRCL stands for Signal Recycling Cavity Length. Here, we only provide the definition as needed for the purposes of this discussion. More details on the role of each DoF will be provided later in the main text. Now we have everything we need to move through the map.

Sensing: for the five DoFs, the sensing matrix $G \in \mathcal{R}^{5\times5}$ relates the motion of the optics $p_{\text{mir}} \in \mathbb{R}^5$ to the movement of the DoFs, $p \in \mathbb{R}^5$. To provide a practical example, the out-of-phase movement of ETMx and ETMy results in the movement of DARM. In other words, the G matrix is the base-change matrix that goes from the coordinate system of individual optics to that of DoFs. From now on we will assume that by DoFs we mean the DoFs under control. The movement of the DoFs is compared to a reference point to create an error signal, denoted $e \in \mathbb{R}^5$, which is the difference between the position of the DoFs and the reference point. We will call this point the operating point.

Control: the feedback controller $C \in \mathcal{R}^{5\times5}$ uses the error signal to generate a control signal $u \in \mathbb{R}^5$ for each DoF. The driving matrix $T \in \mathbb{R}^{5\times5}$ applies a coordinate transformation to the actuation signal, defining the correction for each of the optics $u_{\text{mir}} \in \mathbb{R}^5$. Providing another practical example, if the out-of-phase movement of ETMx and ETMy leads to a nonzero error signal for DARM, this error signal passes through a controller, producing a correction for DARM. The matrix T defines how much of this correction is applied to ETMx and how much to ETMy. In other words, this matrix again changes the base to switch from the coordinate system of the DoFs back to that of the individual optics.

The plant: Now, let us move on to the heart of the loop, its plant P. Generally, the term "plant" refers to the system or process that is being controlled. It is the physical system on which control actions are performed to manage its behaviour or output. In our specific case, the physical system on which control actions are performed is the mechanics on which the optics are suspended. To mitigate the impact of ground vibrations, optical components

are commonly suspended using seismic isolators. Normally, the actuators used in the control scheme of a gravitational wave detector are attached to the lower stages of the suspension chain. Thus, the mechanical response of the suspension should be considered in the context of the overall loop dynamics.
For a gravitational wave detector, a significant amount of optical power is stored within the cavities. This circumstance makes the effects of radiation pressure non-negligible and impactful on the mechanics. When a mechanical resonator of this type is combined with an optical resonator, it results in a redefinition of the mechanical system. The dynamics of this redefined system cannot be described without considering the influence of optics.

In this line of reasoning, the plant is intended to be in the coordinate system of the individual optics. On the other hand, the plant in terms of the DoFs base is given by:

$$\overline{P} = T \cdot P \cdot G \tag{1.2}$$

For the connection with linear algebra, it is just nice to note that if G is composed of eigenvectors of P and $T = G^{-1}$, the plant in the base of the DoFs is diagonal.

2

Sensing: Tuning of Resonant Doublets in Coupled Optical Cavities

Here begins our round-trip journey, a circular adventure that begins in the thorough territories of Sensing; take a look at the map Fig. 2.1 to check your position. High-precision optical experiments require exact positioning of the optics to guarantee optimal performance. Knowing the position of the optics allows for the implementation of feedback control systems that can correct any deviation from the desired position, ensuring stability of the system over time. Here, the sensing block comes into play, providing precise measurements of optical positions relative to specific working conditions. Although this might seem a straightforward measurement, it is not when extremely high precision is required. In contexts such as laser stabilisation, knowing the precise distance between optics is essential, sometimes to fractions of a light wavelength. This precision is achievable through modulation-demodulation techniques, making them a cornerstone in gravitational wave detectors con-

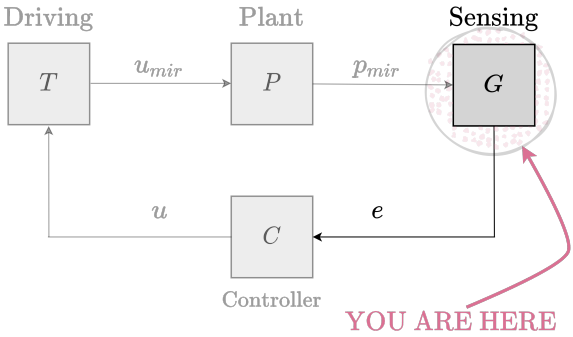

Figure 2.1: Map of our round-trip journey through a control loop.

trol. These techniques yield an indirect position measurement based on the light's propagation path within the optical setup. Because this is influenced by the position of every optical component, it gives rise to the challenge of being able to distinguish the motion of each optical component. This is, in many ways, the greatest challenge for those designing a sensing scheme: laying out the scheme in such a way as to ensure that each target optic's movement (or a combination) is distinguishable. Consequently, while performing an indirect optical measurement allows for greater precision, it might come at the cost of introducing couplings between the various degrees of freedom of the system.

In this section, we introduce a novel sensing technique for controlling coupled cavities that uses light modulation-demodulation methods. While this may seem like a well-explored topic, it is certainly not the case when dealing with strongly coupled cavities. Compared to what we typically observe in gravitational wave detectors, the optical system behaves in a substantially different manner, necessitating the development of specialised techniques. Notably, our proposed method exhibits extremely low coupling levels between the degrees of freedom.

This technique was documented in a paper [12]. In the following sections, we attempt to present the content of the article, trying to alter its format as little as possible. For this reason, at times, we use terms that are paper-orientated, and we refer to the last three sections of this chapter as "Appendices", as they were intended in the original paper.

2.1 Introduction

Large-scale gravitational wave detectors are operational, and the design of third-generation detectors is under way. Current gravitational-wave detectors, such as LIGO [2], Virgo [6] and KAGRA [18] use dual-recycled Michelson interferometers with arm cavities. Next-generation detectors, such as the Einstein Telescope [7] and Cosmic Explorer [19], are expected to inherit the same design concept. Achieving the desired increase in sensitivity for these new detectors will be a challenge and requires the development of new noise-mitigation strategies to overcome the limits of current laser interferometers. Many of these techniques are based on the ability to operate resonant optical systems under strict stability criteria. Theoretical design studies have begun to explore the use of strongly coupled optical cavities as key elements in new precision metrology designs. As an example, coupled cavities can be used in cavity optomechanics to enhance the displacement sensitivity, cooling, and effects that rely on strong quantum back-action [20, 21]. Furthermore, coupled cavities can be used to achieve stable behaviour of phase-correcting quantum phase-insensitive filters [22, 23] and to explore PT-symmetric systems based on balanced gain and loss [24, 25]. More generally, developing the ability to control coupled cavities would allow us to explore a wider array of optical setups, including next-generation gravitational-wave detectors. For example, squeezed light is used in current detectors to increase the sensitivity limited by quantum noise [26]. Future detector designs, which incorporate frequency-dependent squeezing, require the addition of one or more filter cavities [27]. This cascade of filter cavities can potentially be replaced with a coupled cavity, which was found to

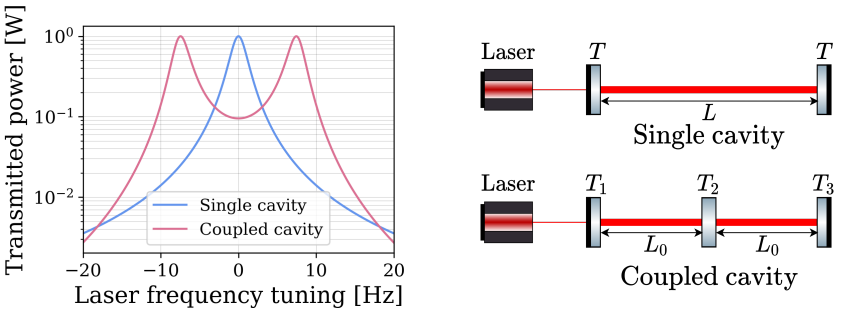

Figure 2.2: Resonances in a single and a coupled cavity. A schematic of a single and coupled cavity setup is on the right-hand side.

perform identically for the ET-LF case [11].

For strongly coupled cavities to be used in precision experiments, such as gravitational-wave detectors, we must develop robust schemes to sense and control parameters of the cavities with a sufficient shot-noise-limited sensitivity. Controlling coupled cavities is not unprecedented, as demonstrated by gravitational-wave detectors. These detectors are typically made up of several coupled optical resonators whose degrees of freedom are measured by well-established methods, as outlined in [28]. These sensing schemes are based on the possibility of setting optical fields of different frequencies to be resonant in different parts of the detector [29]. However, these techniques are not applicable to strongly coupled cavities that exhibit resonance splitting.

The mode profile of a single optical cavity is given by the Airy distribution [30]. In the case of coupled cavities, if the coupling is strong enough, the mode profile turns from a single peak into a resonant doublet, which can be used to enhance multiple modes simultaneously and increase the power driving mitigation systems; Fig. 2.2. In this regime, if a field is resonant in one of the sub-cavities, it is simultaneously resonant in the other one. The system behaves as single resonator, and a field is either resonant in the coupled cavity or it is not. Thus, the resonance condition of a single field is

not sufficient to read out the parameters of the cavity. Therefore, the control of strongly coupled cavities requires the development of specialised sensing techniques.

We present a novel approach to measuring the degrees of freedom of a coupled cavity under the condition of strong coupling between subcavities. This technique enables the tunability of the splitting between the resonant frequencies, which might be crucial for many applications.

The outline of this paper is the following. In Section 2.2, we go through the basics of coupled cavities and show how the distance between the two resonances can be tuned. In Section 2.3, we explain the readout scheme, which consists of phase modulation in combination with a beat frequency demodulation scheme. Section 2.4 is dedicated to the examination of the fundamental noise limits of the readout scheme set by the quantum nature of light. Appendix 2.6 shows how the transmission spectrum of a symmetric coupled-cavity system depends on the system parameters and degrees of freedom. In Appendix 2.7, it is demonstrated that a coupled cavity can be mathematically treated as two independent single cavities in the vicinity of the resonant doublet. This approximation is used in Appendix 2.8 to derive the analytical formulation of the read-out functions. Additionally, in the calculation, it is shown that the error signal designed for laser frequency stabilisation exhibits the same symmetries as the Pound-Drever-Hall (PDH) [31, 32] signal. As a consequence, the error signal is insensitive to several noise sources, at least at a first-order level. Numerical modelling in this paper has been done using the frequency domain modelling software FINESSE [33, 34].

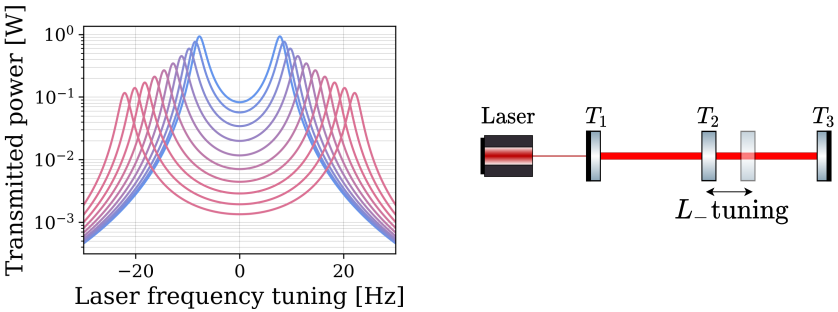

Figure 2.3: Coupled-cavity resonant doublet profile. Blue is for $L_- = 0$, red for increasing tunings of L_-. A schematic of a coupled cavity illustrating the tuning of L_- is on the right hand side.

2.2 System description

A coupled cavity consists of two optically coupled resonators. We consider a three-mirror setup, as illustrated in Fig. 2.2, with the corresponding parameters provided in Tab. 2.1.

The mode profile of a coupled cavity exhibits a resonant doublet. This effect can be resolved if the bandwidth of the subcavities is smaller than the frequency splitting. If this is not the case, this coupling effect is hidden by the large bandwidth of the cavities, and the mode profile of the system would consist of a single peak. The spacing between the resonances is dependent on the optical properties of the coupling mirror, as well as the length of the sub-cavities. We define the length $L_{1,2}$ of each subcavity as the sum of a macroscopic-scale length L_0 (which, for simplicity, we assume to be equal for both subcavities) and a microscopic-scale length variation $\delta L_{1,2}$. In our specific case, the macroscopic length is on the order of 10 km, while the microscopic lengths are in the range of 1 nm. Further details regarding the definition of these lengths can be found in the Appendix 2.6. The frequency splitting between the resonances is influenced by both types of lengths, as

follows:

$$\Delta f = \frac{c}{2\pi L_0} \arccos\left(\sqrt{R_2}\cos\frac{\omega_0 L_-}{c}\right). \tag{2.1}$$

Here, L_- is one of the two degrees of freedom (DoFs) of the coupled cavity, which we define as

$$L_- = \delta L_1 - \delta L_2, \tag{2.2a}$$

$$L_+ = \delta L_1 + \delta L_2. \tag{2.2b}$$

The derivation of Eq. 2.1 can be found in Appendix 2.6. It is worth noting that if $L_- = 0$, the equation simplifies to

$$\Delta f_0 = \frac{c\sqrt{T_2}}{2\pi L_0}. \tag{2.3}$$

Here, Δf_0 is the minimum value of frequency splitting that the coupled cavity can experience. The tuning of the differential cavity length L_- increases the split from Δf_0 allowing the fine tuning to an arbitrary split Δf, as shown in Fig. 2.3 and discussed in detail in Appendix 2.6. This is a useful feature for

Table 2.1: Parameters for the example setup used in this work. The optics is assumed to be lossless. The order of magnitude of the coupled cavity parameters is taken from [11].

Parameter	Value
Laser power P	1 W
Modulation depth β	0.1
Modulation frequency f_m	25 Hz
Input and end mirror transmissivity $T_1 = T_3$	1000 ppm
Mid-mirror transmissivity T_2	10 ppm
Subcavities length L_0	10 km
Minimum frequency splitting Δf_0	15 Hz
Frequency splitting tuned to Δf	50 Hz

any application that might require a precise tuning of the frequency splitting.

Tuning the total system length L_+ is equivalent to shifting the frequency of the input laser beam.

2.3 Readout scheme

To derive a relative measure of the DoFs, we present a sensing scheme (Fig. 2.4) that allows for fine-tuning of the frequency splitting between the resonances. This can be used as part of a feedback system to maintain the tuning of the coupled cavity.

The input optical field is phase modulated at half the desired frequency splitting, $f_m = \Delta f\,/2$. The transmitted signal is mixed with a local oscillator signal of frequency f_m and its second harmonic $2f_m$. Respectively, the error signals produced by demodulating at f_m and $2f_m$ are sensitive to the motions L_+ and L_-, see Fig. 2.5. In the same figure, the compass plots depict how each signal responds to the motion of each degree of freedom, showing that

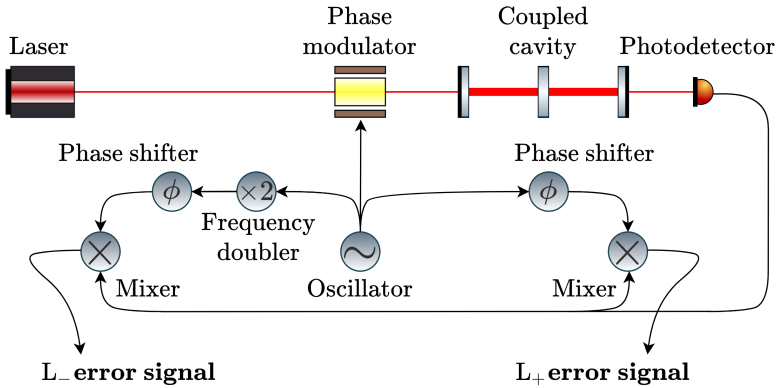

Figure 2.4: Schematic of the proposed readout scheme. A sinusoidal signal from the oscillator is used to drive the phase modulator, which generates sidebands on the laser light. The photodetector signal is then demodulated by mixing it with both the local oscillator signal and its second harmonic.

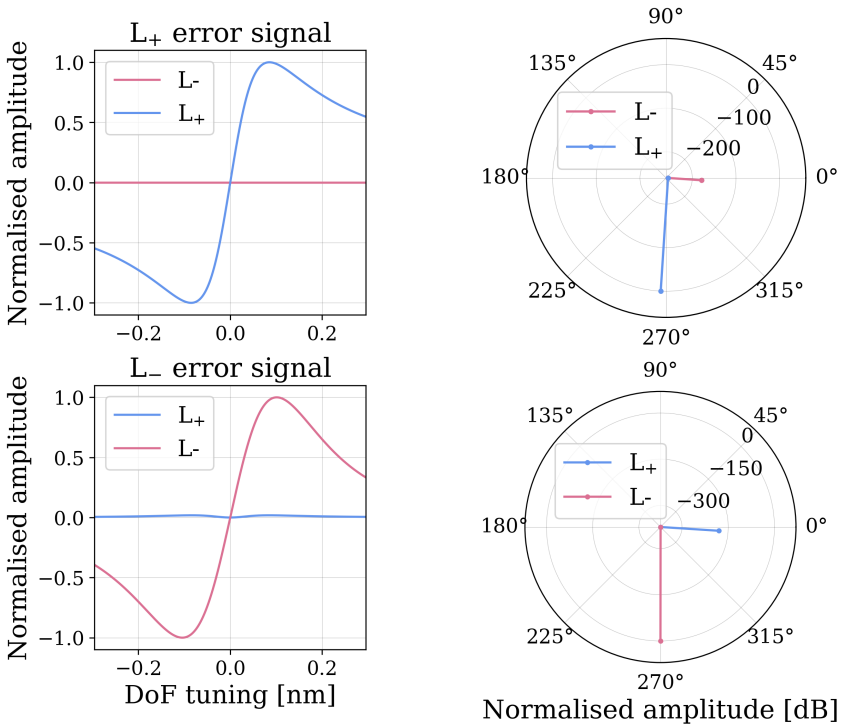

Figure 2.5: The left column shows error signals plotted against the tuning of L_+ in blue and L_- in red, with the tuning being relative to the operating conditions. In the right column, the compass plots show the amplitude and phase of the response of the error signals to the motion of each DoF.

the degrees of freedom are well decoupled in sensing.

At the operating point, L_+ is adjusted to position the laser frequency at the centre of the doublet, while L_- is adjusted to ensure that the frequency splitting corresponds to $2f_m$, resulting in resonance of both sidebands. If any application requires the sidebands not to be resonant, an alternative is to modulate the input laser at slightly different frequencies than $\Delta f/2$ and add an offset to the L_- error signal.

The error signal for L_- is an odd function that indicates not only whether there is a mismatch between the output frequency Δf and the reference frequency $2f_m$, but also whether Δf is greater or less than $2f_m$. This scheme would fail if $\Delta f = \Delta f_0$ as the splitting is at its minimum and it can only become larger. A positive or negative adjustment of L_- would increase the splitting to the same direction and the read-out function for L_- becomes an even function unusable for control purposes.

In conclusion, it is important to note that demodulating a signal at f_m not only isolates the signal at the demodulation frequency, but also generates oscillating terms at its harmonics. These terms must be filtered using a low-pass filter, resulting in a control bandwidth of approximately $\sim 2f_m = \Delta f$.

Taking into account the chosen parameters, the control bandwidth is relatively narrow. However, these were deliberately selected to demonstrate the effectiveness of the sensing technique even in extreme scenarios, such as kilometre-scale cavities for gravitational wave detectors. This effect must be considered in cavity design, but it does not restrict the technique that provides a more comprehensive modulation-demodulation approach for generating error signals in the case of strongly coupled cavities.

2.4 Shot-noise-limited resolution

We examine in this section some fundamental noise limits of the error signals. Noise present in the L_+ error signal is indistinguishable from the laser's frequency noise, and similarly, any noise inherent in the L_- error signal cannot be differentiated from the phase modulator's frequency noise. The quantum nature of light determines the ultimate limit of how low the noise level of an error signal can be.

At the operating conditions, the coupled cavity transmits only a small amount of power in the carrier, while the sidebands are completely transmitted. The average power reaching the photodetector is $\sim 2P_s$, where P_s is the power in each sideband at the output of the modulator. The corresponding

shot noise in the power signal has an amplitude spectral density (ASD) of:

$$A = 2\sqrt{\frac{hc}{\lambda}P_s}. \tag{2.4}$$

To estimate the frequency noise level in either signal, we divide the shot noise spectrum by the optical gain of each signal $D_{\pm}$. The derivation of the optical gains is available in Appendix 2.8. The resulting ASD for the L_+ error signal is

$$A_+ = \frac{A}{D_+} = \frac{\sqrt{T_2}}{16\pi L}\sqrt{\frac{hc^3}{\lambda P}}. \tag{2.5}$$

For the L_- error signal, the ASD is

$$A_- = \frac{A}{D_-} = \frac{T_1}{8\pi L}\frac{1}{\beta}\sqrt{\frac{hc^3}{\lambda P}}, \tag{2.6}$$

where we have assumed the modulation depth β to be small so to approximate the power of the sidebands as in [9]:

$$P_s \simeq \frac{\beta^2}{4}P. \tag{2.7}$$

The error signal for L_- is obtained from the beating of one sideband with the other. Therefore, the optical gain of this signal is proportional to the power of the sidebands, as shown in the Appendix 2.8. The lower the modulation depth, the lower the power of the sidebands, and, as the previous equation indicates, the higher the shot noise.

By using feedback control, it is impossible to stabilise the frequency of both the laser and modulator beyond these limits[1].

[1] As referenced in Appendix 2.6 and, as is evident in Fig. 2.3, adjusting L_- leads to a decrease in the power transmitted by the system, causing an increase in the shot noise of both signals. This effect is not considered in the equations, but it is relatively straightforward to incorporate. For example, if the average power received by the photodetector is reduced by a factor of γ, the optical gain of the error signals decreases by the same factor. As a result, the noise from both error signals increases by a factor of $\sqrt{\gamma}$.

As introduced in Section 2.1 and further elaborated in Appendix 2.8, this scheme utilises symmetries equivalent to the PDH scheme to generate the L_+ error signal. For the sake of comparison, the shot noise in a PDH signal is

$$A_{\mathrm{PDH}} = \frac{T}{16\pi L}\sqrt{\frac{hc^3}{\lambda P}}. \tag{2.8}$$

Consequently, the error signal L_+ would exhibit an equivalent noise floor as the PDH scheme would have for a symmetric cavity, where the transmission through each mirror is $T = \sqrt{T_2}$. The ratio between the ASDs of the two schemes can be expressed as:

$$\frac{A_+}{A_{\mathrm{PDH}}} = \frac{\sqrt{T_2}}{T}. \tag{2.9}$$

2.5 Summary

Controlling coupled cavities can enable exploration of a broader range of optical configurations. We show that a coupled cavity can be treated mathematically as two separate single cavities near the resonant doublet. This approximation is used to derive analytic expressions for the error signals. The analysis also reveals that the error signal created for laser frequency stabilisation demonstrates the same symmetries as the PDH signal, which is convenient in terms of noise couplings.

We have illustrated how to generate a pair of error signals that, when combined with a feedback system, can maintain the tuning of a strongly coupled cavity. This technique uses phase modulation and a beat-frequency demodulation scheme to anchor the mid-frequency of the doublet to the laser frequency and the spacing between the resonances to twice the modulation frequency. This enables tuning of the degree of splitting between the resonances. Moreover, we have found that the degrees of freedom are well decoupled in sensing.

2.6 Appendix A: Frequency splitting

In this section, we show how the frequency splitting between resonant peaks in coupled cavities (Fig. 2.3) depends on cavity parameters. We consider the case of a cavity coupled with three mirrors. In this setup, the external mirrors share identical transmission coefficients, denoted by $T_1 = T_3$, as well as matching reflectivities, given by $R_1 = R_3 = 1 - T_1$. The transmissivity of the middle mirror is given by $R_2 = 1 - T_2$. For simplicity, we also assume that the macroscopic length of both sub-cavities L_0 is the same, so that the sub-cavity lengths are

$$L_1 = L_0 + \delta L_1, \tag{2.10a}$$

$$L_2 = L_0 + \delta L_2. \tag{2.10b}$$

where the length deviations $\delta L_{1,2} \ll L_0$ are typically on the order of or smaller than a single wavelength of the EM field. Finally, we introduce the relative frequency of the electromagnetic field (EM) ω as a frequency offset between the absolute frequency of the EM field $\tilde{\omega} = \omega_0 + \omega$ and one of the resonant frequencies $\omega_0 \gg \omega$ of a single two-mirror cavity of length L_0 (that is, so that $\omega_0 L_0 = \pi N$, where N is an integer).

The transmission coefficient of the coupled cavity system is:

$$\xi(\omega) = \frac{-iT_1\sqrt{T_2}Z_1(\omega)Z_2(\omega)}{1 - \sqrt{R_1R_2}\left[Z_1^2(\omega) + Z_2^2(\omega)\right] + R_1 Z_1^2(\omega)Z_2^2(\omega)}. \tag{2.11}$$

Functions Z_1 and Z_2 represent the extra phase gained by light as it propagates through each of the respective sub-cavities:

$$\begin{aligned} Z_1(\omega) &= \exp(-i\tilde{\omega}L_1/c) \\ &\approx \exp(-i\omega\tau - i\omega_0\delta L_1/c), \end{aligned} \tag{2.12a}$$

$$\begin{aligned} Z_2(\omega) &= \exp(-i\tilde{\omega}L_2/c) \\ &\approx \exp(-i\omega\tau - i\omega_0\delta L_2/c). \end{aligned} \tag{2.12b}$$

where $\tau = L_0/c$ represents the light's travel time across each of the sub-cavities. By switching to the degrees of freedom (DoFs) of interest (2.2),

$$\delta L_1 = (L_+ + L_-)/2, \tag{2.13a}$$

$$\delta L_2 = (L_+ - L_-)/2, \tag{2.13b}$$

we can see that effect caused by any change in the common DoF L_+ is equivalent to a shift of the laser frequency ω by $\omega_0 L_+/(2L_0)$. Therefore, the drift of L_+ would simply change the whole resonance structure in the frequency domain without affecting the splitting between the resonant peaks.

By plugging equations (2.12, 2.13) into (2.11) and assuming $L_+ = 0$, we can write the transmitted power as

$$|\xi(\omega)|^2 = \frac{T_1^2 T_2}{\left(-2\sqrt{R_1 R_2}\cos\varphi_- + (1+R_1)\cos(2\omega\tau)\right)^2 + (1-R_1)^2\sin^2(2\omega\tau)} \tag{2.14}$$

where

$$\varphi_- = \frac{\omega_0 L_-}{c} \tag{2.15}$$

is the additional phase shift caused by the differential DoF L_-. We notice that any non-zero L_- would attenuate the transmitted power. By finding the roots of the derivative of function (2.14) and calculating the difference between the neighbouring ones, we express the frequency splitting of the resonance doublet as

$$\Delta f = \frac{c}{2\pi L_0}\arccos\left(\frac{(1+R_1)}{2R_1}\sqrt{R_2}\cos\frac{\omega_0 L_-}{c}\right), \tag{2.16}$$

or, if the peaks are well-resolved,

$$\Delta f \approx \frac{c}{2\pi L_0}\arccos\left(\sqrt{R_2}\cos\frac{\omega_0 L_-}{c}\right). \tag{2.17}$$

If $L_- = 0$, then the frequency splitting

$$\Delta f = \Delta f_0 = \frac{c}{2\pi L_0} \arccos \sqrt{R_2} \tag{2.18}$$

$$= \frac{c}{2\pi L_0} \arcsin \sqrt{T_2} \approx \frac{c\sqrt{T_2}}{2\pi L_0} \tag{2.19}$$

is reduced to (2.3). An extra factor of 2 that appears in these equations as compared to Equation 1 in [35] is due to the latter describing the frequency position of each of the split resonances with respect to the middle point rather than the full frequency split between them. The dependency of Δf on the differential DoF L_- is described by (2.17).

2.7 Appendix B: Single cavities approximation

In this section, we demonstrate that near the resonances, the transmission coefficient of a coupled cavity can be expressed as a linear combination of the transmission coefficients of two individual cavities. This is a powerful approximation as it allows us to treat coupled cavities as two single independent cavities.

We combine the transmission coefficients of two identical single cavities as follows:

$$\tilde{\xi}(\omega) = \frac{T\, e^{-i(\omega-\Omega)\tau}}{R\, e^{-2i(\omega-\Omega)\tau} - 1} - \frac{T\, e^{-i(\omega+\Omega)\tau}}{R\, e^{-2i(\omega+\Omega)\tau} - 1}. \tag{2.20}$$

where Ω is defined on the frequency splitting of the coupled cavity as $\Omega = 2\pi(\Delta f/2)$.

We assume that the travel time is equivalent to that in Eq. 2.11. As a consequence, the transmission coefficients in (2.20) and (2.11) will have the same free spectral range (FSR): $\Delta\nu_{\mathrm{FSR}} = 1/2\tau$. In the next steps, we will demonstrate that, near the resonances, $\xi(\omega) = \tilde{\xi}(\omega)$ provided that the reflectivity of the individual cavities is $R = \sqrt{R_1}$. After some algebra, the

previous equation can be written as

$$\tilde{\xi}(\omega) = \frac{-2iT\ \sin(\Omega\tau)\, e^{-2i\omega\tau}(e^{i\omega\tau} + R\, e^{-i\omega\tau})}{1 - R\,[2\cos(2\Omega\tau)\, e^{-2i\omega\tau} - R\, e^{-4i\omega\tau}]}. \tag{2.21}$$

For frequencies much much smaller than the FSR of the cavities, the transmission coefficient in the previous equation behaves as follows:

$$\tilde{\xi}(\omega) \simeq \frac{-2iT\ \sin(\Omega\tau)\, e^{-2i\omega\tau}(1 + R)}{1 - R\,[2\cos(2\Omega\tau)\, e^{-2i\omega\tau} - R\, e^{-4i\omega\tau}]}. \tag{2.22}$$

Assuming high finesse for the equivalent single cavities, which implies $(1 + R) \sim 2$, the transmission coefficient $\tilde{\xi}(\omega)$ becomes

$$\tilde{\xi}(\omega) \simeq \frac{-4iT\ \sin(\Omega\tau)\, e^{-2i\omega\tau}}{1 - R\,[2\cos(2\Omega\tau)\, e^{-2i\omega\tau} - R\, e^{-4i\omega\tau}]}. \tag{2.23}$$

If the subcavities of a coupled cavity have the same length $L = L_1 = L_2$, the frequency split is as follows:

$$\Delta f = \frac{c\sqrt{T_2}}{2\pi L} = \frac{\sqrt{T_2}}{2\pi\tau}. \tag{2.24}$$

The expression above can be used to rewrite the cosine and sine terms in (2.23) as:

$$\sin(\Omega\tau) = \sin\left(\sqrt{T_2}/2\right) \simeq \sqrt{T_2}/2, \tag{2.25a}$$

$$\cos(2\Omega\tau) \simeq \sqrt{1 - (2\Omega\tau)^2} = \sqrt{R_2}. \tag{2.25b}$$

Substituting (2.25) back into (2.23), we obtain

$$\tilde{\xi}(\omega) \simeq \frac{-2iT\sqrt{T_2}\, e^{-2i\omega\tau}}{1 - R\,[\sqrt{R_2}\, e^{-2i\omega\tau} - R\, e^{-4i\omega\tau}]}. \tag{2.26}$$

As mentioned above, we assume

$$R = \sqrt{R_1}. \tag{2.27}$$

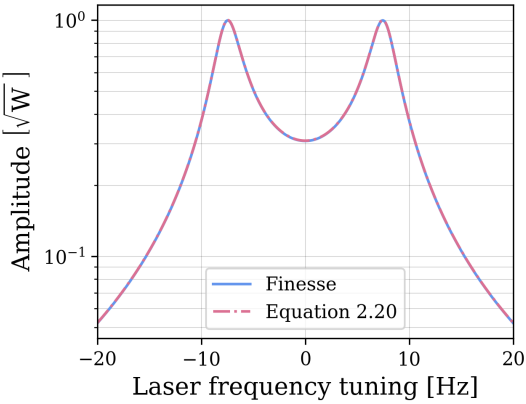

Figure 2.6: Comparison between the transmission coefficient of the coupled cavity computed using FINESSE against the approximation in Eq. 2.20, where we set $R = \sqrt{R_1}$.

Under this assumption,

$$T = 1 - \sqrt{R_1} \simeq (1 - R_1)/2 = T_1/2, \tag{2.28}$$

which makes (2.11) and (2.26) identical.

A comparison between FINESSE output and the approximation (2.20) can be found in Fig. 2.6. This approximation reveals that a coupled cavity can be represented as an equivalent combination of individual symmetric cavities, with each mirror exhibiting a transmission of $T = T_1/2$. With this information, we can proceed to define several quantities that will prove valuable in the following analysis. To begin, we define the finesse of the coupled cavity as follows.

$$\mathcal{F} = \frac{\pi}{T} = \frac{2\pi}{T_1} \tag{2.29}$$

where we have implicitly assumed a high finesse. The linewidth of one of

the resonant peaks is, therefore, given by:

$$\Delta\nu_{\mathrm{LW}} = \frac{\Delta\nu_{\mathrm{FSR}}}{\mathcal{F}} \tag{2.30}$$

where $\Delta\nu_{\mathrm{FSR}}$ has been defined above, but we repeat the definition for clarity:

$$\Delta\nu_{\mathrm{FSR}} = \frac{c}{2L} \tag{2.31}$$

Here, L represents the length of one of the sub-cavities.

2.8 Appendix C: The error signals

This section provides a mathematical interpretation of Section 2.3 by assuming the same setup and deriving the analytical equations for the L_+ and L_- error signals near the resonant doublet. We show that the L_+ error signal shares the same symmetries as the PDH error signal.

Following Appendix 2.7, we approximate the transmission coefficient of a coupled cavity to:

$$\xi(\omega) = \frac{T\, e^{-i(\omega-\Omega)\tau}}{R\, e^{-2i(\omega-\Omega)\tau} - 1} - \frac{T\, e^{-i(\omega+\Omega)\tau}}{R\, e^{-2i(\omega+\Omega)\tau} - 1}, \tag{2.32}$$

with

$$R = \sqrt{R_1},$$
$$T = 1 - R.$$

Input beam modulation.

The input carrier field is phase modulated at Ω so three different beams are incident on the coupled cavity: a carrier of angular frequency ω_c, and two sidebands, with angular frequencies $\omega_\pm = \omega_c \pm \Omega$. For small modulation

depths β, the incident field can be expanded using Bessel functions as:

$$E_i \simeq E_0 \{J_0(\beta)e^{i\omega_c t} + J_1(\beta)[e^{i\omega_+ t} - e^{i\omega_- t}]\}, \tag{2.33}$$

where E_0 is the amplitude the incident beam. The power in the carrier after modulation is

$$P_c = J_0^2(\beta)|E_0|^2$$

and the power in each of the first-order sidebands is

$$P_s = J_1^2(\beta)|E_0|^2.$$

The transmitted beam.

To calculate the beam transmitted by the coupled cavity, we treat each frequency independently and multiply each field component by the transmission coefficient at the corresponding frequency:

$$E_t = E_0\,\xi(\omega_c)J_0(\beta)e^{i\omega_c t} \tag{2.34}$$

$$+ E_0\,J_1(\beta)[\xi(\omega_+)e^{i\omega_+ t} - \xi(\omega_-)e^{i\omega_- t}] \tag{2.35}$$

The total power transmitted by the coupled cavity and measured by the photodetector is:

$$P_t = |E_t|^2 \tag{2.36}$$

$$= P_c\,|\xi(\omega_c)|^2 + P_s\,\{|\xi(\omega_+)|^2 + |\xi(\omega_-)|^2\} \tag{2.37}$$

$$+ 2\sqrt{P_c P_s}\,\{\mathrm{Re}[K]\cos(\Omega t) + \mathrm{Im}[K]\sin(\Omega t)\} \tag{2.38}$$

$$- 2P_s\,\{\mathrm{Re}[G]\cos(2\Omega t) + \mathrm{Im}[G]\sin(2\Omega t)\} \tag{2.39}$$

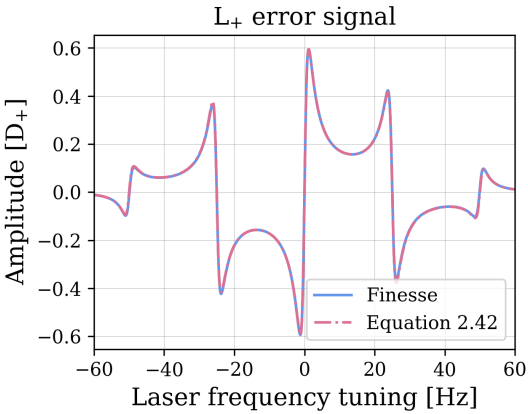

Figure 2.7: The L_+ error signals are plotted against the tuning of the laser frequency, as calculated using FINESSE. The error signal obtained from eq. 2.42 is also displayed in red.

with

$$K = \xi(\omega_c)\xi^*(\omega_+) - \xi^*(\omega_c)\xi(\omega_-),$$
$$G = \xi(\omega_+)\xi^*(\omega_-).$$

Eq. 2.36 contains terms of angular frequency Ω that result from the beat between the carrier and the sidebands. By demodulating P_t at Ω, these terms can be isolated to produce the error signal L_+. On the other hand, the 2Ω terms arise from the beat between the upper and lower side bands, and the demodulation at 2Ω generates the error signal L_-.

The demodulation process involves multiplying the output of the photodetector P_t by a cosine function: $\cos(\tilde{\Omega}t + \theta)$. This cosine function acts as a local oscillator, with $\tilde{\Omega}$ representing the demodulation frequency and θ representing the demodulation phase. The product of this multiplication is then integrated over one period of the cosine function, effectively isolating the $\tilde{\Omega}$ terms of P_t.

In the following paragraphs, P_t is demodulated at Ω and 2Ω to obtain

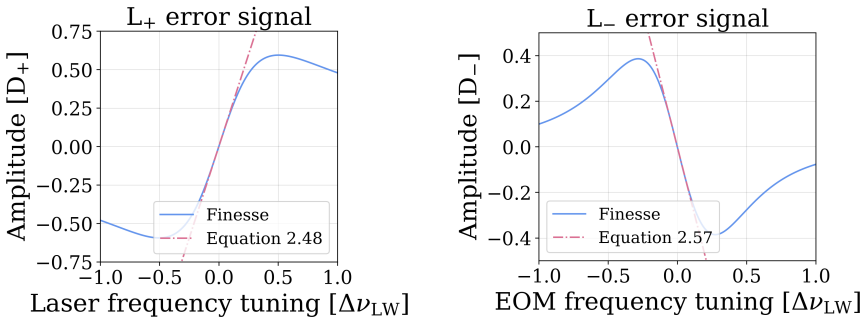

Figure 2.8: Comparison between the behavior of the L_+ and L_- error signals as computed using FINESSE, and the Eqs. 2.48 and 2.57, which describe their behavior within their linear region. For these error signals, the frequency splitting has been tuned to $\Delta f = 30$ Hz. As explained in the main text, this leads to a reduction in transmitted power, resulting in a decrease in optical gain. This effect has been excluded from the equations, while it is considered by default in the FINESSE model. To compare the two results, the FINESSE one has been multiplied by the attenuation of the transmitted power, which is $\gamma = 11$ for the given frequency splitting.

error signals L_+ and L_-. With respect to the DoFs, they were initially defined in the main section in terms of length. However, as shown in Appendix 2.6, they could also be defined in terms of frequencies. In particular, a change in L_+ is equivalent to a variation in the laser frequency, while a change in L_- is equivalent to a variation in the modulation frequency. The following analysis presents the error signal in response to variations in both the laser frequency and modulation frequency.

Demodulating at Ω: L_+ error signal.

Assuming demodulation at Ω, we isolate the Ω terms in Eq. 2.36 to obtain L_+ error signal:

$$\epsilon_+ = 2\sqrt{P_c P_s}\ \{\mathrm{Re}[K]\cos(\theta) + \mathrm{Im}[K]\sin(\theta)\}\,. \tag{2.40}$$

The input beam is modulated at $\Omega = 2\pi(\Delta f/2)$, thus the first-order sidebands are fully transmitted by the coupled cavity, $\xi(\omega_\pm) \sim \mp 1$. We can write K as:

$$K = \xi(\omega_c)\xi^*(\omega_+) - \xi^*(\omega_c)\xi(\omega_-) \sim -2\,\mathrm{Re}\{\xi(\omega_c)\}, \tag{2.41}$$

which is purely real. The sine term in Eq. 2.40 is negligible and we assume $\theta = 0$. L_+ error signal is given as:

$$\epsilon_+ = 2\sqrt{P_c P_s}\,\mathrm{Re}\{K\} \sim -4\sqrt{P_c P_s}\,\mathrm{Re}\{\xi(\omega_c)\}. \tag{2.42}$$

The above equation provides the analytical expression for the error signal we were looking for, and the comparison with the output of FINESSE is shown in Fig. 2.7. In the following lines, we will derive the equation that characterises the linear behaviour of the error signal near the operating point.

The readout scheme sets the frequency of the carrier in the middle of the resonant doublet. In other words, the frequency of the carrier has to be an integer multiple of the free spectral range of the cavity:

$$\omega_c = 2\pi N \cdot \Delta\nu_{\mathrm{FSR}}, \tag{2.43}$$

where N is an integer. As we are interested in the behavior of the error signal around $\omega = \omega_c$, we use the Taylor expansion of $\xi(\omega)$ up to the first order around that point:

$$\xi(\omega_c) \simeq 2i\,\mathrm{Im}\left[\frac{Te^{i\Omega\tau}}{Re^{2i\Omega\tau}-1}\right] \tag{2.44}$$

$$-\mathrm{Im}\left[\frac{T\,e^{i\Omega\tau}\,(1+Re^{2i\Omega\tau})}{(Re^{2i\Omega\tau}-1)^2}\right]\frac{\delta\omega_c}{\Delta\nu_{\mathrm{FSR}}} \tag{2.45}$$

where $\delta\omega_c$ is the deviation of the laser frequency from the center of the doublet. In this scheme, the modulation frequency is much smaller than the cavity FSR, thus $\Omega\tau << 1$. This implies that the first term in parentheses is

almost purely real, and therefore its imaginary part is null and $\xi(\omega_c) \sim 0$. By substituting Eq. 2.44 into Eqs. 2.41 and 2.42, the error signal L_+ is given as:

$$\epsilon_+ = 4\sqrt{P_c P_s}\,\mathrm{Im}\left[\frac{T\,e^{i\Omega\tau}\,(1+Re^{2i\Omega\tau})}{(Re^{2i\Omega\tau}-1)^2}\right]\frac{\delta\omega_c}{\Delta\nu_{\mathrm{FSR}}}. \tag{2.46}$$

Under the assumption of high finesse, as the modulation frequency is much smaller than the FSR, the term below behaves as:

$$\mathrm{Im}\left[\frac{T\,e^{i\Omega\tau}\,(1+Re^{2i\Omega\tau})}{(Re^{2i\Omega\tau}-1)^2}\right] \sim -2\,\mathrm{Im}\left[\frac{1}{e^{2i\Omega\tau}-1}\right] \sim \frac{1}{\Omega\tau}. \tag{2.47}$$

In the above equation, we performed a Laurent expansion around $\Omega\tau = 0$. Substituting this expression into Eq. 2.46, we obtain the error signal within its linear range.

$$\epsilon_+ \simeq 8\sqrt{P_c P_s}\,\frac{\delta\omega_c}{\Omega} = 16\sqrt{P_c P_s}\,\frac{\delta f_c}{\Delta f} = D_+\,\delta f_c, \tag{2.48}$$

where we have written the error signal in terms of the regular frequency $\delta f_c = \delta\omega_c/(2\pi)$ and defined the proportionality constant between ϵ_+ and δf_c as D_+, which is the optical gain of the error signal L_+ relative to a variation of the laser frequency.

In the previous section, we have shown that tuning the frequency splitting leads to a decrease in the power transmitted by the system. To simplify the notation, this effect has been intentionally ignored in Eq. 2.20, where it is assumed that the maximum transmission coefficient remains 1 even for splittings larger than Δf_0. However, the consequence of having a lower transmitted power on the error signals is easy to incorporate. If, for example, the power is reduced by a factor of γ, the optical gain D_+ is reduced by the same amount.

As mentioned previously, this error signal utilises the same symmetries as the PDH scheme. In fact, its mathematical derivation is equivalent to the "Fast modulation near resonance" case described in Black's work [32]. The

key properties of the PDH readout scheme are that the reflected signal is nearly zero at the carrier frequency, and the modulation sidebands are fully reflected by the cavity. This means that the ratio between the input power at the carrier frequency and that measured by the readout photodetector is at its maximum, while the same ratio for the sidebands is almost one.

In the proposed scheme, the photodetector in transmission fulfils the same role as the photodetector in reflection in the PDH scheme. The power to reach the readout photodetector is determined by the transmission coefficient of the coupled cavity $\xi(\omega)$. As mentioned earlier in Eq. 2.44, this coefficient is at a minimum at the carrier frequency, $\xi(\omega_c) \sim 0$, while it is nearly one for the sidebands, $|\xi(\omega_\pm)| \sim 1$. Therefore, the conditions for the L_+ error signal are the same as those for the PDH error signal, making it formally equivalent to the latter. This is convenient as the PDH scheme is a well-performing technique in terms of noise couplings. According to [32], the PDH scheme is insensitive, at least to first order, to several noise sources: variation in the laser power, response of the photodiode used to measure the reflected signal, the modulation depth, the relative phase of the two signals going into the mixer, and the modulation frequency.

For the sake of comparison with the PDH scheme, we rewrite L_+ error signal as

$$\epsilon_+ = 8\sqrt{P_c P_s}\,\frac{T_1}{T_2}\,\frac{\delta f}{\Delta \nu_{\mathrm{LW}}}. \tag{2.49}$$

As described in [32], the PDH error signal for a symmetric cavity with a length of L and a transmission of $T = T_1/2$ through each mirror can be expressed as

$$\epsilon_{\mathrm{PDH}} = 8\sqrt{P_c P_s}\,\frac{\delta f}{\Delta \nu_{\mathrm{LW}}} \tag{2.50}$$

Thus, assuming the same modulation depth, the ratio between the optical

gain of the two error signals is

$$\frac{\epsilon_+}{\epsilon_{\mathrm{PDH}}} = \frac{T_1}{T_2} \tag{2.51}$$

Demodulating at 2Ω: L_- error signal.

Assuming demodulation at 2Ω, we isolate the 2Ω terms in Eq. 2.36 to obtain L_- error signals:

$$\epsilon_- = -2P_s \{\mathrm{Re}[G]\cos(\theta) + \mathrm{Im}[G]\sin(\theta)\}. \tag{2.52}$$

As we are interested in the behavior of the error signal close to the operating point, we expand $\xi(\omega)$ in Taylor series around $\omega = \omega_\pm$, which gives

$$\xi(\omega_\pm) \simeq \mp 1 - i\frac{(1+R)T}{2(1-R)^2}\frac{\delta\omega_m}{\Delta\nu_{\mathrm{FSR}}}, \tag{2.53}$$

where $\delta\omega_m$ is the variation of the modulation frequency relative to Ω.

As in the previous section, the equation above can be simplified by assuming high finesse $\mathcal{F} \simeq \pi/(1-R)$, which also implies $(1+R) \sim 2$. The previous equation becomes the following.

$$\xi(\omega_\pm) \simeq \mp 1 - \frac{i}{\pi}\frac{\delta\omega_m}{\Delta\nu_{\mathrm{LW}}}, \tag{2.54}$$

Thus, G can be expressed as:

$$G = \xi(\omega_+)\xi^*(\omega_-) \simeq -1 - \frac{2i}{\pi}\frac{\delta\omega_m}{\Delta\nu_{\mathrm{LW}}}, \tag{2.55}$$

where we only retained the terms linear in $\delta\omega_m$. By substituting this into Eq. 2.52, we obtain the following for the L_- error signal:

$$\epsilon_- = 2P_s\left\{\cos(\theta) + \frac{2}{\pi}\frac{\delta\omega_m}{\Delta\nu_{\mathrm{LW}}}\sin(\theta)\right\}. \tag{2.56}$$

As the sine term in the previous equation contains all the information about

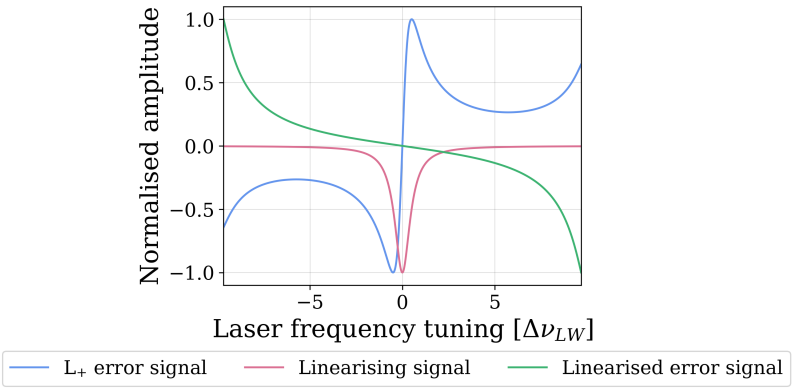

Figure 2.9: The linearization of the L_+ error signal. The standard error signal ϵ_+ is shown in blue, while the linearising signal, which corresponds to the quadrature component of the error signal L_-, is represented in red. The green line represents the linearised error signal.

the frequency change $\delta\omega_m$, we set the demodulation phase to $\theta = \pi/2$ to extract that term[1]. Within its linear region, the error signal is:

$$\epsilon_- = \frac{4P_s}{\pi}\frac{\delta\omega_m}{\Delta\nu_{\mathrm{LW}}} = 8P_s\frac{\delta f_m}{\Delta\nu_{\mathrm{LW}}} = D_-\,\delta f_m. \tag{2.57}$$

As in the previous section, we express the error signal in terms of regular frequency. D_- is the optical gain of the error signal L_- relative to the variation of the modulator's frequency. Fig. 2.8 presents a comparison between the output obtained from FINESSE and the analytical results derived in this section.

Applying the same considerations as for the L_+ error signal, when the frequency splitting is tuned to $\Delta f > \Delta f_0$, the optical gain D_- is diminished by a factor of γ.

[1]With respect to a standard PDH scheme, the 2Ω signal owns this term proportional to δf_m. This is due to the fact that the sidebands are transmitted to the photodetector as $\xi(\omega_\pm) = \mp 1$. In the PDH case, the reflexion coefficient for the detector for the sidebands is -1, which would result in the cancellation of the δf_m term.

It should be noted that the real component of the demodulated signal 2Ω in (2.52) can be used to expand the linear region of the error signal L_+. This is a useful feature that can simplify the process of bringing the system to the operating point.

In the context of the PDH setup, the linear region of the error signal can be expanded by dividing the PDH signal by the power transmitted from the cavity [28]. More generally, any signal with the same profile, namely that of the Airy distribution, is a suitable linearising signal for the error signal. In this section, we have shown that the error signal for L_+ can thus be linearised according to the same principle if divided by another signal whose profile is that of the Airy distribution. In the context of the sensing system that we have presented in this work, such a signal is the in-quadrature component of the L_- error signal. When varying the laser frequency relative to the operating conditions, this is the case

$$-2P_s \,\mathrm{Re}[G] = -2P_s |\xi(\omega_\pm + \delta\omega_c)|^2 \tag{2.58}$$

$$= -2P_s \left| \frac{T\, e^{-i\delta\omega_c \tau}}{R\, e^{-2i\delta\omega_c \tau} - 1} \right|^2 . \tag{2.59}$$

The term $|\xi(\omega_\pm + \delta\omega_c)|^2$ is the Airy distribution, whose characteristic length is by definition the linewidth of the resonant peak. We define the linearized L_+ error signal as

$$\Gamma_+ = \frac{\epsilon_+}{-2P_s \,\mathrm{Re}[G]}. \tag{2.60}$$

The linearisation of the error signal is shown in Fig. 2.9.

3

Sensing: The challenge of the operating point

At this point in our journey, we are still in the territory of sensing, specifically at a rather delicate point where the error signal is generated; check your position in Fig. 3.1. In the previous chapter, we explained how the output of the sensing block is an error signal e. Now, we will be a bit more specific and define the error signal as a measure of the movement of a Degree of Freedom p relative to a reference point, which we will call the operating point. The control loop acts by zeroing the error signal, or in other words, it aims to minimise the difference between the position of the DoF p and the reference value, keeping the system at the operating point. However, there may be cases where the reference used by the error signal is not a good reference for the desired working conditions. When this happens, the error signal presents an offset, and the operating point, which is the point where the error signal is zero, no longer coincides with the desired working point. In this case, the control loop will adjust the DoF to the wrong position.

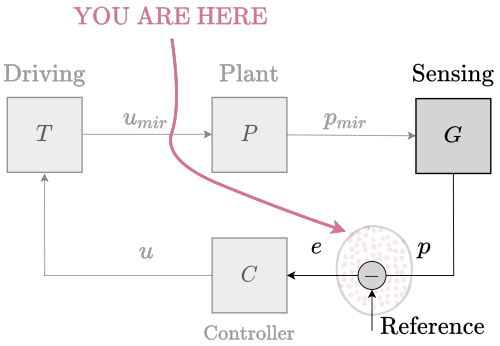

Figure 3.1: Map of our round-trip journey through a control loop.

In the context of interferometric detection, the Pound-Drever-Hall technique is a widely used light modulation-demodulation technique to derive an error signal. In this chapter, we discuss the generation of an offset in the PDH error signal and in the error signals derived from this technique. We will do this by starting with the analysis of the simplest possible case, that of a single cavity, and then we will progress to address the more complex case of the Advanced Virgo Plus (AdV+) detector. Finally, we will discuss the results in Fig. 3.2. This is an example of a transfer function from a complex optomechanical system within AdV+. The curve is shown in blue as a reference. If the error signals used to control the system are affected by offsets, this leads to the system being tuned to the incorrect operating point, typically resulting in a curve similar to the red one. This characteristic makes this transfer function a valuable diagnostic tool for identifying the presence of offsets. We will show that offsets result from optical imperfections that disrupt the phase relationships between beams, and the sensitivity to such effects is particularly pronounced in marginally stable cavities.

We will begin by introducing all concepts and their connections to understand the process that leads to the generation of an offset, starting from

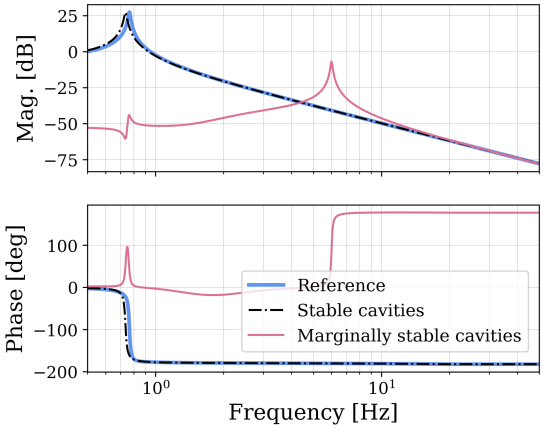

Figure 3.2: All the curves represent the transfer function of a complex optomechanical system within AdV+. The blue reference curve shows how the system should appear. The red and black curves show the transfer function after the introduction of an optical imperfection in the setup. The two curves deviate from the reference due to offsets in the error signals. The deviation is more pronounced in the case of marginally stable (recycling) cavities.

Section 3.1 up to Section 3.3. In Section 3.4, we will analyse the case of a single cavity that uses the PDH scheme to produce an error signal. The analysis was performed for both a stable cavity and a marginally stable cavity, with the effect being more pronounced in the latter. We will show that offsets are caused by the presence of high-order modes of the main laser, as well as by a fundamental limit of the PDH error signal that our analysis highlights, which is perhaps the most intriguing result. Section 3.4.1 represents, in some ways, the culmination of our analysis. Here, we present an analytical interpretation that explains the findings collected in the previous sections and can serve as the basis for future analytical or numerical tools aimed at quantitatively estimating an offset.

From Section 3.5 onwards, the work is focused on the AdV+ detector. This effort originated in the context of commissioning in preparations for the

fourth observational run O4. The goal was to identify the presence of offsets in the error signals used to control the interferometer. Given the specificity of the system and the context in which this work has been developed, we assume that the reader has a basic understanding of the detector's operation. In this case, the higher-order modes of the main laser are suppressed within the PRC. Therefore, the only contribution to the creation of offsets comes from the fundamental limit highlighted in Section 3.4.

3.1 The PDH technique

This technique, aimed at stabilising the frequency of a light field relative to the length of a cavity or vice versa, draws inspiration from well-established techniques used with microwaves and microwave resonators [36]. Drever and Hall have adapted these techniques to function in the optical domain [31]. Currently referred to as the Pound-Drever-Hall technique, this approach is applied in a diverse range of optical setups, including interferometric detection and beyond. An illustrative layout of this method is presented in Fig. 3.3, which illustrates its implementation to generate a length (or frequency) signal within a two-mirror cavity.
The PDH read-out function provides an assessment of the resonance state of a cavity. In terms of lengths, a cavity is resonant with the input laser when its length is half an integer multiple of the laser wavelength – $L_{\text{res}} = (N\lambda)/2$. Mathematically, this approach generates the derivative of the cavity reflection with respect to a variation in its length [32]. The power reflected from the cavity behaves as an even function, peaking when the cavity is on resonance. Consequently, its derivative becomes zero at resonance. Furthermore, the derivative of an even function is an odd function, which takes on positive or negative values depending on whether L is greater or less than L_{res}, making it a suitable error signal. The PDH read-out function is shown in Fig. 3.4. Its complete analytical derivation can be found in [32], which is formally equivalent to that shown in Section 2.8. The crucial information to note is that, in the vicinity of the resonant condition, this function can be expressed

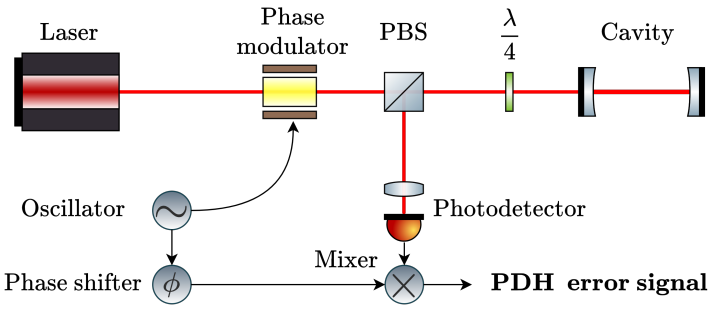

Figure 3.3: Phase-modulation, impresses sidebands onto the laser light. This light is directed onto a two-mirror cavity. A high-speed photodetector is used to collect reflected light, which consists of the two unaltered sidebands along with a phase-shifted carrier component. The Polarising Beam Splitter (PBS) and the plate $\lambda/4$ work together to differentiate between the two directions of light propagation: light that moves from left to right goes straight through the cavity, whereas light travelling from the cavity in the right-to-left direction is redirected towards the photodetector. The photodetector signal is combined with a local oscillator that matches the modulation frequency. Following phase shifting and filtering, the resulting electronic signal provides information about the extent to which the laser carrier frequency deviates from resonance with the cavity. This signal can be used as feedback for active stabilisation purposes.

as follows:

$$\epsilon_{\mathrm{PDH}} = D_{\mathrm{DC}} \cdot \delta z \tag{3.1}$$

where δz is the detuning of the cavity length relative to the resonant case; D_{DC} is the signal gain relative to a change of δz. Specifically, D_{DC} represents the amplification of the length detuning δz. We employ the terms DC and AC to differentiate between the steady-state component (DC) and the frequency-dependent portion of the signal (AC). In fact, the PDH signal responds differently when the length of the cavity varies over time because

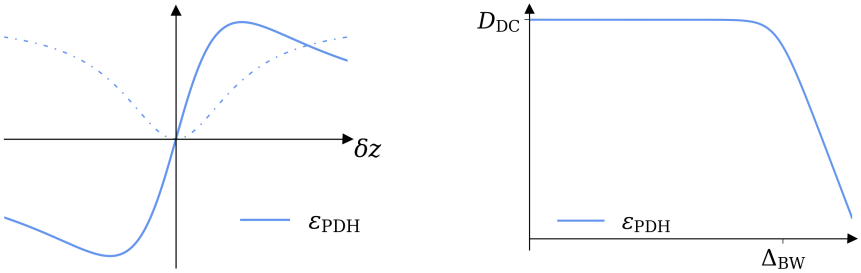

Figure 3.4: The PDH readout error signal as a function of the detuning of the cavity length (on the left), along with its transfer function (on the right). In the plot on the left, the dashed line indicates the power reflected by the cavity.

it is subjected to an external force or input, which causes it to oscillate at a specific frequency f. As this oscillation occurs, it generates sidebands through phase modulation. These sidebands exhibit a frequency difference of $\pm f$ in relation to the carrier light frequency; we will refer to these fields as *signal sidebands*. If this light is detected correctly using a photodiode, it will contain a signal component at frequency f. Subsequently, this specific signal can be extracted from the overall light signal, often achieved through a process such as demodulation [9]. In this case, the PDH gain depends on the oscillation frequency, and its AC gain can be written as:

$$D_{\mathrm{AC}}(f) = D_{\mathrm{DC}} \cdot T_{\mathrm{opt}}(f) \tag{3.2}$$

The DC gain of the signal is weighted by the optical response of the system $T_{\mathrm{opt}}(f)$. This function defines how the amplitude of a signal sideband changes as it passes through an optical system and reaches the readout photodetector. Specifically, it is defined as the ratio of the signal sideband amplitude at the system's output, the photodetector, divided by its amplitude at the input. Because the signal is generated optically, this function is intricately tied to the optical configuration in place. In the case of an optical cavity, this consists of a low-pass response [37], and the AC gain of the PDH signal can

be written as:

$$D_{\mathrm{AC}}(f) = \frac{D_{\mathrm{DC}}}{1 + i(f/\Delta\nu_{\mathrm{BW}})} \tag{3.3}$$

The corner frequency $\Delta\nu_{\mathrm{BW}}$ depends on the optical property of the cavity and is defined as the ratio between the cavity FSR and its finesse:

$$\Delta\nu_{\mathrm{BW}} = \frac{\Delta\nu_{\mathrm{FSR}}}{\mathcal{F}} \tag{3.4}$$

This frequency defines the cavity's bandwidth. The PDH AC gain is shown in Fig. 3.4.

In a broader context, functions such as the one in Eq. 3.3 are known as *transfer functions*. Assuming a Linear Time-Invariant system (LTI), they are defined as the ratio of the output signal to the input signal.

3.2 The longitudinal optical spring and the operating point

To mitigate the impact of ground vibrations, optical components are commonly suspended using seismic isolators. When a mechanical resonator of this type is combined with an optical resonator, the result is a redefinition of the mechanical system whose dynamics cannot be described without considering the influence of the optics. For this reason, these types of system are often described as "opto-mechanical" systems to capture their combined nature.
To explain this concept, let us begin with the fundamentals by introducing the equation that describes the motion of a damped harmonic oscillator:

$$m\ddot{z}(t) + 2m\gamma\dot{z}(t) + Kz(t) = 0 \tag{3.5}$$

In the specific context, we are describing a mass m that can move along a single dimension, which is anchored to a spring of stiffness K. Its displacement from the equilibrium position at time t is indicated as $z(t)$. Alternatively, the

equations of motion are sometimes written as follows:

$$\left[\frac{d^2}{dt^2} + 2\gamma\frac{d}{dt} + \omega_0^2\right] z(t) = 0 \tag{3.6}$$

The expression within the square brackets represents a linear differential operator that operates on $z(t)$. The operator consists of three components, each associated with a fundamental aspect of the damped harmonic oscillator model: a second derivative term originating from Newton's second law, a first derivative term accounting for damping effects, and a constant term representing the oscillatory behaviour caused by the spring force, where we have used $\omega_0^2 = K/m$. This formulation of the equations helps visualise that when the body is displaced from the equilibrium position, it is subject to two forces: a restoring spring force and a damping force. When there is no damping, represented by $\gamma = 0$, the equations of motion are given by:

$$\left[\frac{d^2}{dt^2} + \omega_0^2\right] z(t) = 0 \tag{3.7}$$

In this case, the motion equations reduce to those of a simple harmonic oscillator, where ω_0 represents its natural oscillation frequency.
Finally, since it will be useful for the rest of the following discussion, we transition the previous equation from the time domain to the frequency domain as follows:

$$-m\omega^2 z(\omega) + Kz(\omega) = 0 \tag{3.8}$$

If the system is driven by an external force, the equation of motion becomes:

$$-m\omega^2 z(\omega) + Kz(\omega) = F(\omega) \tag{3.9}$$

The transfer function from an externally induced force to the resulting motion of the body can be formulated as:

$$\frac{z(\omega)}{F(\omega)} = (-\omega^2 + \omega_0^2)^{-1}\, m^{-1} \tag{3.10}$$

Now, we extend this purely mechanical treatment to the optomechanical system in Fig. 3.5. In this context, we are discussing the case of an optical cavity where one of the optics is suspended, while the other is fixed to a rigid support. We assume that the cavity length is such that the circulating beam is in resonance and define δz as small length variations relative to the resonance conditions L_{RES}. Thus, we define the cavity length as $L = L_{\mathrm{RES}} + \delta z$, where δz is much smaller than L_{RES}.
We start by examining the scenario that involves the mirror moving slowly compared to the round-trip time of the cavity, which is $2L/c$. Because under these conditions the cavity response is effectively instantaneous and the system speed can be considered zero, we refer to these conditions as quasi-static [38]. With reference to Eq. 3.5, if the system velocity is zero $\dot{z}(t) = 0$, the damping force is also zero. This allows us to focus our attention solely on the spring force. As shown in [9], the power circulating within the cavity, and consequently the power incident on the suspended mirror, depends on changes in the cavity length as:

$$P_{\mathrm{c}} = \frac{P_0 T_1}{1 + R_1 R_2 - 2\sqrt{R_1 R_2}\cos(2k\,\delta z)} \tag{3.11}$$

Here, R_1 and R_2 respectively denote the reflectivity of the first and second mirror, while T_1 represents the transmissivity of the first mirror. In the presence of a high circulating power across a cavity, the beam exerts a force on the optics through radiation pressure. The amount of force applied depends on the amount of power that circulates within the cavity P_{c}. This dependence is related to the optic positions δz, as shown in the previous

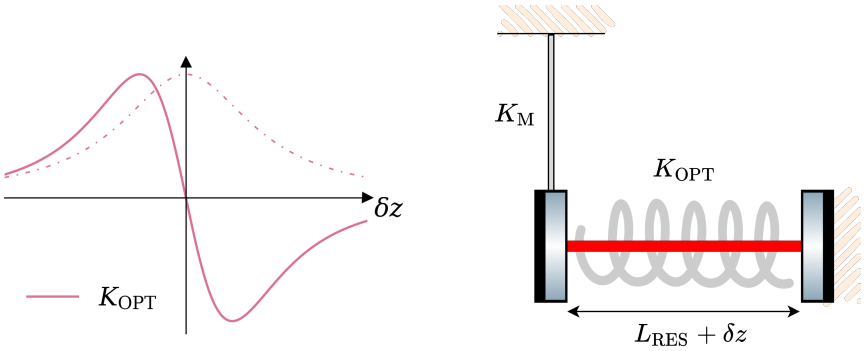

Figure 3.5: On the left, the optical stiffness varying with the tuning of the cavity relative to resonance conditions. The dashed line indicates the circulating power within the cavity. On the right, a schematic of a two-mirror cavity where one of the optics is suspended by a single-stage suspension while the other is fixed to a rigid support. When the length of the cavity deviates from the resonant condition by an amount δz, an optical spring is created, with a stiffness K_{OPT} that adds to the suspension stiffness K_M.

equation. A position-dependent force can be related to the definition of stiffness as follows:

$$K_{OPT} = -\frac{d}{dz}\left[\frac{2P_c(z)}{c}\right] = \frac{-8P_0\sqrt{R_1R_2}T_1\sin(2k\,\delta z)}{c[1+R_1R_2-2\sqrt{R_1R_2}\cos(2k\,\delta z)]^2} \tag{3.12}$$

It is worth noting that when $\delta z = 0$, the optical stiffness K_{OPT} is zero. In particular, if $\delta z > 0$, then $K_{OPT} < 0$, and if $\delta z < 0$, then $K_{OPT} > 0$. The suspended mirror now behaves as if it were attached to a stiff spring K_{OPT}, which we will refer to as the optical spring. The suspended optics is now anchored to a pair of harmonic oscillators connected in parallel, as depicted in Fig. 3.5. The overall stiffness of the system comes from the sum of the mechanical stiffness of the suspension plus that of the *optical spring*.

$$K = K_M + K_{OPT} \tag{3.13}$$

As for this quasi-static case, the way in which the radiation pressure changes the stiffness of the suspension can be understood from a simple mechanical perspective. The introduction of an optical resonator leads to the generation of a position-dependent force that acts on the optics. In the case of $\delta z < 0$, the radiation pressure tends to return the mirror to its equilibrium position. This additional restoring force effectively hardens the suspension, making the overall stiffness greater than the mechanical one. In the case of $\delta z > 0$, a force is created that tends to move the mirror away from the equilibrium position. This anti-restoring force softens the suspension, and therefore the overall stiffness is lower than the purely mechanical one.
Analysing the quasi-static case helps in understanding that the system is essentially composed of two parallel-connected harmonic oscillators. This holds true even when the system velocity is non-zero, with the only distinction from the quasi-static case being that the damping force becomes non-negligible. The equation of motion of the system is typical for a pair of harmonic oscillators connected in parallel, and it is as follows:

$$m\ddot{z}(t) + 2m\left[\gamma_{\mathrm{M}} + \gamma_{\mathrm{OPT}}\right]\dot{z}(t) + \left[K_{\mathrm{M}} + K_{\mathrm{OPT}}\right]z(t) = 0 \tag{3.14}$$

The overall stiffness of the system is given by the sum of the stiffnesses of the two oscillators, just as the overall damping parameter is the sum of their damping parameters. Specifically, the term γ_{M} represents the mechanical damping ratio, while γ_{OPT} is that of the optical spring. As shown in [39, 40], just as the optical stiffness, this factor also depends on the changes in the cavity length relative to the resonance conditions. The expression for it is as follows:

$$\gamma_{\mathrm{OPT}} = -\frac{1}{2\pi\,\Delta\nu_{\mathrm{BW}}}\,\frac{K_{\mathrm{OPT}}}{m(1+\delta^2)} \tag{3.15}$$

with

$$\delta = 2k\mathcal{F}\,\delta z \tag{3.16}$$

We reiterate that $\mathcal{F}$ is the finesse of the cavity. This expression for the damping ratio applies to small differences in the cavity length compared to the resonance conditions. These differences correspond to minor changes in the cavity resonance frequency relative to the laser frequency. By a small variation in the resonance frequency, we mean that it must be much smaller than the cavity bandwidth, $\delta f << \Delta \nu_{\mathrm{BW}}$. In terms of length variation, this condition occurs when $\delta << 1$.
The mechanical stability of the system is determined by its overall stiffness and damping ratio. Stability refers to the system's ability to return to its equilibrium point after being perturbed. If the system is stable, the forces that act on it overall tend to restore it to equilibrium over time. In contrast, the system is unstable when these forces push it away from its equilibrium position. In other words, the stability of the system is determined by the balance of the elastic and damping forces that act on it. A detailed analysis of the balance between these forces in the considered optomechanical system and its consequences in terms of stability can be found in [39]. For our discussion, it is interesting to note that radiation pressure could make the system unstable in two ways: 1) by making the total stiffness of the system negative, or 2) by making the total damping of the system negative. These two possibilities correspond, respectively, to an elastic or damping force that supports motion away from the equilibrium position.

Now, it is worth briefly illustrating a slightly different way of explaining the effect of radiation pressure on the optomechanical system in Fig. 3.5. A less mechanical and more optical approach helps to understand the physical origin of the process. As explained in Section 3.1, a driving force that induces the motion of the suspended mirror at frequency ω results in the generation of signal sidebands at frequencies $\pm\omega$ relative to that of the main laser. As described in [38], the beating of the signal sidebands with the main laser generates a radiation pressure force at the signal frequency ω. This force can be linked to a frequency-dependent stiffness, which is expressed as

$$\tilde{K}_{\mathrm{OPT}}(\omega) = K_{\mathrm{OPT}} + 2im\gamma_{\mathrm{OPT}}\,\omega \tag{3.17}$$

Where K_{OPT} and γ_{OPT} are the optical stiffness and damping defined previously. In this case as well, the overall optomechanical system can be described as a pair of harmonic oscillators connected in parallel. Consequently, the total stiffness of the system is determined by the sum of the mechanical stiffness and the frequency-dependent optical stiffness.

$$\tilde{K}(\omega) = K_{\mathrm{M}} + \tilde{K}_{\mathrm{OPT}}(\omega) = K_{\mathrm{M}} + K_{\mathrm{OPT}} + 2im\gamma_{\mathrm{OPT}}\,\omega \tag{3.18}$$

The overall system can equivalently be described as a simple harmonic oscillator with stiffness $\tilde{K}(\omega)$. In this description of the system, the imaginary component of the stiffness accounts for the damping effect caused by the radiation pressure. The system equation of motion in the frequency domain can be obtained by substituting the expression from Eq. 3.18 into Eq. 3.9, resulting in:

$$\{-m\omega^2 + 2im[\gamma_{\mathrm{M}} + \gamma_{\mathrm{OPT}}]\omega + [K_{\mathrm{M}} + K_{\mathrm{OPT}}]\}z(\omega) = F(\omega) \tag{3.19}$$

The result is precisely equivalent to what would have been obtained by transforming Eq. 3.14 into the frequency domain. As for the force-to-motion transfer function of the system, this can be obtained by substituting Eq. 3.18 into Eq. 3.10.

In this section, we first show that radiation pressure effects are null when the cavity is in resonance. K_{OPT} is proportional to the derivative of the circulating power, and when this power is at its maximum, the derivative is zero. If the optical stiffness is zero, the optical damping ratio is also zero, as shown in Eq. 3.15. The PDH error signal is designed to maintain these resonance conditions by monitoring the beam reflected from the cavity. We discussed that the PDH readout function is the derivative of the reflected signal and, as such, is zero at the minimum of the reflected signal. The reflected signal is at its minimum when the circulating power is at its maximum, and therefore the signal reflected and read by the PDH scheme is a good indicator of the resonance conditions of the circulating beam in the cavity. However, we

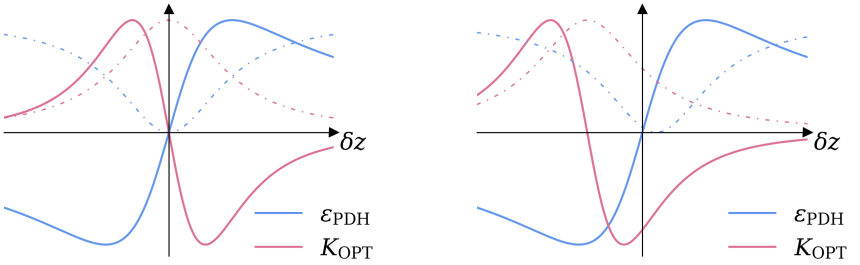

Figure 3.6: The PDH error signal and the optical stiffness varying with the cavity length. When the minimum of the reflected power aligns with the maximum of the circulating power, the two functions can be simultaneously zeroed at the operating point (left). If this does not occur, the two functions cannot be zero at the same point (right).

show in the following sections that the presence of optical imperfections can alter the phase relationship between the circulating beam and the one reflected from the cavity. If this occurs, the minimum of the reflected power does not coincide with the maximum of the circulating power, and hence the reflected beam is no longer a good indicator of the resonance conditions of the circulating field. An illustration of this concept is shown in Fig. 3.6. Based on this reasoning, we define the *operating point* as the point where the error signal is zero, while we refer to the *desired operating point* as the point where the radiation pressure effects are null. The absence of such effects ensures that the cavity is resonant and aligns with the typical operating conditions of most cavity-based setups. Moreover, changes in the suspension response due to a nonzero K_{OPT} can lead to instability in the dedicated control system. Finally, we will denote the distance between the operating point and the desired point as the *offset* of the error signal.

3.3 Transverse electromagnetic modes

In this section, we will continue to illustrate a series of concepts that are helpful in understanding the process that leads to the creation of offsets. To begin with, we delve into the notion of Transverse Electromagnetic Modes (TEM) within a Gaussian beam. Our approach takes inspiration from the more detailed treatment described in [9]. Here, our focus remains on presenting and elaborating on the essential core ideas for the context of this discussion. In an ideal optical resonator, the laser beam would be a smooth Gaussian beam perfectly matching the mirror shapes. However, real-world resonators face practical challenges. Discrepancies between the beam's shape and mirror curvatures, along with deviations from the optical axis due to misalignments and imperfections in mirror surfaces, collectively contribute to distorting the beam away from the theoretical Gaussian ideal. Small distortions of the fundamental beam can be described by the addition of Higher-Order Modes (HOMs). These modes share fundamental characteristics with the primary Gaussian beam. Yet, they exhibit two notable deviations: their intensity patterns differ from the simple focal-point pattern of the fundamental mode, and modes of varying orders accumulate an additional phase as they propagate.

In general, any solution of the paraxial wave equation can be used to describe the transverse characteristics of a scalar electric field, representing an electromagnetic wave with a beamlike quality. A set of functions that satisfies the paraxial wave equation is a suitable basis to describe the lateral shape of a beam. When such a set is complete and countable, it is called a set of transverse electromagnetic modes. The term complete implies that we can represent any solution of the paraxial wave equation, denoted E, by combining TEMs linearly as:

$$E(x,y,z) = \sum_{nm} a_{nm} u_{nm}(x,y,z) \tag{3.20}$$

where the first subscript n corresponds to the mode's order along the x-

axis (horizontal) and the second subscript m to the order along the y-axis (vertical).

3.3.1 Higher-order Hermite–Gauss modes

A Gaussian laser beam, characterised by its Gaussian amplitude profile and a quadratic phase variation, is a fundamental solution to the paraxial wave equation. It represents the lowest-order Hermite–Gauss mode (HG_{00}). Higher-order Hermite-Gauss modes generalise this concept by incorporating higher-order polynomial phase terms. These modes are characterised by their intricate spatial intensity profiles that contain multiple bright spots or intensity maxima within the beam cross section. For this reason, they are suitable for describing more intricate wavefront shapes. Mathematically, the HGMs can be described as follows:

$$u_{nm}(x,y,z) = (2^{n+m-1}n!m!\pi)^{-1/2}\,\frac{1}{w(z)}\,\exp(i(n+m+1)\psi(z))\times \\ H_n\left(\frac{\sqrt{2}x}{w(z)}\right)H_m\left(\frac{\sqrt{2}y}{w(z)}\right)\exp\left(-i\frac{k(x^2+y^2)}{2R_C(z)}-\frac{x^2+y^2}{w^2(z)}\right) \quad (3.21)$$

Here, $w(z)$ represents the beam's dimension along the z-axis and R_C its curvature. These quantities depend on the Gaussian properties of the beam, as explained in more detail in the next section. $H_n(x)$ and $H_m(y)$ are the Hermite polynomials of order m and n along the x and y directions, respectively; k is the beam wave number. Inclusion of higher-order Hermite polynomial terms (m and n greater than 0) in the phase distribution leads to multiple zeros or nodes in the intensity profile of the beam, resulting in the formation of distinct bright spots. These bright spots are spatially separated and contribute to a more complex intensity pattern compared to that of the traditional Gaussian beam.

For the purpose of our discussion, the key parameter to note in the preceding equation is the extra longitudinal phase lag along the z-axis:

$$\varphi_{nm} = (n+m+1)\psi(z) \quad (3.22)$$

The term $\psi(z)$ is known as the Gouy phase [41, 42, 43] and is defined as follows:

$$\psi(z) = \arctan\left(\frac{z - z_0}{z_R}\right) \tag{3.23}$$

The terms z_0 and z_R denote the so-called waist position and Rayleigh range, respectively. These fall within the parameters of the Gaussian beams that will be defined in the next section. As the HGMs set forms an orthogonal basis, each mode can be seen as an individual, independent beam, distinct from the others. Since each mode describes the propagation of the beam in a different region of the transverse plane, each mode experiences a unique optical path. In simpler terms, phase delay φ_{nm} captures these different optical path differences and reflects the different phase velocity for each mode.

3.3.2 Properties of Gaussian beams

The intensity profile across the transverse plane of each mode is influenced by the characteristics of the beam, which we will define for our discussion in the following lines.
The waist of the beam, denoted w_0, is the point at which the Gaussian beam is most tightly focused. At this point, the intensity is at its peak, and the beam has its smallest cross-sectional size. We denote the position of this point along the z axis as z_0. The waist position is a crucial parameter that determines the divergence of the beam and the overall spatial characteristics as it propagates away from this point. The propagation of a Gaussian beam can be divided into two distinct segments along the z-axis: a near-field region near the beam waist and a far-field region far from the waist. The near-field region, which is approximately the length of the Rayleigh range , surrounds the waist. The Rayleigh range, often denoted as z_R, is a characteristic distance associated with the spatial properties of a Gaussian beam. It represents the distance over which the cross-sectional size of the beam increases by a factor of approximately $\sqrt{2}$ from its value at the waist of the beam. In other

words, the Rayleigh range defines the length along the beam propagation axis where the beam's spatial expansion becomes noticeable as it moves away from the waist. The relationship between the Rayleigh range and the size of the beam's spot is connected as follows:

$$z_R = \frac{\pi w_0^2}{\lambda} \tag{3.24}$$

where λ represents the wavelength of the beam. Considering both the position of the beam waist and the Rayleigh range, we can conveniently express the following.

$$w(z) = w_0 \sqrt{1 + \left(\frac{z - z_0}{z_R}\right)^2} \tag{3.25}$$

This equation provides the beam's dimension along the z-axis. In the region where the beam is far from the waist ($z >> z_0, z_R$), an approximation can be employed when:

$$w(z) \approx w_0 \frac{z}{z_R} = \frac{z\lambda}{\pi w_0} \tag{3.26}$$

Another valuable parameter is the radius of curvature of the wavefront at a specific point z. This radius of curvature defines how much the "phase front" of the electromagnetic wave, a surface with a consistent phase that intersects the optical axis at position z, is curved. We calculate the radius of curvature as a function of z to comprehend how the wavefront bends at different locations:

$$R_C = z - z_0 + \frac{z_R^2}{z - z_0} \tag{3.27}$$

Finally, for a more concise description of the properties of a Gaussian beam, we introduce the Gaussian beam parameter q [44]:

$$q = iz_R + z - z_0 \tag{3.28}$$

3.3.3 Cavity eigenmodes and stability

In terms of the Gaussian properties of the beam, identifying the eigenmodes of an optical cavity implies ensuring that the beam parameter q remains the same both before and after completing a complete round-trip through the resonator $q_1 = q_2$. In our analysis, we assume that this condition is consistently met. In essence, the set of HG modes that we use will always consist of eigenvectors of the examined resonator.
As explained in [9], the approach to tackling this particular eigenvalue problem employs techniques rooted in the analysis of the ray transfer matrix. These methods serve to demonstrate the presence of a viable solution if and only if the subsequent condition holds true:

$$0 \leq g \leq 1 \tag{3.29}$$

with

$$g = \left(1 - \frac{L}{R_1}\right)\left(1 - \frac{L}{R_2}\right)$$

Here, the parameter g is called the cavity stability parameter, which depends upon L, the length of the cavity, and R_1 and R_2 are the Radii of Curvature (RoC) of the two mirrors. Values that satisfy the inequality denote stable resonators for which the transverse resonant modes are well defined and supported within the cavity. Values not satisfying the inequality identify unstable resonators for which there is no solution to the eigenmode problem. This implies that the resonator is incapable of supporting well-defined radiation patterns within it, leading to uncontrolled divergence or loss of light beams. The values of g at the edges of inequality (1, 0) indicate marginally stable cavities.

The Gouy phase in the context of an optical cavity

As explained above, the Gouy phase accounts for the additional optical path experienced by a higher-order mode compared to the fundamental

one. In the context of an optical cavity, each time light travels between the two mirrors of the cavity, it accumulates a Gouy phase shift due to the propagation of the beam within the cavity as defined in Eq. 3.23. Therefore, over a round trip through the cavity, the beam traverses the same region twice (once toward the second mirror and once back toward the first). We thus define the round-trip Gouy phase as twice the Gouy phase:

$$\psi_{\mathrm{RT}}(z) = 2\psi(z) \tag{3.30}$$

As shown in [45], the round-trip Gouy phase can be expressed in terms of the stability parameter as:

$$|\psi_{\mathrm{RT}}(g)| = 2\arccos(\sqrt{g}) \tag{3.31}$$

What is noteworthy for our analysis is that, in the case of marginally stable cavities, the round-trip Gouy phase is zero. This implies that there is no phase lag among the various HGMs, and, to some extent, they all undergo the same optical path. Consequently, if the fundamental mode of the beam is resonant within the cavity, so will all subsequent HOMs.

3.3.4 Scattering into higher-order modes

The presence of an imperfection in an optical setup causes the beam to deviate from the ideal Gaussian profile. As a result, the fundamental Gaussian mode is no longer sufficient to describe the wavefront shape, and higher-order modes are required. To be more precise, the presence of the imperfection scatters a portion of the power from the fundamental mode into HOMs.
A detailed elucidation of the scattering process and the relevant coupling coefficients can be found in [9], while the mode orders involved for each type of defect are detailed in [46]. For our discussion, all that is needed to understand is that a portion of the power from the fundamental mode gets converted into a higher-order mode, and this process is not one-way. For a portion of the HG_{00} mode converted to HG_{nm}, a corresponding portion of the HG_{nm} mode is re-focused to the HG_{00} mode. The phase of the beam that

returns in the fundamental mode depends on the entire scattering process. For each mode, the scattering chain unfolds as follows:

$$\mathrm{HG}_{00} \xrightarrow[\text{Scattering}]{\phi_{nm}} \mathrm{HG}_{nm} \xrightarrow[\text{Propagation}]{\varphi_{nm}} \mathrm{HG}_{nm} \xrightarrow[\text{Back-scattering}]{\phi_{nm}} \mathrm{HG}_{00}$$

The beam in the 00 mode scatters in the nm order mode. During this scattering process, light acquires a phase shift, which we refer to as ϕ_{nm}. Subsequently, as light propagates in the nm mode, it accumulates a phase delay φ_{nm} as per Eq. 3.3.1. Finally, when the mode nm is rescattered into the fundamental mode, it gathers another phase factor of ϕ_{nm}. For reasons based on the principle of reversibility of the optical path, the phase accumulated during scattering is the same as that collected during backscattering. All of this chain determines the phase of the beam that returns to the fundamental mode, which may no longer be in phase with the beam that has remained in the 00 mode in the meantime.

3.3.5 The PDH error signal in the presence of HOMs

The final concept needed to understand the process of generating an offset involves understanding the behaviour of the PDH signal in the presence of HOMs. Each of these modes can be envisioned as an individual beam with its distinct error signal, linked to its resonance conditions. The resulting PDH signal is the aggregate of individual contributions to the error signal from each of these modes. In this section, we provide a brief mathematical formalisation of this concept to identify the mode that plays the key role in generating an offset.

In general, for a field with multiple frequency components, the power read by a photodetector can be written as:

$$|E|^2 = E \cdot E^* = \sum_{ij} A_{ij} e^{i(\omega_i - \omega_j)t} \tag{3.32}$$

Here, $A_{ij} = a_i a_j^*$ and a_i represents the amplitude of the component at angular

frequency ω_i. Diagonal terms refer to the average power of a component at frequency ω_i. Off-diagonal terms are generated by the beating of two components at different frequencies, ω_i and ω_j. The frequency of the beat signal is $\Omega_{ij} = |\omega_i - \omega_j|$. As shown in [47], demodulating the signal at Ω_{ij}, in conjunction with low-pass filtering, enables the isolation of all beat signals that occur at that frequency. The resulting demodulated signal is given by:

$$\epsilon = \sum_{ij} \mathrm{Re}[A_{ij}\, e^{-i\phi}] \quad \text{with} \quad \{i, j \,|\, j, i \in \{0, ..., N\} \wedge \omega_i = \omega_j\} \tag{3.33}$$

where ϕ is the demodulation phase, which we will now consider to be zero for the sake of notation simplicity. Within the context of the PDH technique, the composite field detected by the photodetector consists of the primary laser beam operating at frequency ω_0, known as the carrier, along with two additional sidebands at frequencies $\omega_\pm = \omega_0 \pm \Omega$. The beat between the carrier and these sidebands results in the emergence of a signal at the modulation frequency Ω on the readout photodetector. Expanding this discussion to account for the presence of HOMs, it is important to note that, due to the orthogonality of HG modes, interactions will occur only between sidebands and the carrier within modes of the same order nm. In this scenario, the previous equation defines the PDH error signal for every individual mode as:

$$\epsilon_{\mathrm{PDH},\,nm} = 2\mathrm{Re}[A^*_{+,\,nm} + A_{-,\,nm}] \tag{3.34}$$

with

$$A_{\pm,\,nm} = a^*_{0,\,nm}\, a_{\pm,\,nm}$$

Where $a_{0,\,nm}$ and $a_{\pm,\,nm}$ correspond to the complex amplitudes of the carrier and the $\omega_\pm$ sidebands in mode nm, respectively. The resulting PDH error signal is obtained by summing all contributions for each mode:

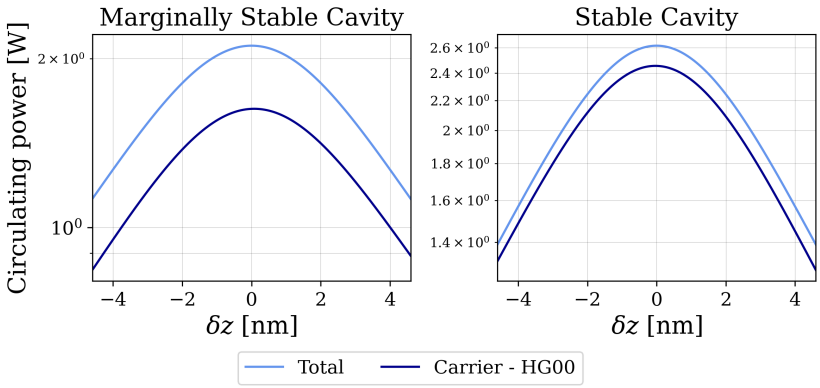

Figure 3.7: In both cases, the marginally stable cavity (left) and the stable cavity (right), the plots show the circulating power within the cavity. These plots emphasise that at zero tuning, the system aligns with the desired operational point, characterised by maximum circulating power. This point coincides with the maximum circulating power in the fundamental mode.

$$\epsilon_{\mathrm{PDH}} = \sum_{nm} \epsilon_{\mathrm{PDH},\,nm} \tag{3.35}$$

3.4 Offset creation in a single cavity

In this section, we analyse the generation of an offset in the presence of optical imperfections in the simplest setup possible, that of a single cavity where the PDH scheme is used to produce an error signal. We will consider two cases, that of a stable cavity and a marginally stable one. We will show that the effect is more pronounced in the case of the marginally stable cavity, despite a smaller optical imperfection being considered. For both cases, this study reveals a fundamental limit of the PDH signal originating in the HG_{00} mode. The origin of this limitation lies in the sequence of scattering and backscattering to and from HOMs. The investigation was carried out through

numerical modelling that has been performed using the frequency domain modelling software FINESSE.

The setup analysed is shown in Fig. 3.3. For the parameters considered, they are reported in Tab. 3.1. We present two case studies, and the entries "stable" and "marginally stable cavity" refer to two different setups we considered. The two setups are identical except for the values of the Radii of Curvature (RoCs) of the optics. Once the cavity length was chosen to make it kilometre-scale, the RoC values were chosen to make the first cavity close to instability and the second one stable. In the study of each set-up, a different base of HGMs was used, but they were chosen according to the same principle. As anticipated in Section 3.3.3, for each resonator considered, the input beam parameters are chosen to match the cavity eigenvalues. In both cavities, we introduce an optical imperfection by enlarging the RoC by 30 m for the nearly unstable cavity and by 300 m for the stable one. Such variations can arise due to thermal effects [48]. When high power circulates

Table 3.1: Parameters of the PDH setups we have considered.

Parameter	Value
Laser power P	1 W
Modulation depth β	0.1
Modulation frequency f_m	15 MHz
Input mirror transmissivity T_1	$1 \cdot 10^4$ ppm
End mirror transmissivity T_2	$1 \cdot 10^5$ ppm
Cavity length L	3 km
Marginally stable cavity	
Input and end mirror RoC $R_1 = R_2$	1502 m
Input mirror RoC change ΔR_1	30 m
PDH DC gain D_{DC}	−0.06 MW/m
Stable cavity	
Input and end mirror RoC $R_1 = R_2$	2500 m
Input mirror RoC change ΔR_1	300 m
PDH DC gain D_{DC}	−0.26 MW/m

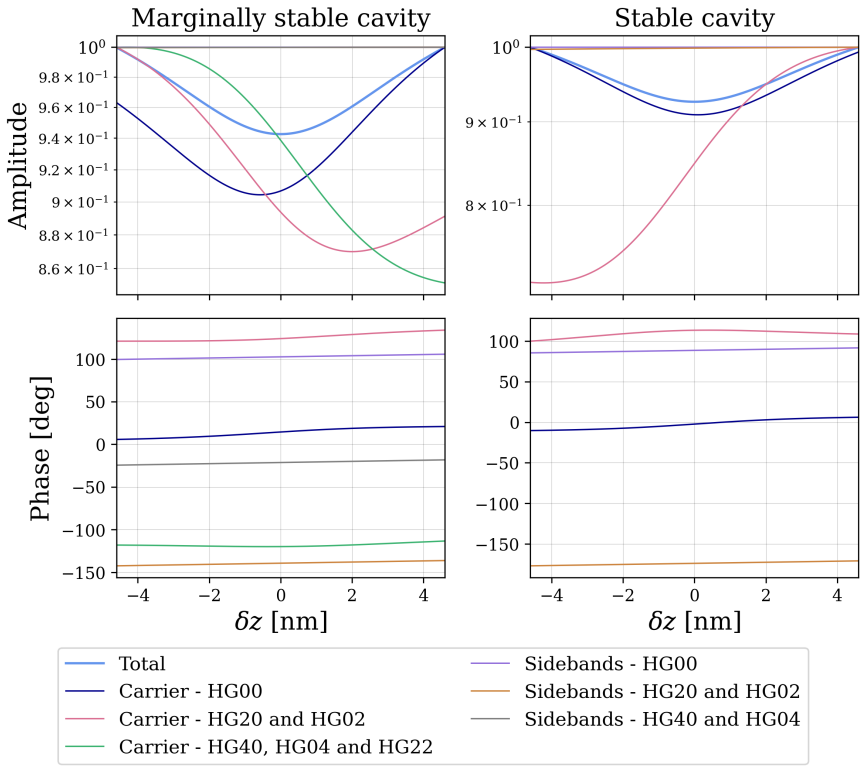

Figure 3.8: Amplitudes and phases of the beam components as at the readout photodector in reflection. The left column corresponds to the marginally stable cavity, while the right column represents the stable cavity. The "zero tuning" point refers to desired operational conditions with maximum circulating power in the cavity. The amplitudes have been normalised. For each setup, only the modes that contribute significantly to the offset are shown.

across a cavity, the energy absorbed by the optics can generate thermoelastic deformations within the optics. The chosen level of deformation is relatively pronounced, and in practical scenarios such significant changes would be implausible. However, these extreme cases prove to be valuable for

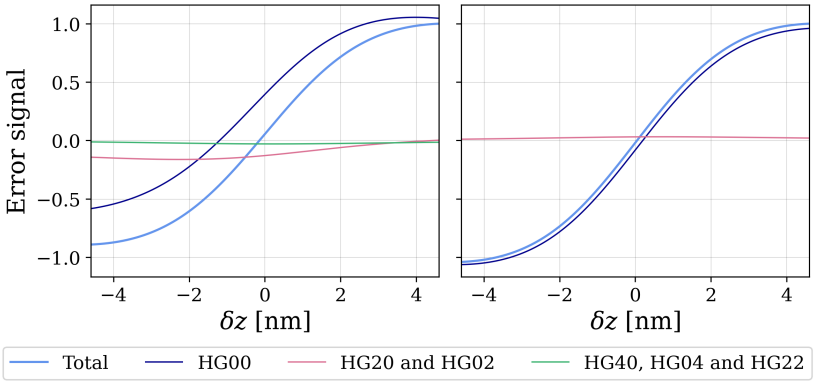

Figure 3.9: PDH error signal separated into contributions per HOM.

Table 3.2: Higher order modes contribution to the PDH error signal at the desired operating point. Only the modes that contribute significantly to the offset are shown.

Marginally stable cavity

Mode	Offset [nm]
HG_{00}	−1.20
HG_{02}	0.44
HG_{20}	0.44
HG_{22}	0.06
HG_{04}	0.06
HG_{40}	0.06

Total offset: −0.15 nm.

Stable cavity

Mode	Offset [nm]
HG_{00}	0.19
HG_{02}	−0.07
HG_{20}	−0.07
HG_{22}	0.00
HG_{04}	0.00
HG_{40}	0.00

Total offset: 0.05 nm.

investigating the influence of defects on offset generation. After the optical defect was introduced, the input beam parameters were left unchanged. This is shown in Fig. 3.7, where the circulating power is plotted as a function of the change in the cavity length relative to the desired operating point. Fig. 3.8 shows the complex amplitudes of all the components of the beam in terms of phase and amplitude. The amplitudes are normalised for ease of representation and visualisation; all figures and tables in this section display

only the HOMs that significantly contribute to the creation of the offset for each set-up. After the defect was introduced, we adjusted the cavity length to optimise the circulating power. Essentially, we aligned the system with its target operating point. For each HGM, the complex amplitudes of the main laser and the sidebands were combined according to Eq. 3.3.5. This was done to determine the contribution of each mode to the PDH signal $\epsilon_{\mathrm{PDH},nm}$. The total PDH signal is shown in Fig. 3.9, along with the contribution of each mode. In both the marginally stable cavity and the stable cavity cases, the total error signal shows a visible offset. It is worth highlighting again that the system is tuned to the desired operating point, where the circulating power within the cavity is at its peak. At this position, the error signal is not zero, and by "offset", we mean the difference in length between the point where the error signal is zero and the desired working conditions $\delta z = 0$. To quantify the offset in metres, the value of the contribution of each mode at $\delta z = 0$ was divided by the DC gain of the signal; the results are shown in the Tab. 3.1. All modes contribute to the creation of the offset, including the fundamental one. This result is particularly intriguing, as it reveals an intrinsic limitation in the error signal that cannot be addressed solely by correct tuning of control systems or filtering out HOMs.
Later in the chapter, we delve into a similar study centred on the Virgo detector. Our findings underscore that within the complete interferometer setup, the fundamental mode is the predominant contributor to the offset. Given its pivotal role and its fundamental nature, our subsequent analysis will be dedicated to pinpointing the origins of this offset within the fundamental mode.

3.4.1 Considerations of energy conservation and its impact on error signal offsets

As we aim to comprehend the origin of the offset in the fundamental mode, all the considerations and graphs in this section refer to the HG_{00} mode. For ease of comparison, we show in Fig. 3.10 the reflected power of the main laser (in the fundamental mode) and the corresponding error signal (in

the same mode). The figure is shown only for the marginally stable setup because the offset is larger and easier to visualise. Let us remember that the system is tuned to the desired operating point and $\delta z = 0$ corresponds to the peak of the circulating power, which, as visible in Fig. 3.7, matches the peak of the circulating power in the fundamental mode. It should be noted that at the point $\delta z = 0$, even though the circulating power is at its peak, the reflected power is not at its minimum. Additionally, the zero of the error signal occurs for the tuning of the cavity length that is double compared to the value for which the minimum of the reflected power occurs. In this section, we offer an analytical interpretation to explain two key observations: 1) the lowest point of the reflected power does not coincide with the peak of the circulating power and 2) the error signal zeros out at a length tuning that is double the value where the minimum reflected power is observed. Furthermore, the proposed conceptualisation can serve as a foundation for future numerical or analytical tools aimed at quantitatively estimating the offset for a specific set-up.

Starting from the equations for a single cavity, we illustrate how defects can change the phase relationship between the reflected beam and the one that circulates within a cavity. With reference to Fig. 3.11, the amplitude at every point within a cavity can be easily calculated by combining fields through superposition. The complete set of equations can be formulated as follows:

$$\begin{aligned} a_1 &= i t_1 a_0 + r_1 a_3' \\ a_1' &= \exp[-ik(L + \delta z)] a_1 \\ a_2 &= i t_2 a_1' \\ a_3 &= r_2 a_1' \\ a_3' &= \exp[-ik(L + \delta z)] a_3 \\ a_4 &= r_1 a_0 + i t_1 a_3' \end{aligned} \tag{3.36}$$

Here, δz is the tuning of the cavity length. The incoming circulating field

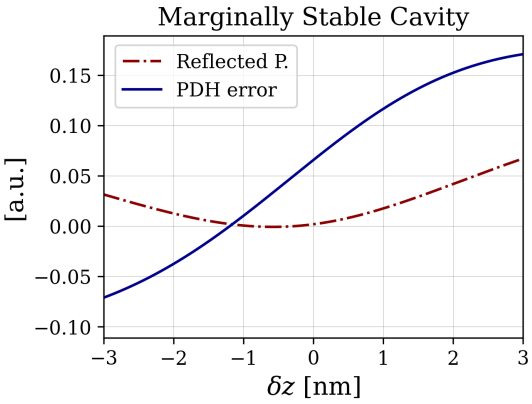

Figure 3.10: Power reflected by the cavity (in log scale) and the fundamental mode error signal. The y-axis is in arbitrary units, as it aids in visualising the important information that resides on the x-axis. The error signal is null at 1.2 nm, while the minimum of the reflected power occurs at half of that tuning. The zero of the x-axis is referenced to the point where the circulating power is at its maximum. For such tuning, the reflected power is not at its minimum.

that falls onto the input mirror a_3' can now be determined as follows:

$$\begin{aligned} a_3' &= \exp[-ik(L+\delta z)]\, a_3 = \exp[-ik(L+\delta z)]\, r_2 a_1' \\ &= \exp[-ik(L+\delta z)]\, r_2 a_1 = \exp[-ik(L+\delta z)]\, r_2 (it_1 a_0 + r_1 a_3') \end{aligned} \tag{3.37}$$

This consequently produces the following.

$$a_3' = a_0 \frac{ir_2 t_1 \exp[-i2k(L+\delta z)]}{1 - r_1 r_2 \exp[-i2k(L+\delta z)]} \tag{3.38}$$

Hence, we can proceed to calculate the amplitude of the reflected field as follows:

$$a_3' = a_0 \frac{ir_2 t_1 \exp[-i2k(L+\delta z)]}{1 - r_1 r_2 \exp[-i2k(L+\delta z)]} \tag{3.39}$$

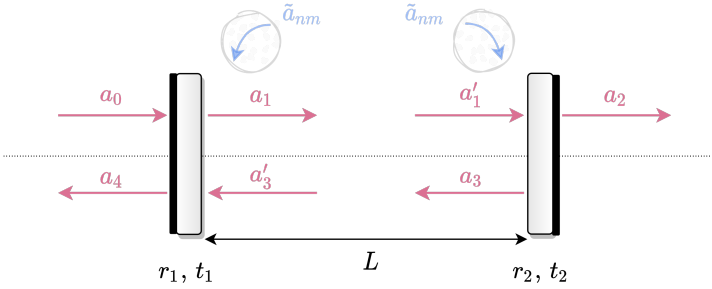

Figure 3.11: Basic diagram of a dual mirror cavity. The two mirrors are determined by their reflection and transmission amplitude coefficients. Moreover, the resultant enclosure is defined by its length L. Blue arrows refer to the case in which defects are present. The field $\tilde{a}_{nm}$ is the result of the backscattering from mode nm.

Thus, the reflected field can be expressed in the following manner:

$$a_4 = a_0 \frac{r_1 - r_2(r_1^2 + t_1^2)\exp[-i2k(L + \delta z)]}{1 - r_1 r_2 \exp[-i2k(L + \delta z)]} \tag{3.40}$$

If we assume resonance conditions, $L = L_{\text{res}} = (N\lambda)/2$, it can be observed that the reflected and transmitted amplitudes reach their minimum and maximum values, respectively, for the same tuning $\delta z = 0$. As trivial as this result may appear, it is made possible by well-defined phase relationships between the reflected and transmitted beams by an optic. Taking the beam a_1 as an example, we have implicitly assumed in Eq. 3.4.1 that it could be written as:

$$a_1 = \tau a_0 + \rho a_3' = i t_1 a_0 + r_1 a_3' \tag{3.41}$$

Therefore, we defined the optics' transmission and reflection coefficients to be $\tau = i t_1$ and $\rho = r_1$, with $0 \leq r_1, t_1 \leq 1$. These two coefficients, ρ and τ, have a phase difference of $\pi/2$, as explained in [49]. This phase relationship is deduced from energy conservation and ensures that interference between

the terms $it_1 a_0$ and $r_1 a_3'$ does not result in energy creation.
In the case of defects, the situation remains similar but not analogous. The difference is that there is another beam to consider, namely the beam scattered from the HG_{nm} mode back to the fundamental mode. The process of scattering and then backscattering occurs inside the cavity. We assume that this redistribution to the fundamental mode occurs in the same manner on the inner side of both the input and output optics, as illustrated in Fig. 3.11. We will now focus our discussion on the input optics. This is sufficient to formulate our argument, and the reasoning that follows can also be extended to the output optics. Nevertheless, it should be emphasised that in the process leading to the generation of an offset, the role of the output optics is not as significant as that of the input optics. This is because the PDH scheme uses the beam reflected from the cavity to produce an error signal. Now, the beam propagating away from the input optics is given by the superposition of three beams:

$$a_1 = \tau a_0 + \rho a_3' + \tilde{a}_{nm} \tag{3.42}$$

The phase relationship among all these three beams is constrained by energy conservation, ensuring that no energy is created through interference. In other words, energy conservation dictates the phase relationship between τa_0, $\rho a_3'$, and $\tilde{a}_{nm}$. This means that, depending on the phase value of $\tilde{a}_{nm}$, the phase relationship between ρ and τ can deviate from the canonical $\pi/2$[1]. To account for possible variations, we rewrite the phase difference between ρ and τ as:

$$\arg(\rho) - \arg(\tau) = \frac{\pi}{2} + \varphi \tag{3.43}$$

where φ is the deviation of the phase relationship from $\pi/2$, and it depends

[1] Specifically, this phase relationship deviates from $\pi/2$ when $\tilde{a}_{nm}$ is not in phase with ρ (or with τ). If, for example, the backscattered beam were in phase with the one transmitted by the optics, the two beams could simply be added together and rewritten as a single beam. The problem then becomes that of two overlapping beams, which is identical to the defect-free case, where the phase relationship between ρ and τ is $\pi/2$.

on the phase of $\tilde{a}_{nm}$; for the sake of simplicity in notation, we have omitted this dependency. We will show later that deriving φ enables derivation of the offset in the error signal.
Given its dependence on the phase of $\tilde{a}_{nm}$, a highly setup-specific quantity, φ also strongly depends on the optical configuration. For this reason, we limit the rest of our analysis to the assumption that φ is non-zero and formulate the consequences. Such conceptual work can serve as a basis for a future numerical tool aimed at quantifying offsets for a specific set-up. The logic of such a tool should be: 1) calculate $\tilde{a}_{nm}$, and thus its phase, 2) apply the conservation of energy to derive φ.

Now that we have introduced the term φ, we rewrite the transmission coefficient as:

$$\tau = it \rightarrow ie^{i\varphi}t$$

We reiterate that the term φ accounts for the change in the phase relationship between the beam reflected and transmitted by an optic compared to the defect-free scenario. Eq. 3.4.1 becomes:

$$\begin{aligned}
a_1 &= ie^{i\varphi}t_1a_0 + r_1a_3' \\
a_1' &= \exp[-ik(L + \delta z)]a_1 \\
a_2 &= ie^{i\varphi}t_2a_1' \\
a_3 &= r_2a_1' \\
a_3' &= \exp[-ik(L + \delta z)]a_3 \\
a_4 &= r_1a_0 + ie^{i\varphi}t_1a_3'
\end{aligned} \tag{3.44}$$

For notation simplicity, we have omitted the term $\tilde{a}_{nm}$. The amplitude of the backscattered beam is typically negligible compared to that of the other beam components. Therefore, we consider that its only effect is the alteration of the phase relationship between ρ and τ. By following straightforward algebraic steps similar to those carried out earlier, we can express the transmitted

beam as:

$$a_3' = a_0 \frac{ie^{i\varphi} r_2 t_1 \exp[-i2k(L + \delta z)]}{1 - r_1 r_2 \exp[-i2k(L + \delta z)]} \tag{3.45}$$

The reflected beam is:

$$a_4 = a_0 \frac{r_1 - r_2(r_1^2 + t_1^2)\exp\{-i2[k(L + \delta z) + \varphi]\}}{1 - r_1 r_2 \exp[-i2k(L + \delta z)]} \tag{3.46}$$

In this case as well, we relate the system to resonance conditions assuming $L = L_{\mathrm{RES}}$. From the two preceding equations, it is evident that the minimum of the reflected beam and the maximum of the circulating one cannot occur at the same tuning of δz. Specifically, the reflected beam reaches its minimum for the tuning:

$$\delta z = -\frac{\varphi}{k} \tag{3.47}$$

So far, we have shown that a change in the phase relationship between ρ and τ can account for one of the observations made in the previous section: The minimum of the reflected power does not align with the peak of the power circulating in the cavity. Now, we will demonstrate how it can also replicate the second observation, namely that the zero of the error signal occurs at twice the tuning where the power is at its minimum.

The role of the input optic

The beam read by the PDH scheme is the one reflected by the cavity, that is, a_4. This beam is the result of the superposition of two beams: a first beam that does not enter the cavity but is directly reflected by the input optics and a second beam that leaks out from the cavity after having propagated within it. We will call the first beam $a_{4,1}$ and the second $a_{4,2}$. It is known that the PDH signal is a reading of the phase difference between these two beams [32]. Phase differences are due to the different optical paths experienced by the two beams. Compared to the beam $a_{4,1}$, the beam $a_{4,2}$ is 1) transmitted by

the input optic, 2) propagates through the cavity, and 3) is then transmitted again by the input optics. This propagation chain is schematised below.

$$\xrightarrow[\text{Transmission}]{\text{Input optic}} \frac{\pi}{2}+\varphi \xrightarrow[\text{Propagation}]{\text{Cavity}} \delta\phi \xrightarrow[\text{Transmission}]{\text{Input optic}} \frac{\pi}{2}+\varphi$$

Relative to the $a_{4,1}$ beam, $a_{4,2}$ collects a $\pi/2+\varphi$ phase in transmission from the input optics, accumulates a phase difference during propagation in the cavity that we denote as $\delta\phi$, and finally collects another factor $\pi/2+\varphi$ in transmission from the input optics when it exits the cavity. Therefore, the overall phase difference between $a_{4,1}$ and $a_{4,2}$ can be written as:

$$\Phi = \pi + 2\varphi + \delta\phi \tag{3.48}$$

Let us start with the analysis of the case without defects $\varphi = 0$ where we assume the resonance of the cavity $\delta\phi = 0$. The phase difference between $a_{4,1}$ and $a_{4,2}$ is π. The two beams interfere destructively, therefore, the reflected power is at its minimum and under these conditions the PDH error signal is null. In fact, to be precise, the PDH signal is a reading of the phase difference Φ with respect to π: when $\Phi = \pi$ then the error signal is null $\epsilon_{\text{PDH}} = 0$. Therefore, we rewrite the PDH error signal as follows.

$$\epsilon_{\text{PDH}} = D_{\text{DC}}\left(\frac{\Phi-\pi}{k}\right) \tag{3.49}$$

In the case without defects, the previous equation becomes:

$$\epsilon_{\text{PDH}} = D_{\text{DC}}\left(\frac{\delta\phi}{k}\right) \tag{3.50}$$

In this case, the PDH signal is a reading of the phase difference between $a_{4,1}$ and $a_{4,2}$ accumulated during the propagation of $a_{4,2}$ in the cavity. When the beam is in resonance in the cavity, this phase difference is null and therefore the error signal is null in turn. Instead, in the case where defects are present

and $\varphi \neq 0$, the PDH signal is:

$$\epsilon_{\mathrm{PDH}} = D_{\mathrm{DC}} \left(\frac{\delta\phi + 2\varphi}{k} \right) \tag{3.51}$$

The error signal is zero at the tuning:

$$\delta z = -\frac{2\varphi}{k} \tag{3.52}$$

This is, in other words, the value of the offset which, as intended to demonstrate, corresponds to twice the tuning at which the reflected power reaches its minimum.
This way of thinking about the problem, albeit simplistic, makes clear the pivotal role of the input optics in the process leading to the creation of an offset. Since the beam $a_{4,2}$ is transmitted twice by the input optics, it collects an additional phase factor 2φ compared to the case without defects. This extra phase factor is effectively the offset.

As further support for this conceptualisation, we present Fig. 3.12. This is obtained only by numerical modelling with FINESSE and without using any of the equations in this section. The figure is associated with the marginally stable PDH setup in Tab. 3.2, whose description is given in Section 3.4, along with our modelling methodology. The graph shows the phase difference φ as the optical imperfection varies. As explained above, φ is the phase difference between ρ and τ relative to $\pi/2$. This can be mapped one-to-one with the error signal, demonstrating that φ is the origin of the offset.

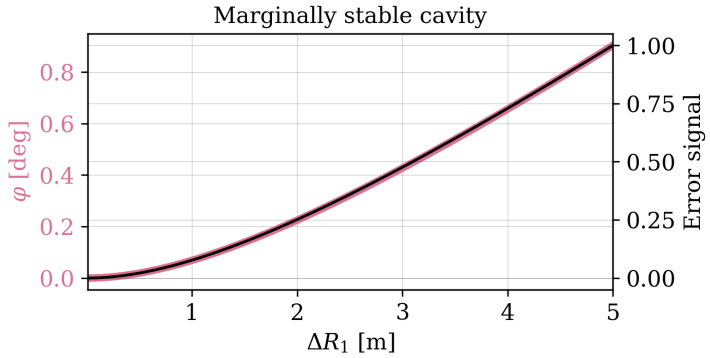

Figure 3.12: The figure depicts the phase difference between reflected and transmitted beams via the input optics, namely $a_{4,1}$ and $a_{4,2}$. The phase difference is relative to 90° and is shown as the RoC of the input optics increases. The figure also displays the amplitude of the PDH error signal (for the fundamental mode) as the optical imperfection increases; its amplitude is normalised. The black curve is effectively a measurement of the offset as the imperfection increases. For each data point the system was tuned to the desired operating point. In spite of this, the error signal is not zero, indicating an offset. This offset can be directly mapped to φ on a one-to-one basis. This figure obtained solely through numerical modelling using FINESSE.

3.5 Offset creation within Virgo interferometer

This section is a summary of several investigations that began while I was at the Virgo site from February 2021 to October 2021 and continued even after I left the site. The primary goal was to identify the presence of offsets in the control loops. We explored various possibilities, such as whether the control design was correct, whether there were couplings that we had not modelled, and so on. However, in the end, we were able to model comparable offsets in the error signals resulting from HOMs coupling. We will show how we came to this conclusion and outline the key simulations that we performed along the way.

3.5.1 The detector and its DoFs

Fig. 3.13 illustrates a simplified diagram of the dual recycled configuration in the Advanced Virgo Plus (AdV+) detector, indicating the lengths that need to be controlled. The DoFs associated with these lengths are as follows.

$$\begin{aligned}
\text{DARM} &= L_N - L_W \\
\text{CARM} &= \frac{L_N + L_W}{2} \\
\text{MICH} &= l_N - l_W \\
\text{PRCL} &= l_P + \frac{l_N + l_W}{2} \\
\text{SRCL} &= l_S + \frac{l_N + l_W}{2}
\end{aligned} \tag{3.53}$$

where DARM stands for Differential ARM length; this controls the difference in length of the two arm cavities and is used to get the best interference between the two arms at the dark port. CARM stands for Common ARM length; its tuning sets the average length of the arm cavities and is used to keep the arms on resonance. MICH stands for MICHelson; its tuning controls the short arms of the Michelson (between the ITMs and beam splitter) and determines the fringe at the output port. Generally, the Michelson is operated on the dark fringe. PRCL stands for Power Recycling Cavity Length; the power recycling cavity is operated on resonance to maximise the power coupled to the central interferometer. SRCL stands for Signal Recycling Cavity Length; it is used to control the operation of the signal recycling cavity. The operating point of the SRCL depends on the mode of operation of the interferometer. It can be adjusted to increase the detector's sensitivity around a specific frequency, or alternatively, it can be used to widen the entire bandwidth of the detector. For our analysis, we assume that the SRC is operated under the latter conditions. The detector bandwidth is determined by the SRC-Arms system. This coupled cavity system operates in a regime fundamentally different from that described in Section 2. Due to the low

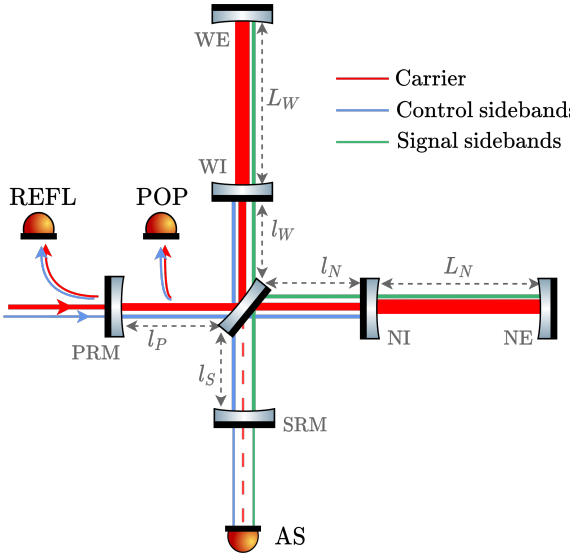

Figure 3.13: Simplified layout of the dual recycled Fabry-Perot Michelson of AdV+, illustrating the fields within the interferometer. This representation highlights the position of critical photodiodes: REFL (REFLected port), POP (power recycling Pick off Port), and AS (antisymmetric port). The diagram illustrates the paths traversed by different light fields within the interferometer. The carrier resonance occurs within the arm cavities and the power recycling cavity, while the Fabry-Perot Michelson is finely tuned to approach the carrier dark fringe. Meanwhile, the RF sidebands used for control purposes resonate within the recycling cavities but experience reflection from the arms. Note that the Michelson configuration deviates from the dark fringe for the control sidebands, leading to their presence both in both the signal recycling cavity and at the Michelson output. In particular, the signal sidebands, generated by gravitational waves, originate within the arm cavities and eventually exit Michelson via the antisymmetric port.

finesse of the SRC and the shorter length compared to the arms, light spends considerably less time within the SRC than in the arms. This allows the

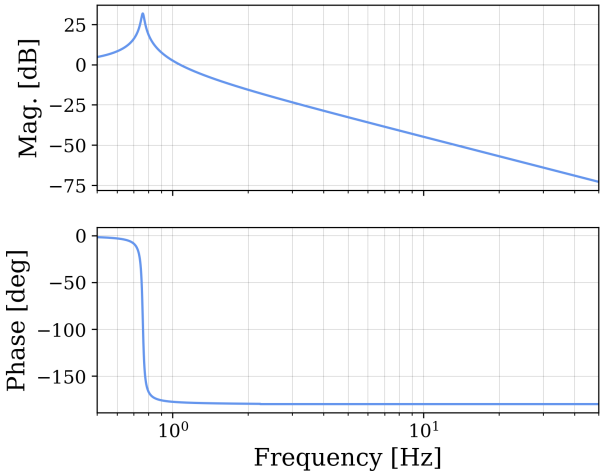

Figure 3.14: Mechanical response of the last stage of the suspension chain. From now on, we will exclusively refer to the term *suspension* or *mechanics* in relation to this stage. Regarding the mechanical parameters of the suspension, its mass is $m = 42$ kg. The resonance frequency is $f_M = 0.76$ Hz. The quality factor of the suspension is $Q = 40$, which is related to the damping ratio as $Q = 1/2\gamma$.

SRM-ITM optics to be treated as a single compound mirror, whose reflectivity is lower than that of the individual TM. Consequently, the SRC-Arm system can be conceptualised as a single cavity with a lower finesse compared to that of the individual arm cavities, which implies a higher bandwidth.

3.5.2 The DARM optomechanical response

The major upgrade made to the Virgo detector ahead of the fourth observational run involves the incorporation of the signal recycling mirror into the optical layout. The SRM functions by redirecting the signal that emerges from the AS port back into the arm cavity, thus recycling the signal [50]. The presence of the SRM results in radiation pressure effects similar to those described in Section 3.2. The differential motion of the TMs at a frequency

ω creates signal sidebands at a frequency $\pm\omega$ relative to that of the main laser. As shown in Fig. 3.13, signal sidebands originate within arm cavities and, in the presence of SRM, are directed back into arm cavities. Inside the arm cavities, the beating between the signal sidebands and the carrier generates a frequency-dependent radiation pressure force at the signal frequency ω, which acts on the TMs. This optically generated force can be related to frequency-dependent stiffness, which is typically called ponderomotive rigidity [51].

Through a simple change of basis, the differential movement of two TMs can be described as the movement of a single DoF, which is DARM. In terms of the dynamics of this DoF, the motion of DARM can be described as that of a single TM anchored to a suspension identical to the one used for the individual TMs. As shown in [52], the introduction of the SRM introduces an optically induced stiffness, as just mentioned. As in the simple cavity case, the system consists of an optomechanical setup where the equivalent TM is anchored to two harmonic oscillators connected in parallel: the suspension and the optical spring. The equations of motion of the system are those of Eq. 3.19, which we repeat below for clarity.

$$\{-m\omega^2 + 2im\gamma\omega + K\}z(\omega) = F(\omega) \tag{3.54}$$

Here, z denotes the DARM motion. The transfer function that maps an external force to the generated motion is simply given as:

$$\frac{z(\omega)}{F(\omega)} = (-\omega_0^2 + 2im\gamma\omega + \omega^2)^{-1}\, m^{-1} \tag{3.55}$$

with

$$K = K_{\mathrm{M}} + K_{\mathrm{OPT}}$$
$$\gamma = \gamma_{\mathrm{M}} + \gamma_{\mathrm{OPT}}$$

Fig. 3.14 illustrates the transfer function that maps a differential force

applied to the TMs of the Virgo detector to their generated differential motion. We will refer to this as the *optomechanical response of DARM*. This was calculated using the AdV+ FINESSE model in the case where the effects of radiation pressure are null, that is, $K_{\mathrm{OPT}} = 0$ and $\gamma_{\mathrm{OPT}} = 0$. Therefore, the frequency response shown in the figure is purely mechanical, and specifically, it is the transfer function of the last stage of the suspension chain that suspends the optics. The same result can be obtained using Eq. 3.55 by setting $K = K_{\mathrm{M}}$ and $\gamma = \gamma_{\mathrm{M}}$. To minimise the impact of ground vibrations on optics, a multistage seismic isolator, called the superattenuator, is employed; its characteristics are detailed in [53]. The last stage is primarily affected by the impact of radiation pressure on the optics, which led us to focus on our analysis here.

In the single-cavity case, it is the variations in cavity length relative to the resonance conditions of the main laser that determine the effects of radiation pressure, making K_{OPT} and γ_{OPT} non-zero. In the case of the signal-recycled detector, we are interested in the variation in length of the SRC. The operating conditions for which the signal sidebands are resonant in the SRC are known as Resonant Sideband Extraction (RSE). Under these conditions, the optical stiffness and damping are null. Fig. 3.15 shows the variation of the optomechanical response of DARM with changing SRCL. In this case, as in all subsequent ones presented in this chapter, the optomechanical response of DARM was calculated using FINESSE, which includes the effects of radiation pressure in the simulation. Specifically, FINESSE was used to calculate K_{OPT} and γ_{OPT} and incorporate them into the calculation of the optomechanical response.

3.5.3 Offsets and the longitudinal optical spring

To ensure the operational functionality of the detector, a remarkable degree of stability between the relative position of the optics is crucial. To meet these rigorous demands, the use of feedback control becomes essential in maintaining the required stability. The control loops keep the detector at a point where the error signals for the five DoFs are zero. Consequently,

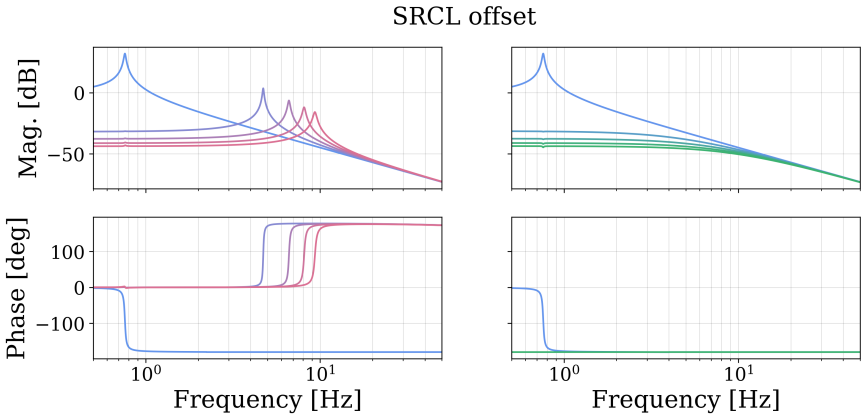

Figure 3.15: Optomechanical response of DARM while setting an offset on SRCL. The offset is relative to the RSE conditions. Blue denotes that there is no offset, red indicates increasing offsets that extend the SRC length (left), and green represents offsets that decrease the SRC length. In both cases, the offset ranges from 0 to 5 nm. In both cases, the radiation pressure renders the system unstable, although it does so in different ways. For increasing tunings, the system is unstable due to a negative damping coefficient. This instability is evident from the positive phase flip from 0 to 180 degrees in the transfer functions. Similarly, decreasing tunings reveal a system with negative stiffness. This is intuitively visible from the phase: when a force is applied, the system drifts away. These behaviors for the transfer functions can be easily verified by Eq. 3.55.

if these signals exhibit an offset, the control loops would keep the system operating at a point that is not the desired one. Being close but not precisely at the operating point can lead to variations in the optomechanical response of DARM.

Similarly to the case of a simple cavity, we show that the presence of optical imperfections results in the creation of offsets. This, in turn, has repercussions on the optomechanical response of DARM. It is worth noting that the significance of offsets in determining radiation pressure effects emerges pri-

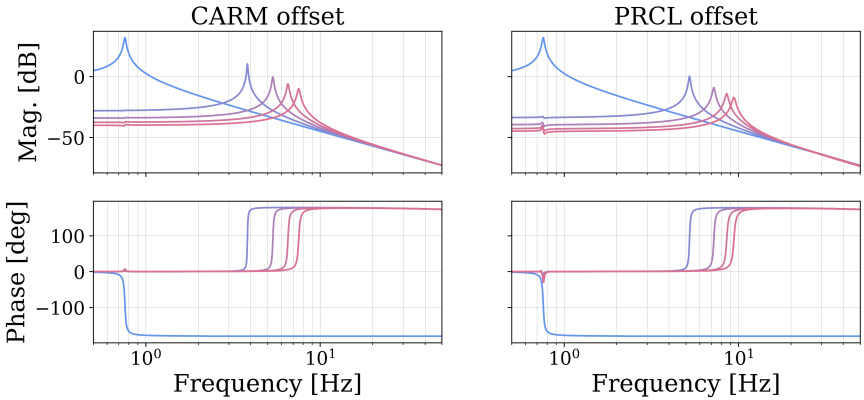

Figure 3.16: Optomechanical response of DARM while setting an offset on CARM and PRCL. Blue denotes that there is no offset, and red indicates increasing offsets that extend the length of the arm cavities and the PRC, respectively. For CARM, the offset ranges from 0 to 0.25pm; for PRCL, the offset ranges from 0 to 0.5nm. The sensing scheme considered is the one currently implemented in the FINESSE package for modelling Virgo[54], which is based on [55]. This figure shows that offsets in other DoFs cause an offset on the SRCL, leading to a noticeable change in the DARM response. This linkage between various DoFs and SRCL is a result of cross-couplings in sensing. In other words, the SRCL error signal is sensitive to the position of other DoFs in addition to SRCL itself.

marily due to the introduction of the SRM. This optics inherently introduces radiation pressure effects. In the case of defects, offsets in the error signals would appear even without the SRM. However, this would not cause the SRCL to detune, a process that leads to radiation pressure effects.

As mentioned earlier, SRCL has the greatest impact on altering DARM's optomechanical response. Thus, we begin our discussion by focussing on its error signal. The control sidebands shown in Fig. 3.13 are those used to generate the error signal of SRCL. Under normal operating conditions,

these sidebands resonate within both recycling cavities. To generate the error signal, the photodetector signal at the REFL port is demodulated at the corresponding modulation frequency. In a sense, the SRCL error signal is a PDH-like error signal where the sidebands assume the conventional role of the carrier and vice versa; its purpose is to maintain the resonance of the control sidebands. Such resonance conditions are used as a probe to infer the RSE conditions for the signal sidebands: the resonance of the control sidebands corresponds to the resonance of the signal sidebands. Drawing a parallel to the case described in Section 3.4.1, we expect that scattering to, and backscattering from, HOMs can result in a change in the phase relationship between the control sidebands reflected and transmitted by the PRM. If this phase relationship deviates from $\pi/2$ by a certain amount φ, the SRCL error signal reads an additional phase delay of 2φ, resulting in the creation of an offset. This hypothesis aligns with our simulation results but requires further investigation.

The reasoning we have just outlined can easily be extended to all error signals collected at the REFL port. This might suggest that collecting the SRCL error signal at the POP could immunise the signal from offsets, which, however, is not the case. The phase relationship of $\pi/2$ is specifically a constraint on the phase difference between the reflected and transmitted beam by an optic. There is no such constraint on the individual phases of these beams. They can assume any value, as long as the difference between them remains $\pi/2$. For the PRM and the control sidebands it transmits and reflects, a deviation from the $\pi/2$ phase relationship implies that both the reflected and transmitted sideband phases can change. Altering the phase of the transmitted sidebands consequently leads to a change in the phase relationship between the control sidebands and the signal sidebands. If this relationship shifts, the control sidebands are no longer a reliable probe for inferring the resonance conditions of the signal sidebands within the SRC. Therefore, even collecting the SRCL error signal at the POP cannot guarantee a null error signal at the desired operating point.

Until now, we have discussed the consequences of an offset in the SRCL error signal on the optomechanical response of DARM. However, in principle,

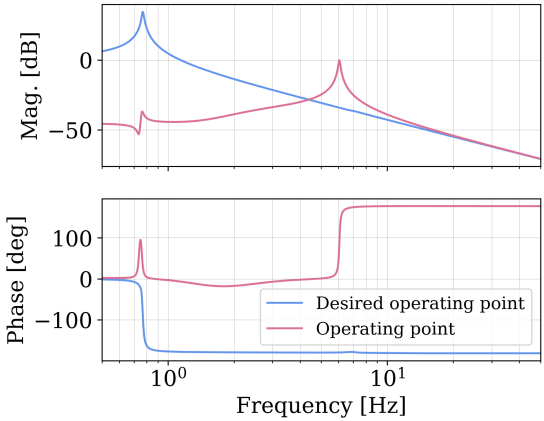

Figure 3.17: Both the blue and red curves represent the optomechanical response of DARM after introducing an optical imperfection. Specifically, the RoC of the PRM has been expanded by 2 m from its design value. In the blue curve case, all five DoFs are adjusted to the point where radiation pressure effects are eliminated. The error signals corresponding to this tuning of the system are shown in Fig. 3.18. In the red curve case, the system is tuned to the point where the error signals become null.

even offsets in the error signals of the other DoFs can lead to changes in the optomechanical response. Let us consider a scenario where one of the remaining four DoFs, excluding the SRCL, experiences an offset. If the SRCL error signal is sensitive to that specific DoF, the fact that it is not at its operating point will result in a nonzero error signal for SRCL. In other words, if an offset occurs in one of the other DoFs, it can cause an offset on SRCL due to coupling in sensing, which in turn affects the optomechanical response of DARM. As an example of this effect, we show Fig. 3.16, which illustrates the change in the optomechanical response when setting an offset on CARM and PRCL.

More generally, the presence of defects can induce offsets in all error signals of all DoFs, and an accurate assessment of the offset in SRCL requires

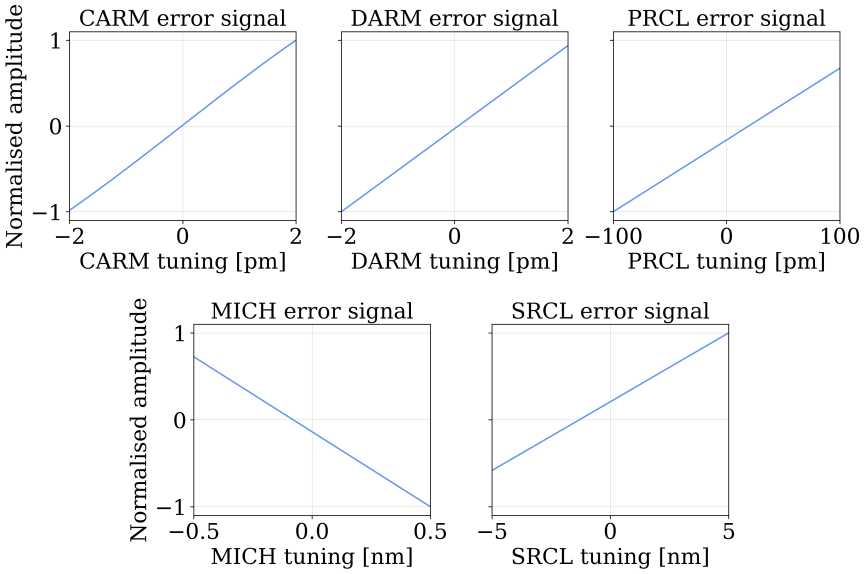

Figure 3.18: The figure illustrates the error signals of each DoF in relation to the tuning of their respective DoF. These error signals were calculated after increasing the RoC of the PRM by 2 m and readjusting the system to the point where the radiation pressure effects are null. In fact, the zero-tuning position is referenced to the desired operating point, which corresponds to the blue optomechanical response in Fig. 3.17.

considering the couplings in sensing among all the DoFs. For the sake of completeness in the discussion, it should be added that an offset in the other DoFs may have an inherent role in determining the impact of radiation pressure on mechanics, in addition to just causing an offset in SRCL. The force of the radiation pressure is determined by the beating of the carrier with the signal sidebands. These beams are influenced by the tuning of all DoFs. Hence, although to a lesser extent than SRCL, all DoFs play a role in shaping the optomechanical response of DARM.

Table 3.3: On the left, the offset in the error signal of each DoF relative to the desired operating point. On the right, the contribution per HOM to the SRCL error signal.

DoF	Offset [pm]
CARM	−0.01
DARM	0.06
PRCL	20.0
MICH	−80.0
SRCL	−1317

SRCL error signal

Mode	Offset [pm]
$\mathbf{HG}_{00}$	−1369
$\mathbf{HG}_{02}$	26
$\mathbf{HG}_{20}$	26

3.5.4 Offset creation

Applying the same approach as in the single-cavity scenario, we intentionally introduce an optical defect into the detector's optics to investigate its connection to the generation of offsets in the error signals. The results are particularly fascinating because they underscore that the issue is primarily driven by the fundamental mode.

As a case study, we extended the RoC of the PRM by two metres beyond the design value. At this stage, it is beneficial to establish some terminology to suit the context of the interferometer. By the *operating point* we refer to the configuration where all five DoFs are tuned to render all error signals null. On the contrary, the *desired operating point* is where the radiation pressure effects become null $K_{\mathrm{OPT}} = 0$ and $\gamma_{\mathrm{OPT}} = 0$; see Fig. 3.17. At this point, the optomechanical response of DARM aligns precisely with the mechanical response of the suspension. Fig. 3.18 shows the error signals relative to the desired operating point. To varying degrees, all signals are influenced by the defect, although the SRCL one is the most affected, displaying a pronounced offset. Tab. 3.3 reports the deviation of each signal's zero point from the desired working point. Since the SRCL signal is the most affected and plays a dominant role in the reshaping of the optomechanical response, the table also presents the contributions to the signal per HOM.

Unlike the single-cavity scenario, most of the effect is concentrated in the fundamental mode. This phenomenon is a result of the fact that the PRC

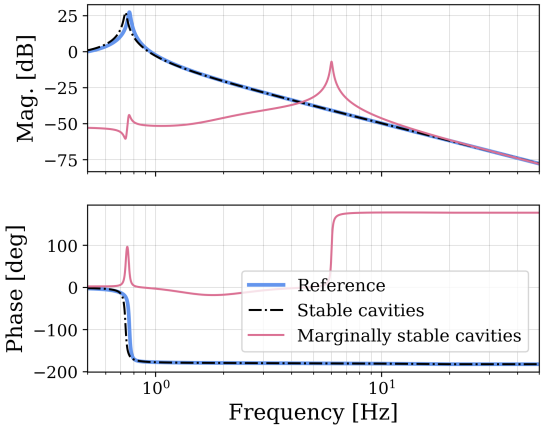

Figure 3.19: Both the black and red curves represent the optomechanical response of DARM after introducing an optical imperfection. Specifically, the RoC of the PRM has been extended by 2 m beyond its design value. When we refer to "stable" and "marginally stable", we refer to the stability of the recycling cavities. In both the black and red cases, the system is tuned to the operating point where error signals are zero. It is evident that, when the same imperfection is introduced, offsets are more pronounced in the case of marginally stable cavities.

effectively suppresses the HOMs of the carrier beam. To explain this concept, let us consider the case where a defect generates HOMs within the PRC. In terms of the carrier, it is transmitted into the arm cavities and propagates within them. Because these cavities are stable, the HOMs of the carrier accumulate a certain amount of Gouy phase, making them off-resonance. Therefore, when the fundamental mode and the higher-order modes are transmitted back into the PRC, the HOMs have accumulated a certain phase difference compared to the fundamental mode. Since the PRC is marginally stable, the HOMs almost do not accumulate any additional phase difference compared to the fundamental mode, and thus, if they were off-resonance, they remain off-resonance. As a result, a significant portion of the power is scattered back to the fundamental mode. The situation is different for the

HOMs of the sidebands. These beams do not enter the arm cavities. The PRC is marginally stable, and therefore the HOMs almost do not accumulate a phase lag relative to the fundamental mode. As a result, the HOMs resonate with the fundamental mode. Although a substantial amount of power from the sidebands remains distributed in the HOMs, only a small amount of carrier power remains distributed in the HOMs. Therefore, the carrier-sidebands beating per HOM contributes only minimally to the error signal due to the suppression of the carrier modes by the PRC.

The simulation described in this section was repeated by forcing the recycling cavities, which are marginally stable, to behave as if they were stable. By this, we mean that we have deliberately forced the HOMs to accumulate a 20° Gouy phase within the current recycling cavities. The results are shown in Fig. 3.19, which shows the optomechanical response of DARM after enlarging the RoC of the PRM by two metres. The transfer function is shown in both the case of stable and marginally stable recycling cavities. Even in the case of the full detector, the offsets are more pronounced in the case of marginally stable cavities.

In Section 3.4, we discussed how defects in the optical setup can lead to an offset in the error signal. These offsets arise because these imperfections cause optical modes to first be converted up and then back, disrupting the phase relationship between different beams. In the same section, we have shown a connection between cavity stability and the effect of defects in terms of offset creation. In this section, we have demonstrated that these effects are not limited by the complexity of the optomechanical system; they are observed in both simple and more intricate systems, such as AdV+.

3.6 Summary

In this chapter, we explored the generation of offsets in the PDH error signal caused by optical imperfections. Beginning with the scenario of a single

cavity, we have shown that all modes contribute to the creation of these offsets, including the fundamental one. This observation is particularly intriguing because it shows an intrinsic limitation in the error signal. In fact, this cannot be addressed solely by correct tuning of control systems or filtering out HOMs. From the same analysis, it was found that the system is more susceptible to offset generation in the case of a marginally stable cavity compared to a stable one. Lastly, we have shown that the origin of the offset lies in the backscattering of the HOMs to the fundamental mode. This process spoils the phase relationships between different beams, which ultimately results in an offset.

We then performed similar analysis within the Virgo detector context. Contributions from other modes were significantly reduced through the suppression of carrier HOMs within the PRC. Consequently, the only limitation left to the system arises from the fundamental mode. Similarly to the single-cavity case, this effect cannot be mitigated merely by adjusting the cavity length or filtering out HOMs. Finally, even in the case of the complete interferometer, the system exhibited greater sensitivity to offset generation for marginally stable (recycling) cavities.

4

Angular control noise in Advanced Virgo and implications for the Einstein Telescope

After a long journey through the meticulous lands of sensing, we finally arrive in the vast plains of control. It is impossible to talk about the control section without delving into the entire control loop, which leads us to take a distinct approach in comparison to other sections. Instead of targeting a specific point in the control loop, we offer a complete description of the entire system while keeping our primary focus on the control aspect. Specifically, we present the modelling of the angular control loops of Advanced Virgo (AdV), which is of interest due to its implications for the Einstein Telescope. The results of this work have been documented in a paper [14].

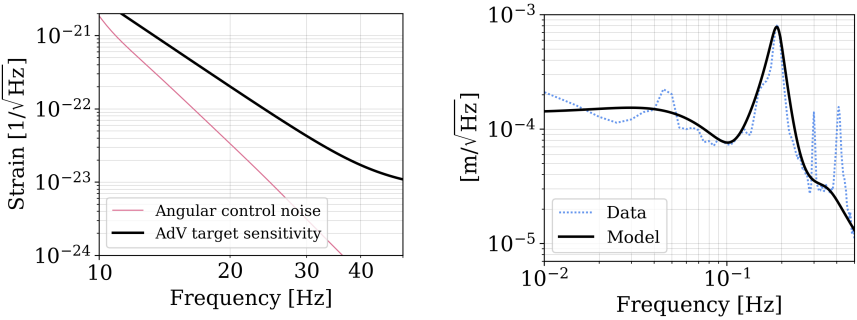

Figure 4.1: The black line represents the target sensitivity of the Advanced Virgo detector, while the red line indicates the expected level of angular control noise. This curve was calculated based on the circulating power in the cavities of 650 kW, which is approximately five times higher than that used during O3. On the right, an example of very good agreement between the model and experimental data is shown.

Efforts are currently underway to design third-generation detectors that will surpass the performance of current detectors. The Einstein Telescope, along with other forthcoming detectors, will advance gravitational wave detection capabilities to an unprecedented level, enabling the observation of previously undetectable events, such as the mergers of intermediate-mass black holes, and conducting precise tests of Einstein's theory of general relativity under extreme gravitational conditions. Nevertheless, as the objective is to surpass the capabilities of current detectors, it is logical to assume that the technical constraints inherent in existing detectors might hinder the achievement of ET's goals unless the design is carefully crafted to avoid such limitations. The significant improvement that will be brought about by ET lies primarily in the low-frequency range, where an approximately one million-fold increase in sensitivity is expected compared to current detectors. In this frequency range, the primary limitation of LIGO detectors arises from angular control noise that originates from the necessity to maintain optical alignment [56, 57, 58]. Maintaining the operational integrity of the

detector requires a high level of alignment stability between the mirrors. Using feedback control ensures that the remaining rotation of the mirrors stays sufficiently low to meet these requirements. However, this comes at the cost of generating control noise that can couple with the detector's output channel, potentially limiting its performance. Considering the significant expected improvements in this frequency range for ET, it is reasonable to assume that angular control noise may pose a limitation in achieving its target sensitivity. Therefore, it is crucial to be able to evaluate the level of this control noise for ET, and to do this, we needed a precise model. This had not been achieved previously, mainly because there was hope that simplified models would suffice. We took a different approach and developed a more detailed model based on the AdV system, which closely matches the measured data. This enables us to make predictions about ET's performance. Incidentally, our model confirmed that Virgo, unlike LIGO, is not constrained by alignment control noise, as previously shown in [59]. We decided to model the configuration of the detector known as Advanced Virgo, which is the one in use during O3. The commissioning phase for Virgo in preparation for the fourth observational run is not yet complete, and we believed that modelling a stable system that is not subject to changes was the right environment to develop our model. Through the validated model, we show that this limitation would not apply even if the detector were operating at full power; see Fig. 4.1.

In Section 4.1, we begin by explaining the fundamentals of angular control noise and how mirror rotations can lead to a length signal. We will clarify that assessing the amount of angular noise requires an understanding of the dynamics of the control loops. Therefore, we begin the description of these loops in Section 4.2, starting with their fundamental component, the plant. In particular, here, we elucidate the impact of radiation pressure on the mechanics through a mechanical model that we have developed. In Section 4.4, we present the characterisation of all external disturbances that enter the angular control loops, which are at the origin of the angular control noise. In Section 4.3, we explain the rest of the control system. In

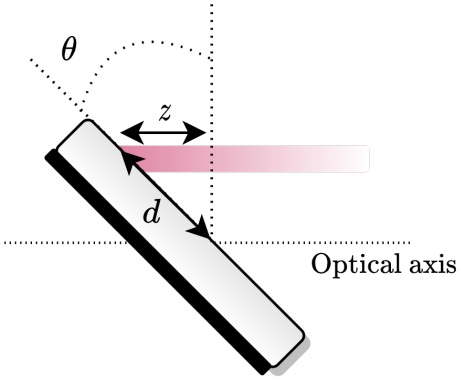

Figure 4.2: Illustration of how a rotation can alter the optical path of a beam if it is offset from the optical axis.

Section 4.5, we project the noise onto the detector's output channel, and in Section 4.6, we repeat the same process for ET, discussing the results and implications for the detector.

4.1 Angular control noise: the coupling chain

A diagram of the interferometric detector is shown in Fig. 4.3. When a gravitational wave passes through it, it induces a differential change in the length of the detector arm cavities. Similarly, any rotation of the main optics can also lead to a change in length, which can create noise that is indistinguishable from a gravitational wave. As illustrated in Fig. 4.2, this angle-length coupling can be easily understood from a geometric point of view. If the incident beam in one of the mirrors is offset by a value d, the rotation of the mirror by a small angle θ results in a corresponding change in length given by:

$$z = d\,\theta \tag{4.1}$$

Eq. 4.1 is simply an angle times a distance, which gives the change in the optical path experienced by the beam. The beam on the mirrors is off-centred due to the rotation of the optics. To illustrate the concept, let us consider the case of a single cavity with an input test mass (ITM) and an End Test Mass (ETM). As explained in [60], the Beam Spot Motion (BSM) in the test masses (TM) is related to their rotation by the following relationship.

$$[d_{\mathrm{ITM}}\, d_{\mathrm{ETM}}]^T = D \cdot [\theta_{\mathrm{ITM}}\, \theta_{\mathrm{ETM}}]^T \tag{4.2}$$

with

$$D = \frac{L}{1 - g_{\mathrm{ITM}}\, g_{\mathrm{ETM}}} \begin{bmatrix} g_{\mathrm{ITM}} & -1 \\ -1 & g_{\mathrm{ETM}} \end{bmatrix} \tag{4.3}$$

In this context, d_{ITM} and d_{ETM} indicate the displacement of the beam spot on the ITM and ETM, respectively, resulting from their rotations represented by θ_{ITM} and θ_{ETM}. The previous equation shows that the cause of the angular noise is the rotation of the optics, which causes the beam to become off-centre. Now, the remaining question is why the optics undergo these movements. External disturbances, denoted by η, enter the control loops, causing the movement of the mirrors. Therefore, Eq. 4.1 can be refined to include more specific dependencies as follows:

$$z(\theta(\eta)) = d(\theta(\eta)) * \theta(\eta) \tag{4.4}$$

The entire process unfolds as follows: external noises induce mirror movement $\theta(\eta)$, which, in turn, triggers the BSM $d(\theta(\eta))$; within a bilinear process, the BSM modulates the angular motion, ultimately producing a length signal. Eq. 4.4 shows how an angle can generate a length signal when considering a single mirror. However, when dealing with the entire detector, which comprises multiple mirrors, the situation becomes more complex. Nevertheless, this equation is adequate to grasp that two essential components are required to evaluate the amount of angular noise: identifying and characterising the input noises that cause the motion of the optics, and a

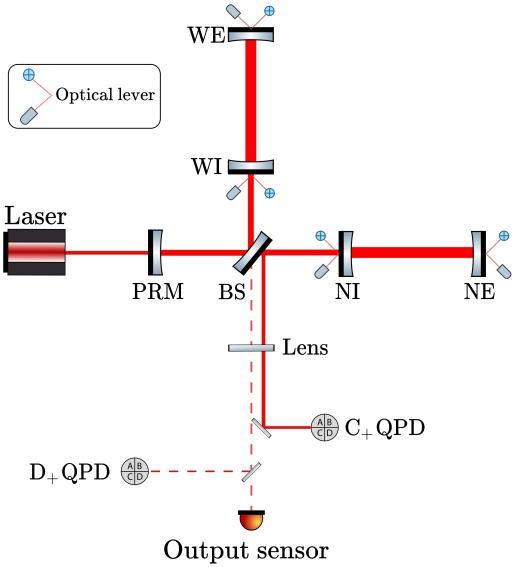

Figure 4.3: The diagram shows Advanced Virgo's optical configuration during the O3 run. The main optics consists of input test masses (NI, WI), end test masses (NE, WE), the Power Recycling Mirror (PRM), the beam splitter (BS), and a lens that was used as a placeholder for the signal recycling mirror. The diagram also indicates the positions of the alignment sensors, namely quadrant photodetectors (QPD) and optical levers (OpL).

control loop model that relates mirror motion to the set of input noises. This is because the dynamics of the optics is shaped by the entire control system. In this framework, we will begin by describing the core component of the Alignment Sensing and Control (ASC) system in the next section, which is its plant.

4.2 The opto-mechanical plant and degrees of freedom

To isolate the mirrors from ground vibrations, a multistage seismic isolator called the superattenuator is used, with its details described in [53].The lower part of the suspension consists of a steering element, the marionette, from which hang the suspended optics [61]. The actuators used in the control scheme are attached to the lower stages of the suspension chain. Thus, the mechanical response of the suspension should be considered in the context of the overall loop dynamics. During the O3 run, the control scheme used only the actuators anchored to the marionette. Therefore, we simplify our analysis by assuming that each TM is solely suspended by the last two stages of the suspension, as the dynamics of the ASC loops only involve those. We start by explaining the dynamics of a two-stage suspension system for a single test mass. This setup can be described as a double-torsion pendulum that is driven, and its equations of motion are as follows:

$$I\ddot{\theta}(t) - K\theta(t) = T(t) \tag{4.5}$$

with θ denoting the vector $[\theta_{\text{mar}}\ \theta_{\text{mir}}]$, where θ_{mar} signifies the rotation of the marionette and θ_{mir} represents the rotation of the mirror. From now on, we will use the subscript *mar* to denote the "marionette" stage and *mir* for the final stage, which is the one supporting the "mirror". In this context, I corresponds to the inertia matrix, K represents the stiffness matrix, and T represents the driving torque. Transforming these equations into the Laplace domain, we obtain the following.

$$-s^2 I\theta(s) - K\theta(s) = T(s) \tag{4.6}$$

The mechanical response of the suspension is given as the output rotation divided by the input driving torque:

$$\frac{\theta}{T} = \left(-s^2\mathbb{1} - I^{-1}K\right)^{-1} I^{-1} \tag{4.7}$$

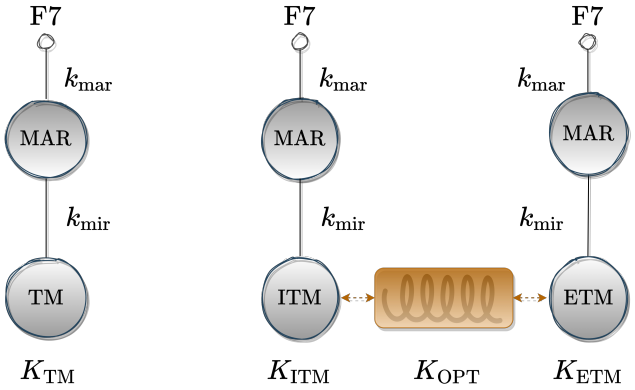

Figure 4.4: On the left, a schematic of the last two stages from the suspension of one of the TM is shown. On the right is an illustration of how the mechanical system is redefined when combined with an optical resonator. In this representation, it is understood that there is optical power circulating within the optical cavity composed of an ITM and an ETM. Both TMs are suspended through their respective suspension systems. Due to the effect of radiation pressure, the two TMs behave as if they were connected by a spring, which couples the two suspension systems. The stiffness term K_{OPT} accounts for the radiation pressure. The diagram shows the suspension point of the marionette, which is the upper stage of the suspension chain known as Filter 7 (F7).

For clarity, we rewrite the equation of motion in matrix form as:

$$-s^2\begin{bmatrix} I_{\mathrm{mar}} & 0 \\ 0 & I_{\mathrm{mir}} \end{bmatrix}\begin{bmatrix} \theta_{\mathrm{mar}} \\ \theta_{\mathrm{mir}} \end{bmatrix} - \begin{bmatrix} k_{\mathrm{mar}}+k_{\mathrm{mir}} & -k_{\mathrm{mir}} \\ -k_{\mathrm{mir}} & k_{\mathrm{mir}} \end{bmatrix}\begin{bmatrix} \theta_{\mathrm{mar}} \\ \theta_{\mathrm{mir}} \end{bmatrix} = T(s) \qquad (4.8)$$

Here, I_{mar} and I_{mir} are the moments of inertia of the marionette and mirror stage, respectively. The stiffness of each stage, namely the marionette stage and the last pendulum stage, which suspends the mirror, is denoted by k_{mar} and k_{mir}, respectively. The stiffness matrix for the suspension of each TM is

as follows:

$$K_{\mathrm{TM}} = \begin{bmatrix} k_{\mathrm{mar}} + k_{\mathrm{mir}} & -k_{\mathrm{mir}} \\ -k_{\mathrm{mir}} & k_{\mathrm{mir}} \end{bmatrix} \tag{4.9}$$

In the case of an arm cavity, two optics are suspended, which means there are four mechanical DoFs to take into account: one for the marionette and one for the mirror stage of each suspension. In each arm cavity, there is a high level of circulating optical power. As explained in [62], when a mechanical resonator of this type is combined with an optical resonator, the result is a redefinition of the mechanical system whose dynamics cannot be described without considering the influence of optics. As illustrated in Fig. 4.4, the two mirrors behave as if they were connected by a spring, cross-coupling the dynamics of the two suspension systems. The equations that govern the motion of this system can always be expressed in accordance with the framework outlined in Eq. 4.5. For the sake of simplicity in notation, we do not rewrite the entire equation of motion in extended form, but we redefine its main elements. Radiation pressure couples the suspension of the TM and that of the ETM, making it necessary to consider the motion of four mechanical DoFs instead of two. We now redefine the vector of DoFs to adapt it to the four-body case as:

$$\theta = [\theta_{\mathrm{mar,\ ITM}} \ \ \theta_{\mathrm{mir,\ ITM}} \ \ \theta_{\mathrm{mar,\ ETM}} \ \ \theta_{\mathrm{mir,\ ETM}}]^T$$

The subscripts ITM and ETM serve to reference elements in the equation corresponding to either the ITM or ETM suspension. For example, $k_{\mathrm{mir,\ ITM}}$ represents the stiffness of the mirror stage in the ITM suspension. Additionally, the inertia matrix also needs to be expanded to account for four DoFs, which we redefine as:

$$I = \mathrm{diag}(I_{\mathrm{mar,\ ITM}} \ \ I_{\mathrm{mir,\ ITM}} \ \ I_{\mathrm{mar,\ ETM}} \ \ I_{\mathrm{mir,\ ETM}})$$

In the absence of radiation pressure, the mechanical stiffness matrix for the two suspensions system is as follows.

$$K_{\mathrm{M}} = \begin{bmatrix} k_{\mathrm{mar}} + k_{\mathrm{mir}} & -k_{\mathrm{mir}} & 0 & 0 \\ -k_{\mathrm{mir}} & k_{\mathrm{mir}} & 0 & 0 \\ 0 & 0 & k_{\mathrm{mar}} + k_{\mathrm{mir}} & -k_{\mathrm{mir}} \\ 0 & 0 & -k_{\mathrm{mir}} & k_{\mathrm{mir}} \end{bmatrix} \tag{4.10}$$

The two 2×2 blocks, one in the upper left and one in the lower right, represent the stiffness matrices of the ITM and ETM suspensions, as defined in Eq. 4.9. We assumed that the stiffness of the ITM suspension is equal to that of the ETM, as is the case in the experimental setup. Even in the case of two different suspensions, the equations of motion do not change, and Eq. 4.10 remains the same as long as we differentiate between the stiffness of the ITM suspension and that of the ETM. It is worth noting that the two suspension systems are independent in the sense that the motion of the ITM does not result in a torque on the suspension of the ETM. The effect of radiation pressure is to couple two otherwise independent suspensions. To account for this effect, we define the following stiffness matrix.

$$K_{\mathrm{OPT}} = \frac{2P_{\mathrm{ARM}}}{c} \frac{L}{1 - g_{\mathrm{ITM}}\, g_{\mathrm{ETM}}} \begin{bmatrix} 0 & 0 & 0 & 0 \\ 0 & g_{\mathrm{ITM}} & 0 & -1 \\ 0 & 0 & 0 & 0 \\ 0 & -1 & 0 & g_{\mathrm{ETM}} \end{bmatrix} \tag{4.11}$$

where P_{ARM} is the power circulating across an arm cavity, L the length of the cavity and, for each TM, g_{TM} depends upon the geometry of the cavity as:

$$g_{\mathrm{TM}} = 1 - L/R_{\mathrm{TM}} \tag{4.12}$$

Here, R_{TM} is the radius of curvature of the test mass. This matrix K_{OPT} has been calculated as in [62]. K_{OPT} is defined as a combination of two components: a prefactor that scales the radiation pressure force and a matrix that specifies the beam offset on the TMs according to their rotation.

This matrix is, in fact, plays the same role as the matrix D in Eq. 4.2. The effect of radiation pressure can be understood from a mechanical perspective. When the optics rotate, they displace the beam on the TMs. Consequently, a force exerted via radiation pressure, due to the beam being off-centred, results in a torque applied to the TMs. This couples the two suspension systems and the motion of one TM results in the application of torque to the other TM, causing it to move. The overall stiffness of the optomechanical system is determined by combining the purely mechanical stiffness with the optical stiffness due to radiation pressure as:

$$K = K_{\mathrm{M}} + K_{\mathrm{OPT}} \tag{4.13}$$

The frequency response of the system can be computed from Eq. 4.7. This is the plant of the system, which defines the motion of the mirrors (and the marionette) in response to an input torque.

ASC loops are designed on a base where the plant, or equivalently the optical stiffness matrix K_{OPT}, is diagonal. This is commonly known as the basis for the "hard and soft mode". For each arm cavity, this is expressed as follows:

$$\begin{bmatrix} \theta_{+} \\ \theta_{-} \end{bmatrix} = \begin{bmatrix} t_1 & t_2 \\ t_2 & -t_1 \end{bmatrix} \begin{bmatrix} \theta_{\mathrm{ITM}} \\ \theta_{\mathrm{ETM}} \end{bmatrix} \tag{4.14}$$

In this representation, each row of the change in basis matrix represents an eigenvector of the optical stiffness matrix. The $\theta_{\pm}$ DoFs are commonly known as the hard and soft modes, respectively. As explained in [62], when the

Table 4.1: Mechanical parameters of the suspension.

	Marionette	**Test mass**
Stiffness [Nm/rad]	0.07	18.7
Inertia [kg·m^2]	3.65	0.46

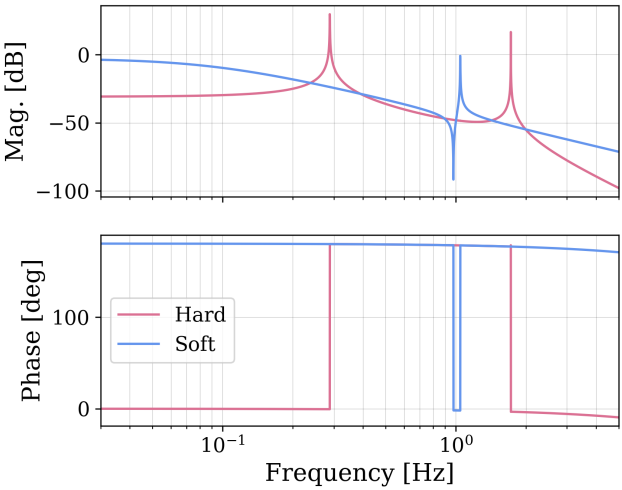

Figure 4.5: The torque to rotation transfer function of the opto-mechanical plant in the hard and soft mode base. For both curves, the torque is applied to the marionette, while the resulting motion is measured at different levels. For the hard mode, the output motion is read at the test mass level, whereas for the soft mode, it is measured at the marionette level.

mirrors move in the same direction, the beam tilts, resulting in a radiation pressure torque that tends to bring the optics back to their equilibrium position. This additional restoring effect strengthens the mechanical stiffness, which is why it is called the hard mode. Conversely, when the mirrors move in opposite directions, the beam shifts, and the resulting radiation pressure effect creates a torque that reinforces the displacement of the optics away from their equilibrium position. This additional anti-restoring effect softens the mechanical stiffness, which is why it is known as the soft mode. The optomechanical response of the plant is shown on the basis of hard and soft mode in Fig. 4.5. The mechanical parameters considered are listed on Tab. 4.1. Regarding the optomechanical parameters, the circulating power in the arms was considered to be 131.5 kW. For the geometry of each arm cavity, the parameters considered are those specified in the FINESSE model

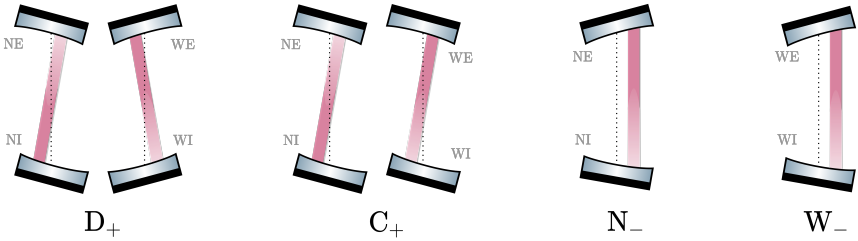

Figure 4.6: Illustration of DoFs under control. D_+ stands for Differential Plus, C_+ for Common Plus, N_- for North Minus and W_- for West Minus. Respectively, they include differential tilting of the beam between the arm cavities, common tilting of the beam between the arm cavities, shifting of the beam in the north arm cavity, and shifting of the beam in the west arm cavity.

of Virgo [63]. The model values for the lengths of the cavities and the RoC of each mirror were taken from experimental measurements. For both cavities, given the optomechanical values considered, t_1 and t_2 were found to be 0.76 and 0.64, respectively.

From a purely mechanical standpoint, the two arm cavities are identical and independent systems. Misalignment of a TM only displaces the beam within the cavity to which it belongs, thus defining the torque exerted by the radiation pressure on the TMs of that cavity. Despite this independence, the ASC loops use a set of DoFs that combines the modes of each arm cavity. Namely, the following DoFs were controlled for each axis of rotation:

$$\begin{bmatrix} D_+ \\ C_+ \\ N_- \\ W_- \end{bmatrix} = \begin{bmatrix} t_1 & t_2 & -t_1 & -t_2 \\ t_1 & t_2 & t_1 & t_2 \\ t_2 & -t_1 & 0 & 0 \\ 0 & 0 & t_2 & -t_1 \end{bmatrix} \begin{bmatrix} \theta_{\mathrm{NI}} \\ \theta_{\mathrm{NE}} \\ \theta_{\mathrm{WI}} \\ \theta_{\mathrm{WE}} \end{bmatrix} \tag{4.15}$$

The selection of these specific DoFs is motivated by optical considerations, where each produces a unique effect on the beam [64]; see Fig. 4.6

The detector requires accurate alignment of the optics in both the yaw (horizontal) and the pitch (vertical) axes. Our analysis focusses on yaw, sufficient to develop a reliable methodology for future detector modelling. Expanding this analysis to include pitch requires a slightly more elaborate mechanical description. Nevertheless, extending this modelling to pitch remains relatively straightforward.
Only the DoFs of the arm cavities have been considered, because their rotation directly influences the cavity length, thereby coupling directly with the detector output. This is not true for other optics, whose coupling with the output is indirect and is usually experimentally manageable. For instance, the rotation of the PRM, when there is beam misalignment, affects the length of the power recycling cavity, not that of the arms.

4.3 The control system

The control system defines the dynamics of the mirrors, the understanding of which is necessary to assess the amount of angular noise coupled to the detector output. In this section, we will illustrate the control system's architecture following the structure of the block diagram in Fig. 4.7.
The feedback controller $C \in \mathcal{R}^{4\times4}$, uses an error signal:

$$e = [e_{\mathrm{D}_+}\ e_{\mathrm{C}_+}\ e_{\mathrm{N}_-}\ e_{\mathrm{W}_-}]^T \tag{4.16}$$

to produce a control signal $u \in \mathbb{R}^4$ for each DoF. The driving matrix $T \in \mathbb{R}^{4\times4}$ applies a coordinate transformation to the actuation signal to obtain the actuation to the marionette of each mirror:

$$u_{\mathrm{mar}} = [u_{\mathrm{NI}}\ u_{\mathrm{NE}}\ u_{\mathrm{WI}}\ u_{\mathrm{WE}}]^T \tag{4.17}$$

The actuation to each marionette is converted into a torque by the matrix $A \in \mathcal{R}^{4\times4}$, which contains the dynamic of the actuators. The optomechanical plant P, which has been defined in the previous section, connects the torque

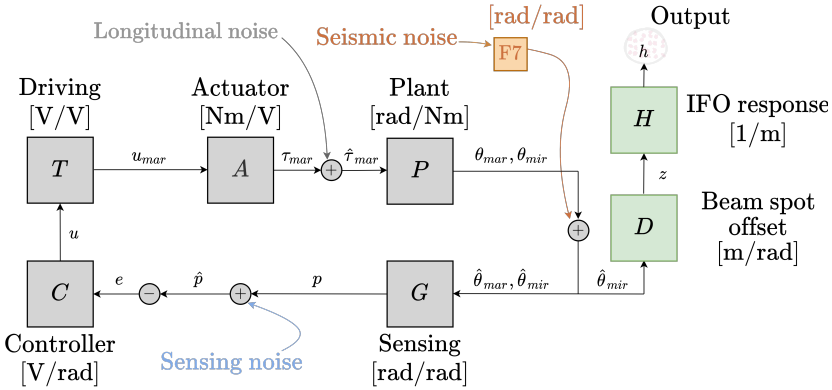

Figure 4.7: The grey blocks represent the block diagram of Advanced Virgo's ASC loops. The diagram shows the entry points of external disturbances into the loops, a description of which can be found in Section 4.4. The F7 block connects the residual motion of the suspension stage above the marionette, known as Filter 7, to a torque applied to the marionette. The green branch of the diagram illustrates how the mirror motion couples to the output of the detector; its elements are explained in detail in Section 4.5

applied to the marionette $\tau_{\text{mar}} \in \mathbb{R}^4$ to the rotation of the two suspension stages $\theta_{\text{mar}}, \theta_{\text{mir}} \in \mathbb{R}^4$, the marionette, and the mirror, respectively. The sensing matrix $G \in \mathbb{R}^{4\times4}$ connects the rotation of the optics and that of the marionette to the error signal of each DoF, which is denoted by:

$$p = [p_{\text{D+}}\ p_{\text{C+}}\ p_{\text{N-}}\ p_{\text{W-}}]^T \tag{4.18}$$

Considering the marionette movement is necessary because the O3 sensing scheme utilised optical levers reading at the marionette level to obtain $p_{\text{N\_}}$ and $p_{\text{W\_}}$. In the case of D_+ and C_+, QPDs were used as sensors. Specifically, Ward's technique [65] was employed for D_+, while for p_{C_+}, the beam's DC position on the dedicated photo detector was measured. A more detailed description of the angular sensing scheme used during O3 can be found

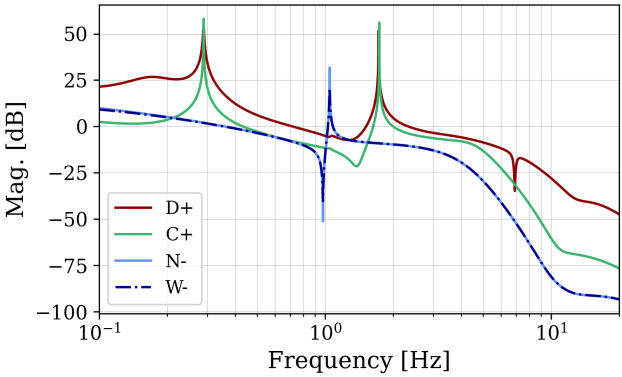

Figure 4.8: Magnitude of the open-loop transfer function of each loop.

in [66].

The magnitude of the Open Loop Transfer Function (OLTF) of each loop is shown in Fig. 4.8. For the specifications of the individual components of the loop, the sensing and driving matrices can be found in Tab. 4.2. The control filters used are the same as those used during O3.

Table 4.2: On the left and right side, the sensing and driving matrices are shown, respectively, in units [rad/rad]. The sensing matrix has been measured and imported into the FINESSE model. For the optical parameters of Advanced Virgo, the eigenvectors of the optical stiffness matrix are [0.76 0.64] and [0.64 −0.76]. It is quite evident that the sensing matrix is not composed of these vectors, making the system non-diagonal. The driving matrix has been experimentally tuned to improve the diagonalisation of the system and, in particular, to reduce the coupling in Fig. 4.11.

	NI	**NE**	**WI**	**WE**
D_+	-1.73	-2.13	1.95	2.14
C_+	5.37	6.12	-1.93	-2.16
N-	-1.00	1.00	0	0
W-	0	0	-1.00	1.00

	D_+	**C_+**	**N-**	**W-**
NI	0	0.50	-0.52	0
NE	0	0.50	0.48	0
WI	0.50	0.50	0	-0.54
WE	0.50	0.50	0	0.46

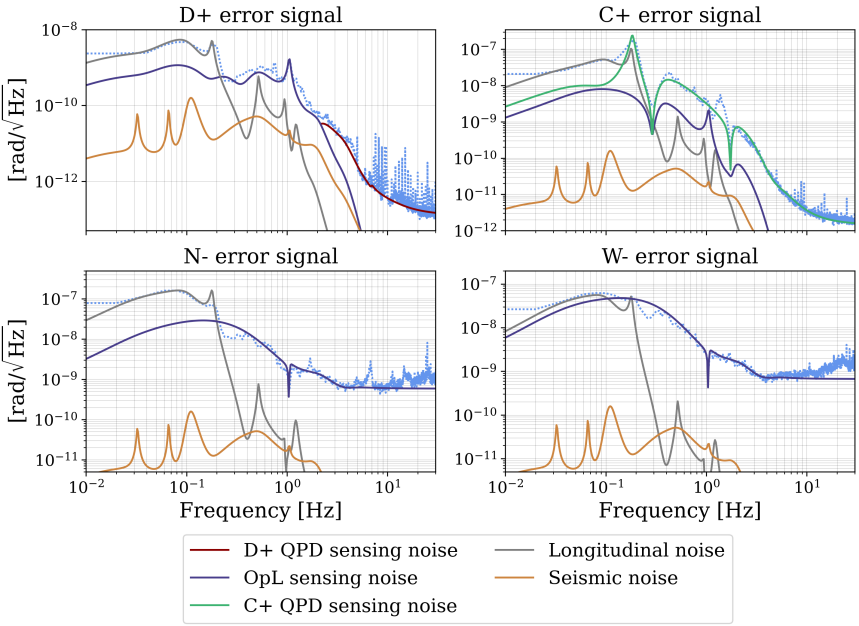

Figure 4.9: Noise budget of the ASC error signals. The contribution to each error signal was calculated using the FINESSE model, with the methodology explained at the beginning of the Section 4.4.

The ultimate modelling goal is to evaluate the effectiveness of the ASC system by quantifying the extent to which angular motion, within the detection frequency band ($f > 10$ Hz), contributes to the detector's output. To achieve this, the control scheme used during O3 has been integrated into a FINESSE model [33, 34]. In terms of optical setup, the model incorporates the current FINESSE model of the Virgo detector [63], readapted to the O3 configuration.

4.4 External disturbances

The last element missing to evaluate the residual movement of the optics is the external noise. From the analysis of experimental data, we have identified and characterised a series of external disturbances. These noises were then propagated through the modelled loops to calculate the residual movement of the optics. With this we mean that using FINESSE, the transfer function was calculated from the noise input point to the error signal point. This transfer function was then multiplied by the input noise to calculate the contribution to the error signal produced by that specific noise. In Fig. 4.7, we have marked the input point for each external noise source that we considered. Fig. 4.9 illustrates the resulting error signals for each input noise. In general, the output of the FINESSE model is a transfer function from any point in the diagram in Fig. 4.7 to any other point in the same diagram. Therefore, the just-outlined modelling methodology can be extended to calculate any signal of interest. This involves calculating the transfer function from the noise input point to the desired signal, and then multiplying this transfer function to the input noise.
A comparison between the transfer function calculated from the experimental data and that calculated through the model is shown in Fig. 4.11.

Fig. 4.9 shows that the input noises considered are adequate to reconstruct all error signals. Therefore, the set of noises serves as a comprehensive description of the system inputs.
It is important to note that certain disturbances that we have considered are influenced by environmental conditions. For our analysis, we selected a data set in which the environmental conditions led to a relatively large movement of the mirrors and, therefore, to a relatively large angle-to-length coupling. We aimed to confirm our model's precision under extreme working conditions and also helped in isolating and identifying the individual input contributions.

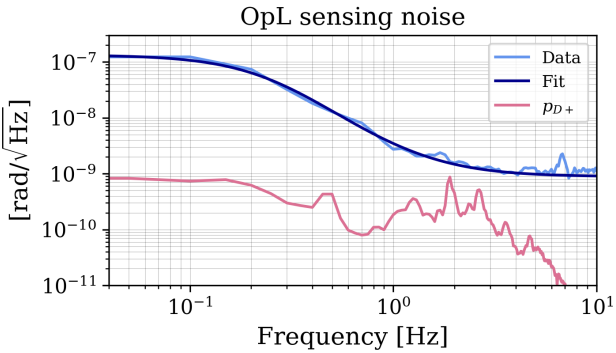

Figure 4.10: The red measurement indicates the D_+ error signal while the light blue measurement represents the same DoF measured using OpLs at the marionette level, and its corresponding fit is shown in dark blue.

Optical levers sensing noise

In Fig. 4.10, the red curve indicates the measurement of p_{D_+}, while the blue curve represents the motion of the same degree of freedom as measured by OpLs. Due to the sensor hitting its noise floor, the latter signal is higher than p_{D_+} throughout the frequency range. The dark blue curve in the plot corresponds to the measurement fit, representing the level of OpLs sensing noise that we have taken into account.

OpLs are used to control soft modes, specifically N_ and W_. The noise from these sensors is then re-introduced into the control loops, leading to motion in these modes. However, due to the nondiagonal nature of the system, this noise also induces motion in D_+, as shown in Fig. 4.9. The transfer function, shown in Fig. 4.11, is responsible for this coupling.

C_+ QPD sensing noise

In Fig. 4.9 is a measurement of the C_+ error signal. The presence of two pronounced troughs at the mechanical frequencies, around 300 mHz and

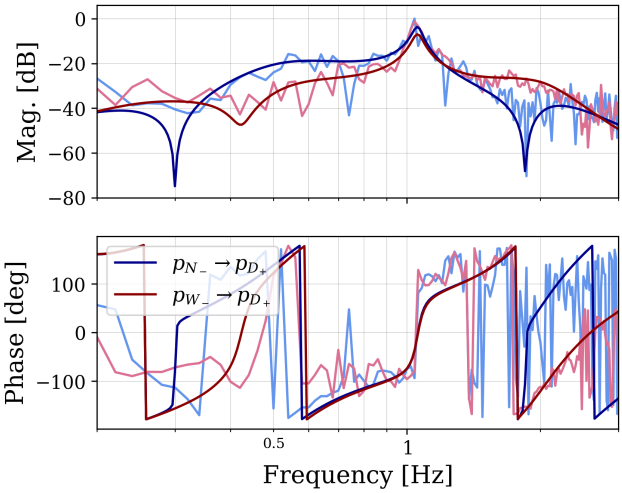

Figure 4.11: A direct comparison of the model's output, a transfer function, with its experimental counterpart. The figure shows the transfer functions that map the error signal of the soft modes to that of D_+ is shown below. The light-colored curve represents the measurement, while the dark-colored curve represents the model output.

2 Hz, respectively, suggests that this signal was dominated by the sensor noise. The feedback action of a loop suppresses a signal by a factor of one minus the open-loop gain. If the signal consists of noise and the loop gains at the mechanical frequencies, the result are these deep troughs in the sensor noise. Fig. 4.12 shows a measurement of p_{C_+} that has been divided by the loop suppression, resulting in an equivalent open loop measurement of noise. The structure at ~ 200 mHz in the p_{C_+} signal warrants a separate discussion. This was found to be coherent with the longitudinal motion of the lens that served as a placeholder for the signal recycling mirror. The movement of that lens resulted in jitters in the beam of the C_+ QPD, which ultimately produced the p_{C_+} signal. Although this is not strictly sensing noise, this signal is reinjected into the C_+ loop as much as the sensor noise. This is the

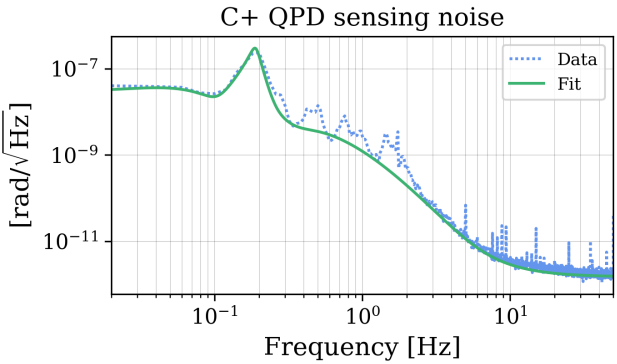

Figure 4.12: A measurement of p_{C_+} is shown along with its fit in green, after being multiplied by the inverse of the loop suppression.

reason we have included it as part of the C_+ QPD sensing noise.

D_+ QPD sensing noise

As shown in Fig. 4.9, the D_+ sensor detects movements resulting from various sources of noise up to ~ 2 Hz. The sensing noise of D_+ QPD has been regarded as anything beyond that frequency. Similarly to what was done for C_+ sensor noise, the measurement of p_{D_+} shown in Fig. 4.13 has been divided by loop suppression to remove the influence of the loop. The red curve represents the fit of the measurement for the frequency range of interest. This curve corresponds to the level of D_+ QPD sensing noise that we have considered.

Longitudinal noise

The actuators attached to the marionette were used as part of the length control system to correct for low-frequency disturbances. In the event that these actuators are imbalanced, the force applied for length control F_z will generate an additional torque on the marionette as:

$$\eta_z = \rho r F_z \tag{4.19}$$

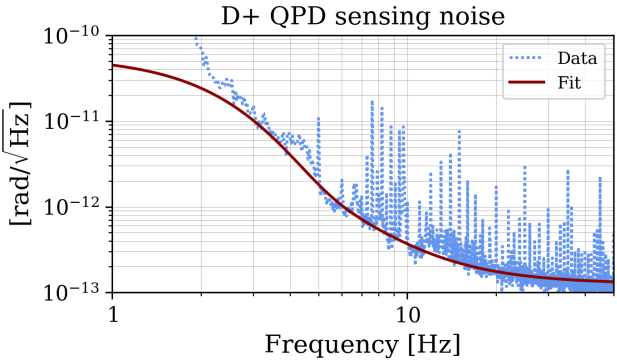

Figure 4.13: The measurement of p_{D_+} is displayed along with its fit in red, following the division by the loop suppression.

Here, r denotes the position of an actuator relative to the rotation axis, and ρ is a scaling factor that represents the degree of imbalance among all actuators attached to a marionette. The force applied to a marionette for length control is depicted in blue in Fig. 4.14, along with its fit in grey. In particular, coherence was observed between this signal and the angular error signals in the low-frequency range ($f < 200$ mHz), indicating that the rotation of the mirrors was driven by the length correction. The longitudinal noise has been defined as the signal in Fig. 4.14 multiplied by ρr. The result is a torque that has been applied to each marionette involved in the length control scheme. The level of imbalance of the actuators of each marionette

Table 4.3: The table records the measured level of imbalance of the actuators and their corresponding values from the model. The actuators are positioned at a distance of $r = 0.3$ m from the rotational axis. Notably, the length driving scheme utilizes only the actuators for the end test masses.

Imbalance ρ	**Model**	**Measured**
NE	0.21%	0.10%
WE	0.04%	0.03%

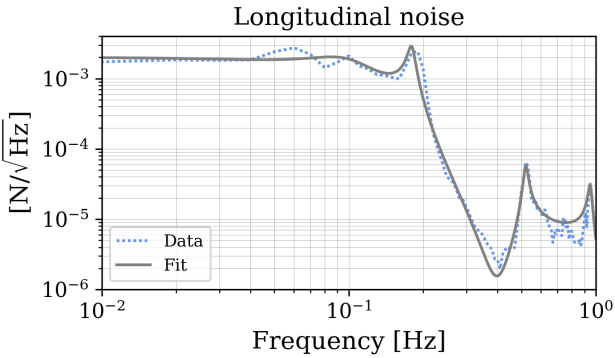

Figure 4.14: The measurement of the force exerted on the marionette for length control is depicted along with its fit in grey.

was adjusted to effectively replicate the error signals within the coherent frequency range using the model. As shown in Tab. 4.3, the degree of imbalance obtained from the model is in close agreement with the measured value.

Seismic noise

We considered the movement of the suspension point of the marionette as seismic noise, specifically the motion of Filter 7. This is the suspension stage positioned directly above the marionette. The motion of the ground is transmitted through the suspension, causing the movement of Filter 7. This, in turn, induces motion in the marionette, thereby entering the ASC loops. Fig. 4.15 illustrates the measurement obtained from a local sensor responsible for monitoring the motion of Filter 7. The signal captured by this sensor consists mainly of noise, except for three distinct structures occurring between 30 and 120 mHz. The curved segment of the signal, up to around 30 mHz, is a result of the sensor noise being "bent" by the influence of the local loop, rather than representing the actual motion of Filter 7. In more general terms, the local sensor does not measure for the most part the actual motion of Filter 7; instead, it captures mainly noise. The brown curve

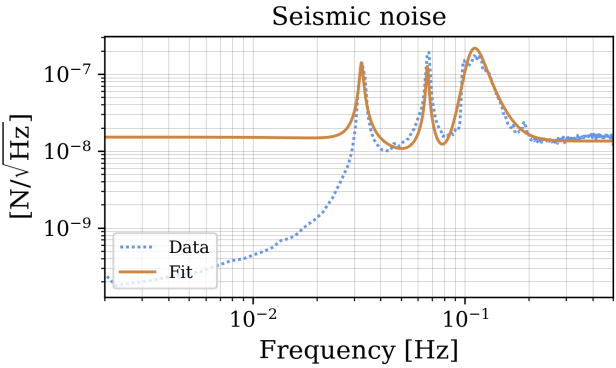

Figure 4.15: The measurement of a local sensor used to monitor the motion of Filter 7. The brown curve, labeled as "fit" for consistency with other plots, represents the level of seismic noise we have considered

represents the level of seismic noise that we have taken into consideration. It is calibrated based on the local sensor noise, which, as we have explained, exceeds the actual motion of Filter 7. Hence, this assessed noise level should be regarded as an upper limit.

The error signals in Fig. 4.9 capture the motion of the DoFs whenever it exceeds the sensor noise. Conversely, when the actual motion of the DoFs is lower than this noise, the error signals consist mainly of sensing noise shaped by the feedback action of the control loops. This noise is then reintroduced into the system, ultimately causing the mirrors to move. Using the model, the actual motion of the mirrors has been computed for the given noise sources, and the results are shown in Fig. 4.16. From the motion of the mirrors, we calculated the BSM on the TMs using Eq. 4.2; the result is shown in Fig. 4.17. This is the first time the measured BSM has been accurately reproduced using a numerical model of the optomechanical system.

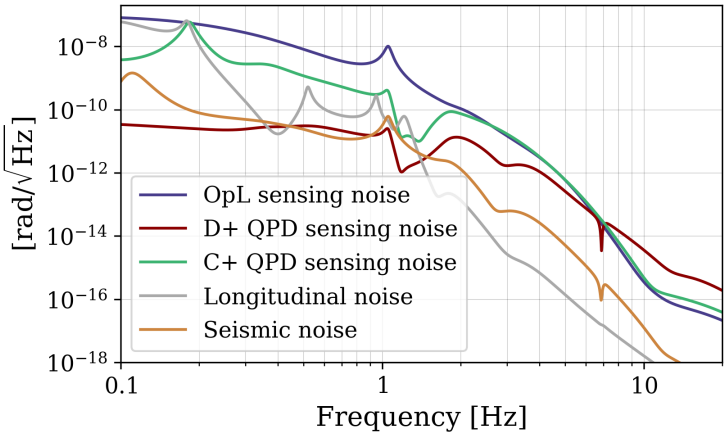

Figure 4.16: The figure shows the movement of one of the mirrors, specifically WI, caused by each input noise. Each contribution to the mirror motion was calculated using the FINESSE model, with the methodology explained at the beginning of Section 4.4.

4.5 Noise projections: the methodology

In Fig. 4.7, the green branch of the diagram is the chain that carries the motion of the mirrors to the detector output channel. The matrix $d \in \mathbb{R}^{4\times4}$ serves to convert the mirror rotations θ_{mir} into the corresponding length changes, resulting in a length vector $z \in \mathbb{R}^4$. This matrix D is diagonal and consists of scalar coefficients along the diagonal, as shown below.

$$D = \text{diag}(d_{\text{NI}}\ d_{\text{NE}}\ d_{\text{WI}}\ d_{\text{WE}}) \tag{4.20}$$

These coefficients are responsible for translating the rotation of specific optics into length changes. Specifically, when applying the matrix D to the vector θ_{mir}, the result is the vector z, where each element corresponds to a change in the length of the arm cavities due to rotation of each TM:

$$z = [z_{\text{NI}}\ z_{\text{NE}}\ z_{\text{WI}}\ z_{\text{WE}}]^T \tag{4.21}$$

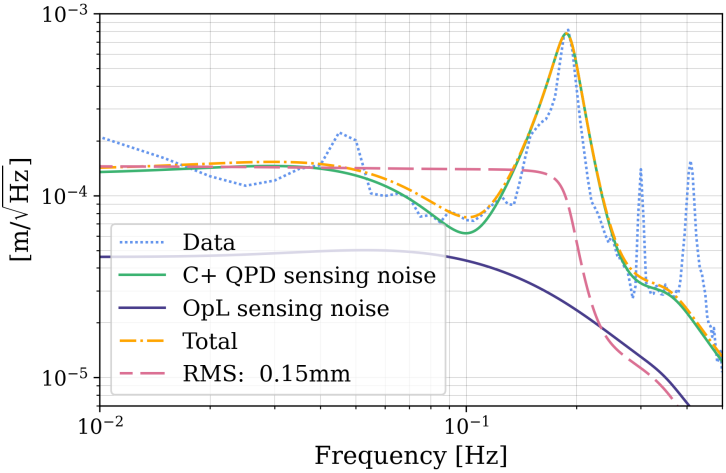

Figure 4.17: Noise budget of the beam spot motion. The yellow curve represents the sum of all contributions from the input noise. The dashed red line illustrates the cumulative RMS of the yellow trace, which corresponds to approximately 0.15 mm. The measured RMS from the experimental data is around 0.14 mm. Each contribution to the BSM was calculated using the FINESSE model, with the methodology explained in Section 4.4.

For instance, z_{NI} represents the modification in the northern cavity's length caused by the rotation of the NI optic. Each element in vector z results from a product of this form:

$$z_{\text{TM}} = d_{\text{TM}}\,\theta_{\text{TM}} \tag{4.22}$$

This relationship resembles the one defined in Eq. 4.1, where the outcome indeed represents a change in length. While θ_{TM} encompasses the entire spectrum of NI movement, d_{TM} has been approximated as a scalar constant, which we call static offset; the same has been done for all other TMs. As explained in [56], while an accurate representation of this process involves the convolution of the BSM spectrum with the angular motion spectrum, the

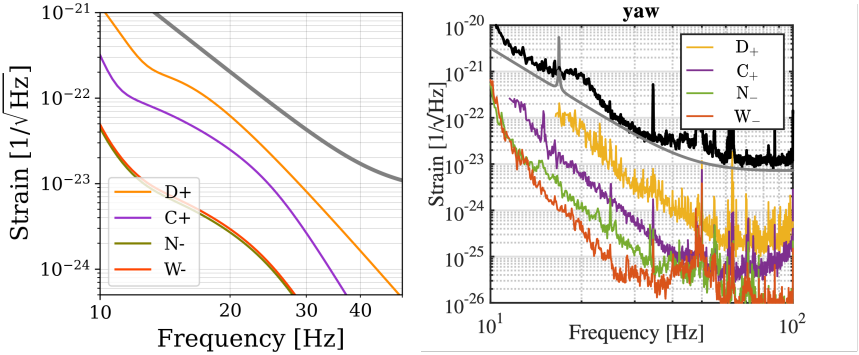

Figure 4.18: On the left, the figure displays the level of angular control noise calculated through the model. The plot shows the noise produced by each of the degrees of freedom. The methodology with which these noise projections were obtained is described in Section 4.5. On the right, the measured noise levels are shown; this figure has been adapted with permission from [59]. The grey line in both graphs represents the target sensitivity for the O3 run.

predominance of low-frequency components in the BSM allows us to treat the misalignment as if it were static. The static offset value can be calculated as the RMS of the BSM. The way in which the detector responds to the length variations defined in z is defined by $H \in \mathcal{R}^4$, which represents the detector response to a differential change in the lengths of the arm cavities. The dot product between the vectors H and z is the signal produced in the output channel of the detector h, which has been calculated using FINESSE.

The amount of angular control noise calculated through the model is shown in Fig. 4.18 in terms of the detector sensitivity. In terms of the methodology used to generate these noise projections with FINESSE, the process comprises two fundamental steps. First, external disturbances are propagated through the model to calculate the motion of the test masses and subsequently determine the beam spot motion, as shown in Fig. 4.17. The

RMS of the BSM is then used as the static offset, which in our case has been determined to be $d_{\mathrm{RMS}} = 0.15$ mm. Next, this beam offset is applied to all the TMs, and the external disturbances are propagated again through the model to calculate the differential change in the length of the detector's arms. In particular, during this second step, only the sensor noise has been propagated because it is the dominant noise in the detection frequency band ($f > 10$ Hz), which is now our focus; see Fig. 4.9. Each trace in Fig. 4.18 refers to a specific degree of freedom. This projection was obtained by propagating the sensor noise used to control that particular DoF. For example, the C_+ curve was obtained by propagating the C_+ QPD sensing noise. The last point to consider is how the static offset has been allocated to each TM. The proposed noise projection methodology takes into account the coherence between the movements of all mirrors. For example, when the C_+ QPD sensing noise is propagated, the TMs rotate simultaneously in phase. This results in a noise projection depending on the arrangement of the static offset on each TM. For example, if the beam spot is offset in such a way that the beams in both cavities are shifted, the in-phase motion of the TMs does not change the cavity length and, therefore, does not lead to the generation of angular noise. The static offset has been distributed among the TMs to maximise the coupling of each DoF to the detector's output. Each curve in Fig. 4.18 corresponds to a different distribution of the direction of the static offset. For example, in the case of the C_+ curve, the matrix D was defined as:

$$D_{\mathrm{C}+} = \mathrm{diag}(-d_{\mathrm{RMS}} \;\; +d_{\mathrm{RMS}} \;\; +d_{\mathrm{RMS}} \;\; -d_{\mathrm{RMS}})$$

Table 4.4: Arrangement of the static offset on each TM for the projection of each DoF.

	NI	**NE**	**WI**	**WE**
$\mathbf{D}_+$	$-d_{\mathrm{RMS}}$	$+d_{\mathrm{RMS}}$	$-d_{\mathrm{RMS}}$	$+d_{\mathrm{RMS}}$
$\mathbf{C}_+$	$-d_{\mathrm{RMS}}$	$+d_{\mathrm{RMS}}$	$+d_{\mathrm{RMS}}$	$-d_{\mathrm{RMS}}$
$\mathbf{N}_-$	$+d_{\mathrm{RMS}}$	$+d_{\mathrm{RMS}}$	0	0
$\mathbf{W}_-$	0	0	$+d_{\mathrm{RMS}}$	$+d_{\mathrm{RMS}}$

More generally, the distribution of the static offset for the projection of each degree of freedom is shown in Tab. 4.4.

The noise projections generated by the model confirm that Advanced Virgo was not constrained by angular control noise during O3. This is in agreement with the experimental measurement of noise levels, which is shown in Fig. 4.18. To compare the two projections, it should be noted that the two plots reflect different environmental conditions. For our analysis, external disturbances refer to environmental conditions that led to a relatively significant angle-to-length coupling, specifically 0.15 mm, which was used to generate the plot on the left. The data in the plot on the right were collected at a different time, which is not specified by the plot's author. Depending on environmental conditions, the coupling factor was found to reach a minimum value of 0.05 mm, while on average it settled around 0.10 mm. This implies that the level of each curve in the model projections can be lower by as much as a factor of three, making the projection levels compatible with those measured experimentally. In addition, what is important to note is that the sequence of contributions per DoF is consistent with that measured experimentally. D_+ is the largest contributor, followed by C_+ and finally the soft modes.

Overall, this indicates that the methodology developed for evaluating the residual rotation of the TMs and its subsequent impact on the detector's output is successful. This establishes a robust foundation for modelling future detector configurations, as well as future-generation detectors.

The noise projection scheme was repeated for the case where Virgo would be operated at full power. The result is shown in Fig. 4.1, indicating that Virgo would not be limited by angular noise even in this scenario. To produce this projection, the input noise and the control system architecture were left unchanged. The key change resulting from the power increase was the impact of the radiation pressure on the mechanical components. The control filters were adapted to the new plant, but they were still designed to ensure

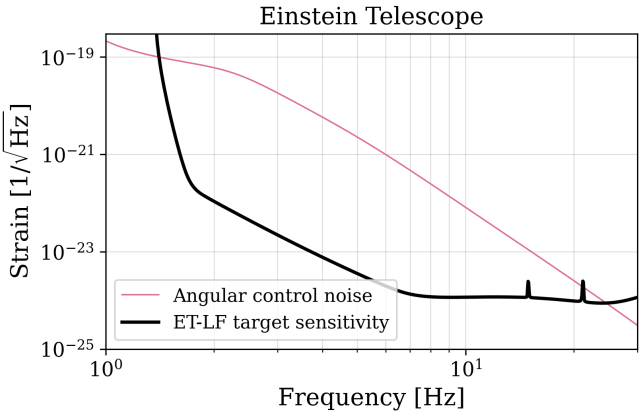

Figure 4.19: Projection of angular noise on the low-frequency sensitivity of ET.

a match with the requirements for the residual motion of the TMs.

4.6 Conclusions for Virgo and implications for ET

In this study, we have successfully developed a model of the Advanced Virgo angular control system, confirming that it has not been limited by angular control noise, despite facing external disturbances comparable to those of aLIGO. The construction of the model has led to a thorough characterisation of the angular control system, which has shown that to model the angular control noise accurately, a comprehensive understanding of the various external disturbances is essential. Furthermore, using the developed and validated model, we have shown that Virgo would not be limited by angular control noise even when operated at full power. More generally, the remarkable agreement between our ACS model and experimental data represents a significant milestone, providing a solid foundation for modelling the low-frequency design of future-generation detectors.

We are now in a position to extend the application of the ASC model to

the Einstein Telescope case, allowing us to evaluate the detector noise performance using an accurate and well-validated model. Fig. 4.19 illustrates a prediction of the angular noise level in ET. It is evident that this noise has the potential to pose a significant challenge to ET. However, it is essential to emphasise that the true result here is the ability to track the noise level, and the projection itself is likely an exaggerated estimate.

This projection was obtained by directly applying the AdV angular control system without any modifications to Einstein Telescope, including external noise. Specifically, we applied the same control architecture described in Section 4.3 to the optical layout of ET-LF, as implemented in the corresponding FINESSE model [67]. The main difference compared to the Virgo case lies in the suspension system's mechanics. We created a preliminary model of the mechanics based on some initial ideas emerging in the community, all inspired by the Virgo superattenuator; more details will be provided in the upcoming paragraph.

Finally, we come to the two key elements that require more careful understanding for the purpose of producing a reliable noise projection: control filters and external noises. Regarding the control filters, we employed those from AdV and adapted them to the new system. Since the requirements for the residual rotation of the TMs have not yet been defined for ET yet, these filters have been designed to roughly match the requirements for Virgo. However, weel-defined requirements for ET are essential to determine the loops gain. Without these requirements, the design of the control filters becomes somewhat arbitrary. In simple terms, for the same input noise, a system that requires more extensive control will generate a higher amount of control noise. An example of this effect can be observed in Fig. 4.8, where we compare the OLTF of D_+ with that of C_+. Both modes are hard modes and, therefore, share the same plant. As explained in the previous Section 4.2, from a purely mechanical perspective, the arm cavities are identical systems, each with its hard and soft modes. If the TMs in each cavity move in a D_+ or C_+ manner, there is no mechanical distinction between them. As a result, it might be logical to assume that the same controller could be employed for both DoFs, and thus, the OLTF should be identical. However, this is

clearly not the situation. As explained in Section 4.2, while the common or differential motion of TMs may be identical from a mechanical point of view, this is not true from an optical point of view. The motion of D_+ defines the differential tilt between the arm cavities, affecting the quality of the dark fringe in the output port. Simply put, the less D_+ moves, the better the quality of the dark fringe. Consequently, the control loop for this specific DoF requires a higher gain over a wider frequency range, resulting in a different filter design. This filter starts to roll off later and with a gentler slope compared to the filter for C_+. As a result, D_+ becomes the main source of injected angular control noise at the detector output; you can see this in Fig. 4.18. This happens despite the fact that D_+ has a high-frequency detection noise almost an order of magnitude lower than that of C_+.

The other fundamental element that requires discussion is input noise. The noises considered are the same as those discussed in Section 4.3, and for all these noises, there is certainly room for improvement. The only difference is that to produce Fig. 4.18, the projections of soft modes were ignored. This was done to avoid giving rise to a possible misconception that ET might be limited by angular noise solely because of the use of optical levers. The projection is instead obtained by projecting only the sensing noise of the QPDs.

The high-frequency sensing noise, which is the source of noise injected into the detector's output. With respect to low-frequency disturbances that ultimately determine the BSM, the focus is returned to requirements for the residual motion of the TMs. In the case of AdV, we have shown that sensing noise is the main contributor to TM motion even at low frequencies; see Fig. 4.16. If we consider the scenario for ET in which we use more effective OpLs or none at all and avoid errors in choosing where to collect error signals that would result in structures similar to the 200 mHz feature in C_+ QPD sensing noise, then the primary source of noise is the longitudinal noise. To obtain a realistic estimate of this noise and, consequently, the BSM, an estimate of the expected longitudinal correction is necessary. In this case as well, the correction depends on the requirements for the residual longitudinal motion of the TMs, which are currently undefined for ET.

Our modelling for AdV has revealed the intricacies of the system. Given the significant improvements expected for ET at low frequencies, all of these details cannot be overlooked when designing ET at low frequencies. Once the outlined requirements are established, the noise projection for ET will need to be reviewed. If ET were to be limited by angular control noise, even in the case of sensors limited by shot noise, this might necessitate a reevaluation of the mechanics. For example, adding a suspension stage between the marionette and the mirror would provide an additional level of passive attenuation, which, with careful design considerations, could potentially address the issue.

A brief overview of ET mechanics

We conclude by providing details about the mechanics used for ET. It should be noted that a suspension design for ET does not yet exist, although some initial ideas are based on the Virgo superattenuator. Specifically, we have roughly adapted some key parameters from the Virgo suspension to the case of an ET's TM. All the mechanical details considered are shown on Tab. 4.5. Starting with the mass, thickness, and radius of the TM, its moment of inertia was defined using the formula for a solid cylinder:

$$I_{\mathrm{mir}} = \frac{m\,(3r^2 + h^2)}{12} \tag{4.23}$$

The TM is attached to the marionette by four suspension wires. The tension in a single wire can be calculated as:

$$T_{\mathrm{w}} = \frac{m\,g}{4} \tag{4.24}$$

The factor of 4 takes into account that the tension is distributed among four wires. At this point, the stiffness of the final stage of the suspension, defined

by the overall stiffness of the four wires, was calculated as follows:

$$k_{\text{mir}} = \frac{mr^2}{l} \tag{4.25}$$

where l is the length of a wire.
As for the marionette, its moment of inertia, we have simply maintained the same marionette-to-mirror proportions as in the Virgo suspension, where the marionette's moment of inertia is approximately four times that of the mirror. Concerning its stiffness, this was manually adjusted to have the resonance frequency of the puppet stage around 20 mHz, as in the case of Virgo. Regarding the effects of radiation pressure, they are included by default in FINESSE simulations, which, given the optical parameters in the model for ET-LF, modify the mechanics accordingly without necessarily having to go through Eqs. 4.7 and 4.13.

Table 4.5: Parameters of the mechanics we have considered for ET. The parameters for the TM are based on [7].

Parameter	Value
TM mass m	211 kg
TM radius r	0.225 m
TM thickness h	0.57 m
Wire length l	0.9 m
TM stage inertia I_{mir}	8.4 kg·m^2
TM stage stiffness k_{mir}	116 Nm/rad
Marionette stage inertia I_{mar}	33.5 kg·m^2
Marionette stage stiffness k_{mar}	0.53 Nm/rad

5

Simulations in support of commissioning

Our round-trip journey has come to an end. This chapter is a bit like the post-credit scene at the end of a movie. It is not part of the main narrative, but at the same time, it cannot be understood without knowing the story that just concluded.

Here, we present a selection of some of the investigations that we initiated during my time at the Virgo site from February 2021 to October 2021. Many of these continued even after leaving the site, such as the study of offsets in the error signals discussed in Section 3.5. The specifics and technicalities of these tasks supporting the commissioning activities are documented in technical documents. We mention some here to make them easier to refer to [13, 68, 69, 70, 71, 72].

The main focus of this chapter is a set of simulations in support of the design of the lock acquisition of the Central part of the InTerFerometer

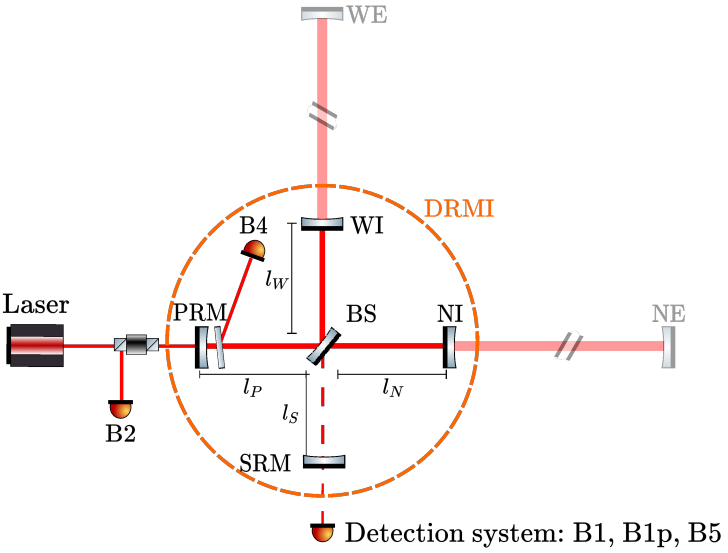

Figure 5.1: The figure illustrates the simplified optical layout of AdV+, highlighting its central part inside the orange circle. This is a Dual-Recycled Michelson Interferometer (DRMI). Its optics consist of the input mirrors of the Fabry-Pérot cavities, as well as the power recycling and signal recycling mirror. The figure also indicates the positions of the main photodetectors that monitor the DRMI beams. These photodetectors are labeled as follows: B2 (reflection from the PRC), B4 (intra-cavity pickoff of PRC), B1p (antisymmetric port pickoff), B1 (antisymmetric port beam after the output mode cleaner), and B5 (stray-beam generated by the BS anti-reflective surface). The figure is adapted from [15].

(CITF). With *lock acquisition*, we refer to the process of bringing the system to its desired operational state. For details of the process, we recommend consulting [15]. As in Section 3.5, given the specific context in which these simulations are placed, we assume that the reader has basic knowledge of the detector and its operation.

The interferometer is a complex system with multiple degrees of freedom.

Bringing it to its final operating conditions is an equally complex process that does not happen in a single step, but requires a series of stages. Acquiring control over the DoFs of the CITF is one of these stages. The placement of this step within the overall procedure is detailed in [55], where the entire process is thoroughly outlined.

We begin with Section 5.1, where we provide a bit more context and describe the central part of the detector. We then proceed to Section 5.1.1, which presents the trigger signal strategy that we helped design. These signals essentially indicate that the system is transitioning near the desired operational point. We conclude with Section 5.1.2, where we show the scheme used to expand the linear region of the error signal used for PRCL control.

5.1 The DRMI: system description

The central part of the interferometer is highlighted in Fig. 5.1 and consists of a Dual-Recycled Michelson Interferometer (DRMI). The DoFs associated with this system that we want to control are:

$$\begin{aligned} \text{MICH} &= l_N - l_W \\ \text{PRCL} &= l_P + \frac{l_N + l_W}{2} \\ \text{SRCL} &= l_S + \frac{l_N + l_W}{2} \end{aligned} \tag{5.1}$$

As for the arm cavities, during the locking of the CITF, they are locked to an auxiliary laser with a tunable frequency [73]. This configuration permits setting the arms out of resonance relative to the main laser, facilitating the separate lock acquisition of the CITF from the arms. After the lock acquisition of the CITF is achieved, the arms are realigned to the resonance condition with the carrier.
The sensing scheme for the DoFs of the CITF utilises modulation-demodulation

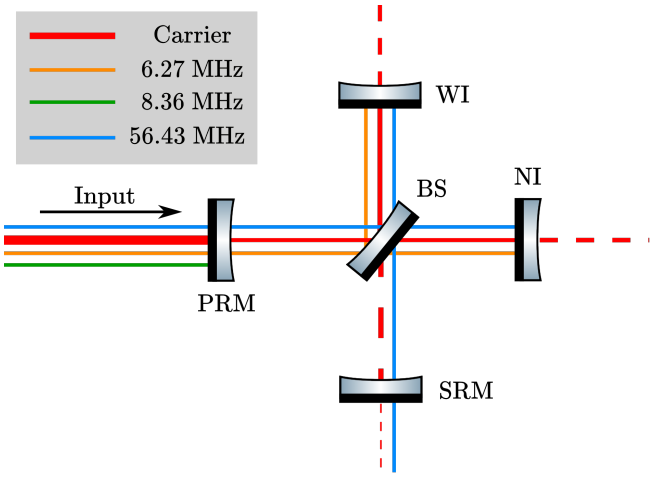

Figure 5.2: The illustration depicts the resonance conditions of the control sidebands in the DRMI at the operating point. In the case of the PRC, resonance occurs for both the 6 MHz and 56 MHz sidebands, while the carrier experiences anti-resonance. Conversely, the SRC resonates with both the 56 MHz sideband and the carrier. Lastly, the Michelson interferometer is in the the dark fringe state. The figure is adapted from [15].

techniques derived from the PDH scheme. The input laser beam is phase modulated at three different frequencies (6.27 MHz, 56.43 MHz, and 8.36 MHz). The modulation frequencies are carefully selected to ensure that the control sidebands meet specific resonance conditions within the PRC and SRC, which are illustrated in Fig. 5.2. The photodetector where each error signal is collected and the corresponding modulation-demodulation frequencies are detailed in Tab. 5.1 for each DoF.

In this section, we will discuss the *operating point* of the CITF system and the operational conditions anticipated once its lock has been acquired, as illustrated in Fig. 5.2.

5.1.1 Trigger scheme for the lock acquisition of the CITF

As an example to illustrate a more complex concept, the 56 MHz sidebands resonate in both recycling cavities at the operating point. Therefore, the resonance conditions of these sidebands depend on both the length of the SRC and the PRC. In general, this interplay between the PRC and the SRC makes it impossible to gain control of each DoF one after the other. Instead, we have to acquire control over all the DoFs at once. This method is often called *coincidence locking*. Thus, it is crucial to determine when all three DoFs approach the operating point so that control loops can be engaged. To achieve this, we identified a set of trigger signals. These signals act as indicators of the transition of the system near its operating point and "light up" when the system is in close proximity. The system is close enough to

Table 5.1: Readout scheme per DoF. It is shown the Detector from which the error signal is extracted for each DoF, along with the demodulation Frequency and demodulation Quadrature.

	PRCL	**MICH**	**SRCL**
Detector	B2	B2	B2
Frequency [MHz]	6	56	56
Quadrature	I	I	Q

Table 5.2: Trigger scheme for CITF lock acquisition. The demodulation Frequency is provided, unless it is a DC signal monitoring the average power on the detector. The Threshold value is expressed as a percentage relative to the maximum signal value. Positive Logic refers to a condition where the signal value needs to be above the threshold to enable the engagement of control loops. Conversely, negative Logic implies the opposite condition.

	Trigger 1	**Trigger 2**	**Trigger 3**	**Trigger 4**
Detector	B4	B4	B4	B1p
Frequency [MHz]	12	112	DC	DC
Logic	Positive	Positive	Negative	Negative
Threshold	70%	60%	10%	10%

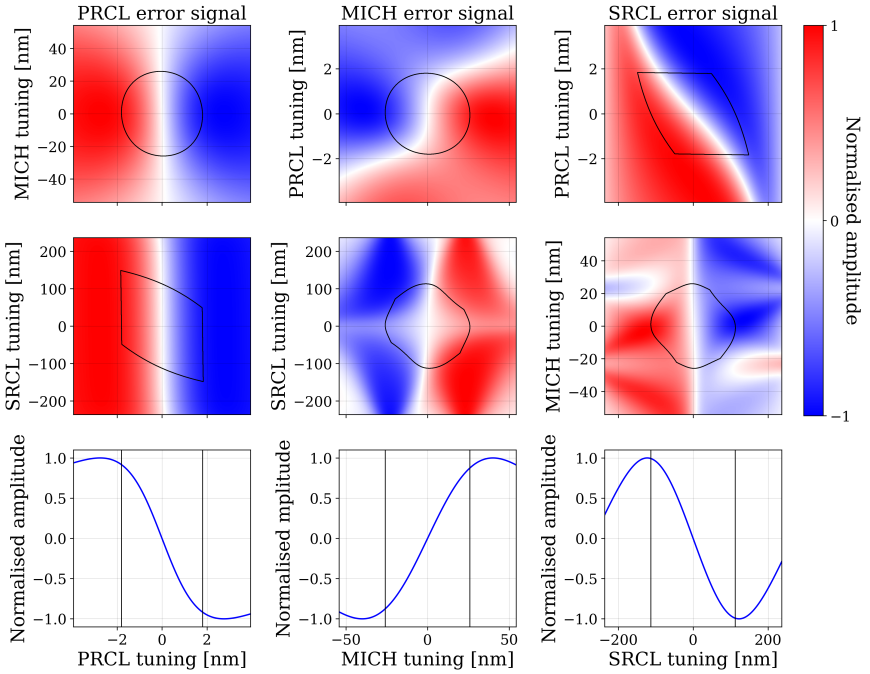

Figure 5.3: In the top two rows, the error signals are plotted against the tuning of pairs of DoFs. The operating point is located in the centre of each image. Points within the black line exceed the triggering thresholds. For clarity, the last line shows the error signal used for each DoF relative to the tuning of that same DoF. This helps visualise that the chosen trigger logic is satisfied when the system is near the linear region of the error signals. The figure is adapted from [15].

the operating point to be able to close the control loops if it lies within the linear region of the error signals. This is because a linear controller requires the system to be within the linear region of the error signal to be engaged.

The selected trigger scheme used for lock acquisition is presented in Tab. 5.2, designed to monitor the operational conditions illustrated in Fig. 5.2.

This scheme incorporates four signals. The first two triggers are “2f signals”, obtained by demodulating at twice the demodulation frequency. In Eq. 2.58, we showed that these types of signals are proportional to the power of the control sidebands. Although this was demonstrated for a strongly coupled cavity, this result also holds for simpler setups, such as the PDH, and those similar to the PDH, such as the one currently under analysis. Requiring the first two triggers to exceed specific thresholds ensures the desired resonance conditions of the sidebands within the recycling cavities. As for trigger 1, it is used to infer the resonance of the 6 MHz sidebands in the PRC, while trigger 2 serves as an indicator of the resonance of the 56 MHz sidebands in both the PRC and the SRC. The remaining two triggers guarantee that the carrier is antiresonant within the PRC (trigger 3) and that the Michelson interferometer operates under dark fringe conditions (trigger 4). The threshold values have been determined on the basis of two criteria: ensuring that the system lies within the linear region of the error signals and achieving the highest rate of successful lock acquisitions. Evaluation of the first criterion was performed using FINESSE, and the results are presented in Fig. 5.3. It can be seen that for the selected values, the system resides within the linear region of the error signals. The second criterion was studied through time domain simulations, and the corresponding results are reported in [15].

5.1.2 Linearisation of PRCL error signal

The criterion we studied when defining the thresholds for the trigger signals is solely position-dependent: when the system is near the operational point, the loops must be closed. However, this criterion may sometimes not be sufficient to ensure successful lock acquisition. For example, if the system enters the linear region too quickly, it requires rapid deceleration, potentially exceeding the actuation limits. In other words, the velocity of the system may exceed the threshold velocity for the associated linear controller, thus causing the lock acquisition to fail [28]. This turned out to be the case for PRCL; despite the loop being engaged in the right position, it was not enough to maintain control over the DoF, resulting in a failed lock acquisition.

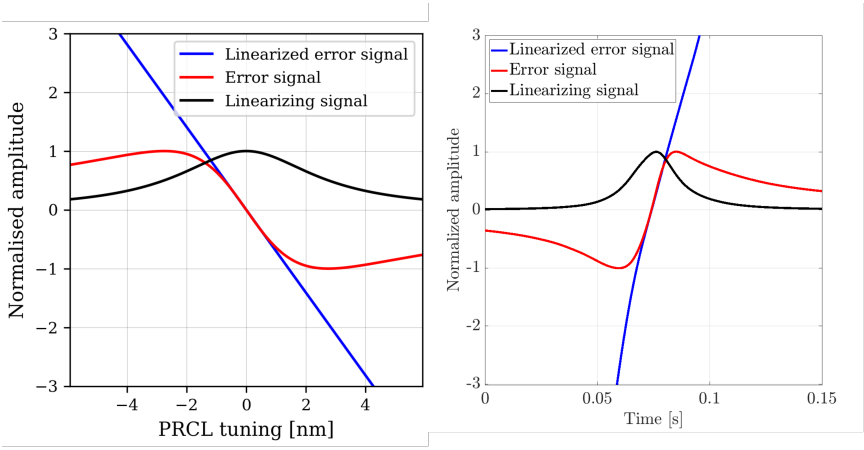

Figure 5.4: Simulated expansion of the linear region of the PRCL error signal is shown on the left, accompanied by its experimental implementation on the right-hand side. In both figures, the standard error signal is represented in red, while the corresponding 2f signal, used as a linearising signal, is depicted in black. The blue line represents the linearised error signal obtained by dividing the error signal by the linearising signal. The figure is adapted from [15].

As described in Section 2.8, the linear region of a PDH-like error signal is fairly narrow and is of the order of the linewidth of the cavity to which it refers. Near the operational point, this type of signal is inversely proportional to the cavity linewidth. The PRC, being a high-finesse cavity, results in a narrow linear region for the error signal, thus limiting the window for system deceleration. A narrower linear region corresponds to a lower threshold velocity for a linear controller. Expanding the linear region of the error signal is one approach to increasing the threshold velocity of a linear controller.

In a simple PDH setup, the linear region of the PDH signal expands when the error signal is divided by the power transmitted by the cavity [28]. The mode profile of the transmitted power is given by the Airy distribution [30].

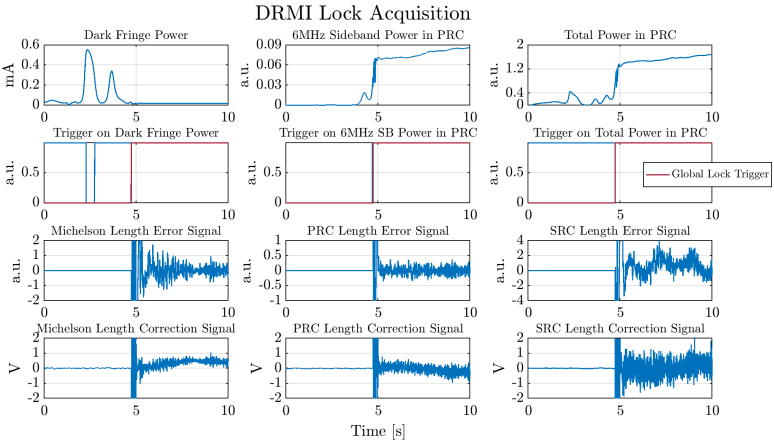

Figure 5.5: Example of a successful CITF lock acquisition. The first row shows three example trigger signals: trigger 4, trigger 1, and trigger 3, respectively. The second row represents a "Bayesian switch" that outputs 0 when the signal in the same column is below the threshold and 1 when it exceeds it. The red global trigger combines the required conditions on all trigger signals. It transitions from 0 to 1 when all signals surpass their threshold values, enabling loop engagement. The figure is adapted from [15].

Generally, any signal that has the same profile can be used to expand the linear region of the error signal. The 2f signal, obtained by demodulating at double the frequency, is proportional to the power of the control sidebands. Its profile, defined by the Airy distribution, makes it a suitable linearising signal for the error signal. This was shown in Eq. 2.58 for a strongly coupled cavity, and the same holds for simpler setups, such as PDH, and similar cases, such as the PRCL error signal. To expand its linear region, we have proposed a linearisation that involves dividing the PRCL error signal by a type 2f signal, obtained by demodulating the B4 signal at 12 MHz. Fig.5.4 shows the expansion of the linear region of the PRCL error signal, along with

its experimental implementation. This enhancement markedly improved the success rate of lock acquisition.

5.2 Summary

This chapter provides a snapshot of the selected simulations performed in support of commissioning. A more comprehensive list of technical documents that gather the finer technical details of the various simulations carried out was presented at the beginning of the chapter. The list was compiled to show the most updated document for each of the areas of interest that we have covered.
The work presented here focusses on a set of simulations all related to the lock acquisition of the CITF, to which we contributed by supporting the design of a trigger signal logic and proposing a scheme to expand the linear region of PRCL error signal. The linearisation strategy, once experimentally implemented, has significantly increased the rate of successful lock acquisitions.

The foundation of success in achieving control of the CITF lies in meticulous modelling work, which is the result of numerous joint efforts, all collected in [15]. Fig. 5.5 shows an example of successful acquisition of CITF locks, using the trigger scheme and the linearisation of the PRCL error signal described in this section.

References

[1] B. P. Abbott et al. 'Observation of Gravitational Waves from a Binary Black Hole Merger'. In: *Phys. Rev. Lett.* 116 (6 2016), p. 061102.

[2] The LIGO Scientific Collaboration et al. 'Advanced LIGO'. In: *Classical and Quantum Gravity* 32.7 (2015), p. 074001.

[3] B. P. Abbott et al. 'Tests of General Relativity with GW150914'. In: *Phys. Rev. Lett.* 116 (22 2016), p. 221101.

[4] B. P. Abbott et al. 'LIGO: the Laser Interferometer Gravitational-Wave Observatory'. In: *Reports on Progress in Physics* 72.7 (2009), p. 076901.

[5] F. Acernese et al. 'Status of Virgo'. In: *Classical and Quantum Gravity* 25.11 (2008), p. 114045.

[6] F. Acernese et al. 'Advanced Virgo: a second-generation interferometric gravitational wave detector'. In: *Classical and Quantum Gravity* 32.2 (2014), p. 024001.

[7] 'ET design report update 2020'. In: ET-0007B-20 (2020).

[8] M. Maggiore. *Gravitational Waves: Volume 1: Theory and Experiments*. Oxford University Press, Oct. 2007.

[9] C. Bond, D. Brown, A. Freise, K. A. Strain. 'Interferometer techniques for gravitational-wave detection'. In: *Living Reviews in Relativity* 19.1 (2017), p. 3.

[10] J. Mizuno, K. Strain, P. Nelson, J. Chen, R. Schilling, et al. 'Resonant sideband extraction: a new configuration for interferometric gravitational wave detectors'. In: *Physics Letters A* 175.5 (1993), pp. 273–276.

[11] P. Jones, T. Zhang, H. Miao, A. Freise. 'Implications of the quantum noise target for the Einstein Telescope infrastructure design'. In: *Phys. Rev. D* 101 (8 2020), p. 082002.

[12] R. Maggiore, A. Freise, A. Dmitriev, M. Sallé. 'Tuning of resonant doublets in coupled optical cavities'. In: *Phys. Rev. D* 109 (2 2024), p. 022010.

[13] J. Casanueva D., J. Degallaix, A. C. Green, S. Hild, R. Maggiore, et al. 'The Need for Stable Recycling Cavities in Virgo-nEXT'. Tech. rep. VIR-0047A-23. https://tds.virgo-gw.eu/?content=3&r=21500. Jan. 2023.

[14] R. Maggiore, P. Ruggi, A. Freise, D. Brown, J. W. Perry, et al. 'Angular control noise in Advanced Virgo and implications for the Einstein Telescope'. Submitted to the journal. 2024.

[15] D. Bersanetti, M. Boldrini, J. Casanueva D., A. Freise, R. Maggiore, et al. 'Simulations for the Locking and Alignment Strategy of the DRMI Configuration of the Advanced Virgo Plus Detector'. In: *Galaxies* 10.6 (2022).

[16] C. Li, H. Wang, A. Dmitriev, R. Maggiore, H. Miao, et al. 'Broadening the dynamic range of the Pound–Drever–Hall frequency stabilization technique'. In: *Results in Physics* 30 (2021), p. 104835.

[17] E. N. Tapia San Martín, M. Valentini, D. Bersanetti, M. Was, R. Maggiore, et al. 'A MIMO approach for longitudinal sensing and control noise projections of Advanced Virgo gravitational wave detector'. In: *Classical and Quantum Gravity* 40.18 (2023), p. 185008.

[18] K. Somiya. 'Detector configuration of KAGRA–the Japanese cryogenic gravitational-wave detector'. In: *Classical and Quantum Gravity* 29.12 (2012), p. 124007.

[19] 'Cosmic Explorer: a next generation gravitational wave detector'. https://cosmicexplorer.org.

[20] J. M. Dobrindt, T. J. Kippenberg. 'Theoretical analysis of mechanical displacement measurement using a multiple cavity mode transducer'. In: *Physical Review Letters* 104.3 (2010), p. 033901.

[21] M. Aspelmeyer, T. J. Kippenberg, F. Marquardt. 'Cavity optomechanics'. In: *Reviews of Modern Physics* 86.4 (2014), p. 1391.

[22] X. Li, M. Goryachev, Y. Ma, M. E. Tobar, C. Zhao, et al. 'Broadband sensitivity improvement via coherent quantum feedback with PT symmetry'. arXiv:2012.00836 [quant-ph]. 2020.

[23] A. Dmitriev, H. Miao, D. Martynov. 'Enhancing the sensitivity of interferometers with stable phase-insensitive quantum filters'. In: *Physical Review D* 106.2 (2022), p. 022007.

[24] H. Jing, S. Özdemir, X.-Y. Lü, J. Zhang, L. Yang, et al. 'PT-symmetric phonon laser'. In: *Physical review letters* 113.5 (2014), p. 053604.

[25] Ş. K. Özdemir, S. Rotter, F. Nori, L Yang. 'Parity–time symmetry and exceptional points in photonics'. In: *Nature materials* 18.8 (2019), pp. 783–798.

[26] H. Grote, K. Danzmann, K. L. Dooley, R. Schnabel, J. Slutsky, et al. 'First Long-Term Application of Squeezed States of Light in a Gravitational-Wave Observatory'. In: *Phys. Rev. Lett.* 110 (18 2013), p. 181101.

[27] H. J. Kimble, Y. Levin, A. B. Matsko, K. S. Thorne, S. P. Vyatchanin. 'Conversion of conventional gravitational-wave interferometers into quantum nondemolition interferometers by modifying their input and/or output optics'. In: *Phys. Rev. D* 65 (2 2001), p. 022002.

[28] M. Evans. 'Lock Acquisition in Resonant Optical Interferometers'. https://labcit.ligo.caltech.edu/~mevans/lockAcq/thesis.pdf. PhD thesis. California Institute of Technology, 2002.

[29] A Staley, D Martynov, R Abbott, et al. 'Achieving resonance in the Advanced LIGO gravitational-wave interferometer'. In: *Classical and Quantum Gravity* 31.24 (2014), p. 245010.

[30] N. Ismail, C. C. Kores, D. Geskus, M. Pollnau. 'Fabry-Pérot resonator: spectral line shapes, generic and related Airy distributions, linewidths, finesses, and performance at low or frequency-dependent reflectivity'. In: *Optics Express* 24.15 (2016), pp. 16366–16389.

[31] R. W. P. Drever, J. L. Hall, F. V. Kowalski, J. Hough, G. M. Ford, et al. 'Laser phase and frequency stabilization using an optical resonator'. In: *Applied Physics B* 31.2 (1983), pp. 97–105.

[32] E. D. Black. 'An introduction to Pound–Drever–Hall laser frequency stabilization'. In: *American Journal of Physics* **69** 79 (2001).

[33] D. D. Brown, A. Freise. FINESSE. You can download the binaries and source code at http://www.gwoptics.org/finesse. May 2014.

[34] D. Brown, S. Rowlinson, S. Leavey, P. Jones, A. Freise. FINESSE 3. https://git.ligo.org/finesse/finesse3. 2020.

[35] D. Martynov, H. Miao, H. Yang, F. H. Vivanco, E. Thrane, et al. 'Exploring the sensitivity of gravitational wave detectors to neutron star physics'. In: *Phys. Rev. D* 99 (10 2019), p. 102004.

[36] R. V. Pound. 'Electronic Frequency Stabilization of Microwave Oscillators'. In: *Review of Scientific Instruments* 17.11 (Dec. 2004), pp. 490–505.

[37] G. Heinzel. 'Advanced optical techniques for laser-interferometric gravitational-wave detectors'. https://www.repo.uni-hannover.de/bitstream/handle/123456789/5674/265099560.pdf?sequence=1. PhD thesis. Max-Planck-institut für quantenoptik, 1999.

[38] A. C. Green. 'When light gets pushy: radiation pressure effects in interferometric gravitational wave detectors'. https://etheses.bham.ac.uk/id/eprint/8512/. PhD thesis. University of Birmingham, 2018.

[39] T. Corbitt, Y. Chen, E. Innerhofer, H. Müller-Ebhardt, D. Ottaway, et al. 'An All-Optical Trap for a Gram-Scale Mirror'. In: *Phys. Rev. Lett.* 98 (15 2007), p. 150802.

[40] M. Boldrini. 'Automatic Alignment in Advanced Virgo+ Phase I and Effects of Radiation Pressure'. PhD thesis. University of Rome - "Sapienza", 2023.

[41] R. W. Boyd. 'Intuitive explanation of the phase anomaly of focused light beams'. In: *J. Opt. Soc. Am.* 70.7 (1980), pp. 877–880.

[42] L. G. Gouy. 'Sur une propriété nouvelle des ondes lumineuses'. In: *C. R. Acad. Sci.* 110 (1890), p. 1251.

[43] L. G. Gouy. 'Sur la propagation anomale des ondes'. In: *C. R. Acad. Sci.* 111 (1890), p. 33.

[44] H. Kogelnik. 'On the Propagation of Gaussian Beams of Light Through Lenslike Media Including those with a Loss or Gain Variation'. In: *Appl. Opt.* 4.12 (1965), pp. 1562–1569.

[45] D. A. W. Töyrä. 'Consequences of being out of shape: the effects of beam distortions in advanced interferometric gravitational wave detectors'. https://etheses.bham.ac.uk/id/eprint/9258/. PhD thesis. University of Birmingham, 2019.

[46] D. Z. Anderson. 'Alignment of resonant optical cavities'. In: *Appl. Opt.* 23.17 (1984), pp. 2944–2949.

[47] A. Freise. 'The next generation of interferometry: Multi frequency modelling, control concepts and implementation'. https://www.repo.uni-hannover.de/handle/123456789/6218. PhD thesis. Hannover : Gottfried Wilhelm Leibniz Universität, 2003.

[48] I. Nardecchia. 'Control of optical aberrations in advanced interferometric gravitational wave detectors'. PhD thesis. University of Rome - "Sapienza", 2016.

[49] A. Rüdiger. 'Phase relationship at a symmetric beamsplitter'. Tech. rep. - unpublished. 1998.

[50] M. Ando, K. Arai, R. Takahashi, G. Heinzel, S. Kawamura, et al. 'Stable Operation of a 300-m Laser Interferometer with Sufficient Sensitivity to Detect Gravitational-Wave Events within Our Galaxy'. In: *Phys. Rev. Lett.* 86 (18 2001), pp. 3950–3954.

[51] A. Buonanno, Y. Chen. 'Laser-interferometer gravitational-wave optical-spring detectors'. In: *Classical and Quantum Gravity* 19.7 (2002), p. 1569.

[52] A. Buonanno, Y. Chen. 'Signal recycled laser-interferometer gravitational-wave detectors as optical springs'. In: *Phys. Rev. D* 65 (4 2002), p. 042001.

[53] B Caron, A Dominjon, C Drezen, R Flaminio, X Grave, et al. 'The Virgo interferometer'. In: *Classical and Quantum Gravity* 14.6 (1997), p. 1461.

[54] The Virgo collaboration. 'FINESSE-VIRGO, a package for modeling Advanced Virgo Plus'. You can download the source code at https://gitlab.com/ifosim/finesse/finesse-virgo. Commit: cc3fc21c. 2023.

[55] M. Valentini. 'The longitudinal control for the Advanced Virgo Plus gravitational wave detector'. PhD thesis. University of Trento, 2023.

[56] L Barsotti, M Evans, P Fritschel. 'Alignment sensing and control in advanced LIGO'. In: *Classical and Quantum Gravity* 27.8 (2010), p. 084026.

[57] A. Buikema, C. Cahillane, G. L. Mansell, C. D. Blair, R. Abbott, et al. 'Sensitivity and performance of the Advanced LIGO detectors in the third observing run'. In: *Phys. Rev. D* 102 (6 2020), p. 062003.

[58] D. V. Martynov, E. D. Hall, B. P. Abbott, R. Abbott, T. D. Abbott, et al. 'Sensitivity of the Advanced LIGO detectors at the beginning of gravitational wave astronomy'. In: *Phys. Rev. D* 93 (11 2016), p. 112004.

[59] M. Bader. ‘Seismic and Newtonian noise modeling for Advanced Virgo and Einstein Telescope’. PhD thesis. Vrije Universiteit Amsterdam, 2021.

[60] A. Siegman. ‘Lasers’. University Science Books, 1986.

[61] A. Bozzi, C. Bourgoin, S. Cortese, A. Errico, D. Enard, et al. ‘Last stage control and mechanical transfer function measurement of the VIRGO suspensions’. In: *Review of Scientific Instruments* 73.5 (2002), pp. 2143–2149.

[62] J. A. Sidles, D. Sigg. ‘Optical torques in suspended Fabry–Perot interferometers’. In: *Physics Letters A* 354.3 (2006), pp. 167–172.

[63] The Virgo collaboration. ‘The FINESSE model of Advanced Virgo Plus’. You can download the source code at https://gitlab.com/ifosim/finesse/finesse-virgo. Commit: 96200059. 2023.

[64] J. Casanueva Diaz. ‘Control of the Gravitational Wave Interferometric Detector Advanced Virgo’. PhD thesis. Cham: Springer International Publishing, Oct. 2017.

[65] E. Morrison, B. J. Meers, D. I. Robertson, H. Ward. ‘Automatic alignment of optical interferometers’. In: *Appl. Opt.* 33.22 (1994), pp. 5041–5049.

[66] A. Allocca, D. Bersanetti, J. Casanueva Diaz, C. De Rossi, M. Mantovani, et al. ‘Interferometer Sensing and Control for the Advanced Virgo Experiment in the O3 Scientific Run’. In: *Galaxies* 8.4 (2020).

[67] The Einstein Telescope collaboration. ‘The FINESSE model of Einstein Telescope-Low Frequency’. You can download the source code at https://gitlab.et-gw.eu/et/isb/interferometer/et-finesse-models. Commit: 5805646c. 2023.

[68] R. Maggiore, J. Casanueva, A. Freise. ‘Modelling CARMnull with Finesse to understand the behaviour of the sidebands throughout CARM offset reduction process’. Tech. rep. VIR-1298A-21. https://tds.virgo-gw.eu/?content=3&r=19778. Nov. 2021.

[69] R. Maggiore on behalf of the ISC team. ‘Longitudinal optical spring in AdV+’-Talk for the Joint IS / Comm. / DetChar-Tuesday-I Session at the March 2022 LVK meeting. Tech. rep. VIR-0282A-22. https://tds.virgo-gw.eu/?content=3&r=20270. Mar. 2022.

[70] R. Maggiore, B. Antonella, D. D. Brown, A. C. Green, J. Perry, et al. ‘Investigation of the tuning of the compensation plates focal length - follow-up’. Tech. rep. VIR-0641B-22. https://tds.virgo-gw.eu/?content=3&r=20732. June 2022.

[71] R. Maggiore, A. Freise. Virgo Logbook post: ‘Study of the double cavity pole frequency vs SR alignment’. Reference number: 55862 - https://logbook.virgo-gw.eu/virgo/?r=55862. 2022.

[72] R. Maggiore. ‘ DC optical gain of the DARM TF against SRM misalignment’. Tech. rep. VIR-0157A-24. https://tds.virgo-gw.eu/?content=3&r=23028. Feb. 2024.

[73] C. De Rossi, J. Brooks, J. Casanueva Diaz, A. Chiummo, E. Genin, et al. ‘Development of a Frequency Tunable Green Laser Source for Advanced Virgo+ Gravitational Waves Detector’. In: *Galaxies* 8.4 (2020).